Micro- and Macro-Scale Characterization of Fatigue Damage Behavior in Metallic Materials Under Constant and Variable Amplitude Multiaxial Loading

By

Abhay K. Singh

A Dissertation Presented in Partial Fulfillment
of the Requirements for the Degree
Doctor of Philosophy

Approved March 2021 by the
Graduate Supervisory Committee:

Aditi Chattopadhyay, Chair
Lenore Dai
Yongming Liu
Yang Jiao
Masoud Yekani Fard

ARIZONA STATE UNIVERSITY

May 2021

ABSTRACT

Engineering materials and structures undergo a wide variety of multiaxial fatigue loading conditions during their service life. Some of the most complex multiaxial loading scenarios include proportional/non-proportional loading, mix-mode loading, overload/underload, etc. Such loadings are often experienced in many critical applications including aircraft, rotorcraft, and wind turbines. Any accidental failure of these structures during their service life can lead to catastrophic damage to life, property, and environment. All fatigue failure begins with the nucleation of a small crack, followed by crack growth, and ultimately the occurrence of final failure; however, the mechanisms governing the crack nucleation and the crack propagation behavior depend on the nature of fatigue loading and microstructure of the material. In general, ductile materials witness multiple nucleation sites leading to its failure; however, high strength material fails from the nucleation of a single dominant crack. Crack propagation, on the other hand, is governed by various competing mechanisms, which can act either ahead of the crack tip or in the wake region of the crack. Depending upon the magnitude of load, overload/underload, mode-mixity, and microstructure, dominant governing mechanisms may include: crack tip blunting; crack deflection, branching and secondary cracking; strain hardening; residual compressive stresses; plasticity-induced closure, etc. Therefore, it is essential to investigate the mechanisms governing fatigue failure of structural components under such complex multiaxial loading conditions in order to provide reliable estimation of useful life. The research presented in this dissertation provides the foundation for a comprehensive understanding of fatigue damage in AA 7075 subjected to a range of loading conditions. A

series of fatigue tests were conducted on specially designed specimens under different forms of multiaxial loading, which was followed by fracture-surface analysis in order to identify the governing micromechanisms and corelate them with macroscopic fatigue damage behavior. An empirical model was also developed to predict the crack growth rate trend under mode II overloads in an otherwise constant amplitude biaxial loading. The model parameters were calculated using the shape and the size of the plastic zone ahead of the crack tip, and the degree of material hardening within the overload plastic zone. The data obtained from the model showed a good correlation with the experimental values for crack growth rate in the transient region.

To my parents and my sisters

for their continual support, inspiration, and patience

ACKNOWLEDGMENTS

I would like to express my deepest gratitude to my advisor, Regents' Professor Aditi Chattopadhyay for her valuable advice, encouragement and support at all stages of my research at Arizona State University. I am and will always be grateful for the guidance and the opportunities she has given me throughout my doctoral studies. I would also like to thank the members of my Supervisory Committee, Prof. Lenore Dai, Prof. Yongming Liu, Prof. Yang Jiao and Prof. Masoud Yekani Fard for volunteering their time to provide valuable insight and advice in regard to my research.

I would like to appreciate the guidance and mentorship I've received from the postdoctoral researchers Dr. Siddhant Datta and Dr. Kranthi Balusu. Dr. Datta helped me enhance my research skills and gave me the opportunity to learn under his guidance. I would also like to thank my friends and fellow graduate students for their support, feedback and friendship which created a pleasant work environment. The pursuit of this degree has been an exceptional experience; I thank my family and all my friends who have been a part of this experience.

I would like to thank the funding agencies for the research presented in this dissertation, which is supported in part by the US Naval Air Systems Command through Cooperative Agreement P-8A Aircraft Support for PMA-290, Program Manager Nam Phan; Army Research Laboratory through Cooperative Agreement W911NF-17-2-0207, Technical Program Manager Dr. Asha Hall.

TABLE OF CONTENTS

Page

CHAPTER Page

CHAPTER Page

CHAPTER Page

LIST OF TABLES

Table Page

LIST OF FIGURES

Figure Page

Figure Page

Figure Page

Figure Page

Figure Page

Figure Page

Figure Page

Figure Page

Figure Page

1. INTRODUCTION

1.1. Historical Background

Failure in engineering structures can arise following long-term exposure to various forms of fatigue load including low and/or high amplitude random loads. Such failures generally occur at considerably smaller values of peak load (cyclic loading) than the estimated "safe" loads obtained from static fracture analyses due to the plastic deformation in a localized area [1]. Wohler [2] was perhaps the first researcher to conduct systematic investigations into fatigue failure. He established an experimental framework to investigate progressive failure on railway axles and observed that the strength of steel during cyclic loading was significantly smaller than its static strength. This pioneering work introduced the term "endurance limit" and led to the characterization of fatigue behavior in terms of stress amplitude versus fatigue cycle (S-N) curves. In this context, the work of Bauschinger [3] was more important in popularizing the theory that the elastic limits of metals in cyclic loading can be different from those in monotonic loading. This behavior was attributed to the occurrence of cyclic softening and cyclic strain hardening. Fatigue cracks in metallic materials usually develop due to cyclic plastic deformation in a localized area, which is caused by the presence of a small crack or pre-existing defect on the surface or in the sub-surface region. Working independently, Coffin [4] and Manson [5] hypothesized that plastic strains are responsible for cyclic damage. They further proposed an empirical relationship between the number of load reversals to fatigue failure and the plastic strain amplitude. This approach is still widely used to characterize strain-based fatigue behavior. The initial work in establishing mathematical tool for quantitative analysis came from

Inglis' stress analyses [6] and Griffiths' energy concepts [7]. Inglis [6] developed a linear elastic solution to determine stress around an elliptical hole in a plate. This solution is applicable to the extreme limits of the form that an ellipse can assume, including a circular hole and a very fine crack. On the other hand, Griffith [7] invoked the first law of thermodynamics to formulate a criteria for the unstable extension of a crack in a brittle solid using a simple energy balance. According to this theory, when the strain-energy change resulting from an increment of crack is sufficient to overcome the surface energy of the material, crack becomes unstable, and thus fracture occurs. Although the work of Inglis [6] and Griffiths [7] was important, the scope of their work was limited and could not fully characterize fatigue failure. In this direction, a major contribution came from Irwin [8], who expressed the amplitude of stress singularity ahead of a crack in terms of the stress intensity factor. Subsequent attempts were made to characterize fatigue crack growth with the help of the stress intensity factor and using linear elastic fracture mechanics (LEFM). LEFM solutions can be applied to a component when the plastic deformation ahead of the advancing fatigue crack is a minor perturbation in an otherwise elastic field. For the cyclic variation of the stress field, Paris *et al*. [9] suggested that the LEFM characterization of the crack growth rate, *da/dN*, should be a function of stress intensity factor range during constant amplitude fatigue loading. Later, they showed that the crack growth rate is related to stress intensity factor range by the power law relationship. This characterization was validated by using experimental data from a wide range of metallic materials with different combinations of stress range and crack length for different specimen geometries. On the other hand, Elber [10] demonstrated that the fatigue cracks

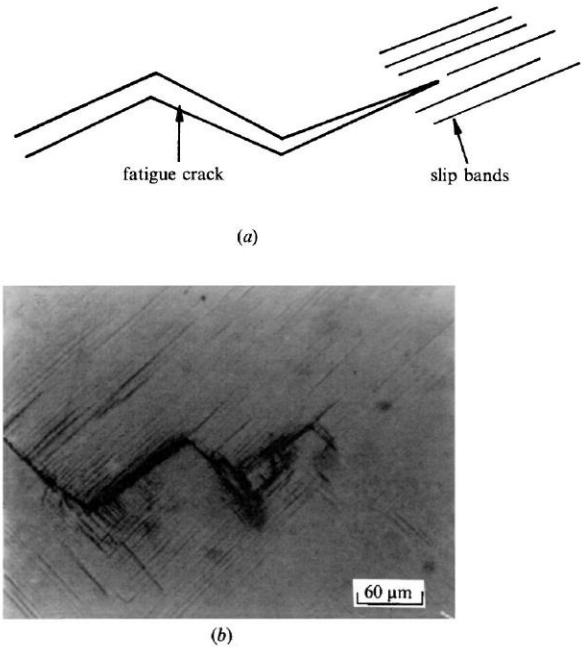

Figure 1.1: (a) A schematic of stage I fatigue crack growth, (b) An example of stage I fatigue crack growth in a single crystal of Mar M-200 nickel-base superalloy. The tensile axis is vertical. The {100} plane is normal to the tensile axis.[1].

could still remain closed when the applied cyclic load is tensile. This implies that the nominal value of the stress intensity factor range used to determine the crack growth rate may not be accurate. Furthermore, he suggested using the effective value of the stress intensity factor range instead of nominal values; this can be calculated after compensating for premature closure of the contact surfaces in the wake region of the crack tip. Significant research has been conducted to understand the mechanisms governing crack initiation and propagation behavior during fatigue loading. These investigations led to important developments in identifying key microscopic features of fatigue deformation. Thompson *et al*. [11] observed that the slip bands, along which deformation was concentrated, persistently re-appeared at the same locations during cycling loading and termed these surface markings “persistent slip bands”. Zapffe *et al.* [12] described ripple markings on

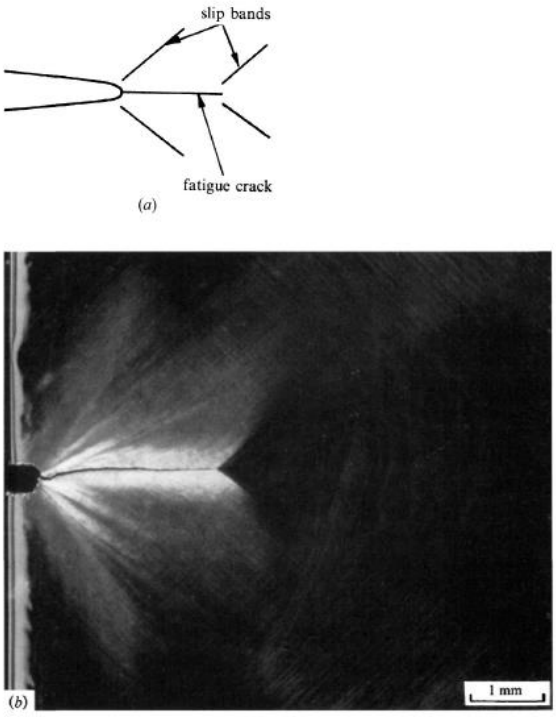

Figure 1.2: (a) An idealization of stage II fatigue crack growth, (b) An example of stage II crack growth in a Cu single crystal. Two sets of {111} slip planes (white areas) are seen. The tensile axis is vertical [1].

the fracture surfaces of specimens that failed under fatigue loading; these are now known as fatigue striations. Forsyth *et al*. [13] separated different stages of fatigue growth on the basis of mechanisms associated with the crack growth process and termed them stage I and stage II growth. As shown in Figure 1.1, when the crack and the plastic deformation near the crack tip are confined within a few grain diameters, crack growth occurs predominantly by single shear in the direction of the primary slip system. This single slip mechanism leading to a zig-zag crack path has been termed stage I crack growth. On the other hand, when the plastic zone at the crack tip encompasses many grains, crack growth process involves two slip systems. This duplex slip mechanism is termed as stage II, which results in a planar (mode I) crack path normal to the far-field tensile loading as shown in Figure

1.2. Furthermore, they correlated the stage II fatigue crack growth rate with spacing between adjacent striations, and their work played an important role in the development of various fatigue crack growth theories.

1.2. Design Approach

Fatigue failure in engineering components can progress in several stages; for example, defect nucleation in an initially undamaged region is followed by crack propagation in a stable state prior to final catastrophic failure. The different failure stages were broadly classified as follows [1]:

1. Nucleation of permanent damage due to microstructural changes
2. Microscopic crack development
3. Coalescence of microscopic cracks into a dominant macro-crack that may result in the catastrophic failure
4. Dominant macro-crack propagation in stable stage
5. Unstable propagation of the dominant crack leading to fast fracture.

Numerous factors affect fatigue crack nucleation and propagation, including mechanical, microstructural, and environmental variables. These further influences the use of various design philosophies adopted to quantify the crack initiation and propagation behaviors underlying fatigue failure. Among them, the most widely used design philosophies are the "total-life" and "defect-tolerant" approaches.

Total-life approach:

In classical fatigue design approaches, the total fatigue life is expressed in terms of the cyclic stress range (S-N curve) or strain range (plastic or total). These methods estimate

the number of fatigue cycles necessary to induce fatigue failure in an initially uncracked specimen subjected to controlled loading conditions. With this approach, the total fatigue life is obtained by incorporating the number of fatigue cycles taken to initiate a dominant crack and propagate it until catastrophic failure. Wohler [2] was the first to introduce this stress-life approach, from which the concept of "endurance limit" evolved. It has a widespread use in fatigue analysis where components are designed either as a high-cycle fatigue (HCF) application or a low-cycle fatigue (LCF) application. In case of HCF, component is designed for the low-amplitude cyclic stresses that induces primarily elastic deformation and provides a longer life; whereas, component under LCF are exposed to high-amplitude cyclic stresses where considerable plastic deformation occurs during cyclic loading that results in a shorter life. The importance of plastic strain in inducing permanent fatigue damage is realized by Coffin [4] and Manson [5] who independently proposed a plastic-strain based continuum characterization of LCF. The Palmgren-Miner cumulative damage rule [14,15] provide a simple criterion for predicting the extent of fatigue damage induced by a particular block of constant amplitude cyclic stresses in a loading sequence consisting of various blocks of different stress amplitudes. The classical approaches also offer various techniques to include the effects of mean stress, stress concentrations, environments, multiaxial stresses, and variable amplitude stress fluctuations to predict total fatigue life [1].

Defect-tolerant approach:

The fracture mechanics approach to fatigue design invokes a "defect-tolerant" philosophy based on the premise that all the engineering components are inherently flawed.

Under this approach, a component's useful fatigue life is defined as the number of fatigue cycles required to propagate the dominant crack from its initial size to the critical size. The critical size of the crack is based on various parameters including fracture toughness, allowable load, permissible change in the compliance, and others [1]. The defect-tolerant approach uses empirical relations based on fracture mechanics to predict the crack propagation life. However, to apply LEFM under the defect-tolerant approach, the component should be subjected only to a small scale yielding in a predominantly elastic loading condition. Paris *et al.* [9] were the first to suggest that the increment of fatigue crack advance per cycle, *da/dN*, could be related to the range of the stress intensity factor, ΔK, during constant amplitude cyclic loading. Similar approach was used by Tanaka [16] to express fatigue crack growth rate as a function of effective stress intensity factor. This model assumed that a fatigue crack grows when the sum of the absolute values of the displacements in a plastic strip reaches a critical value. Irwin [17] estimated the boundary of the plastic zone ahead of a crack in a ductile solid using von Mises equivalent stress criteria. It was found that the extent of the plastic zone ahead of the crack tip is proportional to the square of the stress intensity factor. Dugdale [18] estimated the size of the yield zone ahead of a mode I crack in a thin plate of an elastic-perfectly plastic solid. The results from Dugdale's model compared well with the Irwin approximation. This approach also provides various techniques to include the effects of mean stresses, stress concentrations, environments, variable amplitude loading spectra, and multiaxial stresses to estimate useful crack growth life [1,19].

1.3. Research Motivation

Engineering structures and materials during their service life are often exposed to a variety of multiaxial stress states due to the orientation of the underlying defects, residual stresses, and external loading conditions. Moreover, the presence of geometrical notches in key components result in localized regions of elevated stress that can significantly alter the local stress state within the components. Even for the simplest case of uniaxial loading, the local stress at the crack tip approaches infinity and is expressed in three different modes of deformation as shown in Figure 1.3. In the opening mode, the principal load is applied normal to the crack plane and is called mode I. In mode II, in-plane shear load is applied to the crack surface and is called in-plane sliding mode. In case of mode III, out-of-plane shear load is applied to the crack surface. Each mode of deformation produces stress singularity at the crack tip and can be present alone, or in a combination of two or three modes giving rise to the mix-mode condition. Traditional applications of fracture

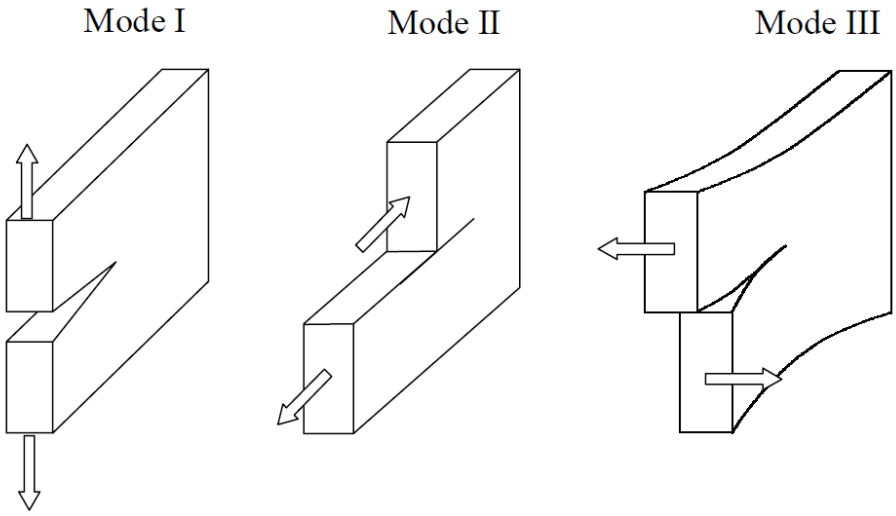

Figure 1.3: Different modes of crack tip deformation.

mechanics have been focused on cracks growing under pure mode I condition [20–24]. However, many service failures occur when components are subjected to mix-mode multiaxial fatigue loadings. A typical example of such an external multiaxial loading in engineering applications is a crack initiated in a transverse plane from a tubing shaft surface under combined bending and torsional loads [19]. Components of rotorcraft and fixed-wing aircraft also experience bending-torsion coupled fatigue with varying values of stress amplitudes ratios. Similarly, pressure vessels, tubes, and pipes are subjected to biaxial stresses due to internal pressure. Automobile transmission shafts undergo combined shear stresses arising from torque and axial stresses generated by bending [1]. Since a fatigue crack in a mix-mode condition propagates in a non-self similar manner, it is difficult to predict the crack path or quantify crack growth throughout various stages in its propagation. Under such conditions, estimation of fatigue life and/or monitoring crack growth is a challenging and cumbersome task. Therefore, it is essential to understand the fatigue crack initiation and propagation under these realistic multiaxial service loads to identify the governing micromechanisms and accurately predict fatigue life.

Crack initiation and propagation under multiaxial fatigue loading is a highly complex phenomenon, because of which most of the multiaxial fatigue investigations have employed constant amplitude load conditions. However, multiaxial loading scenario can be found in the component in various different forms including in-phase loading, out-of-phase loading, load excursion, etc., as shown in Figure 1.4. Several efforts have been made by researchers [25–28] to investigate the effects of in-phase and out-of-phase loading on crack initiation and propagation behavior, for which they have used a cruciform type of

specimen with a central notch under an in-plane biaxial stress state (gauge region), as shown in Figure 1.5. However, load excursion / overload in multiaxial fatigue is a different scenario that has been rarely explored. A few examples of such load conditions include over-/underload experienced by aircraft wings during take-off and landing; overload experienced by the rotor and bearings of the turbo-generator at start-up, etc. [29]. The presence of load fluctuations induces load-interaction effects that can be detrimental to

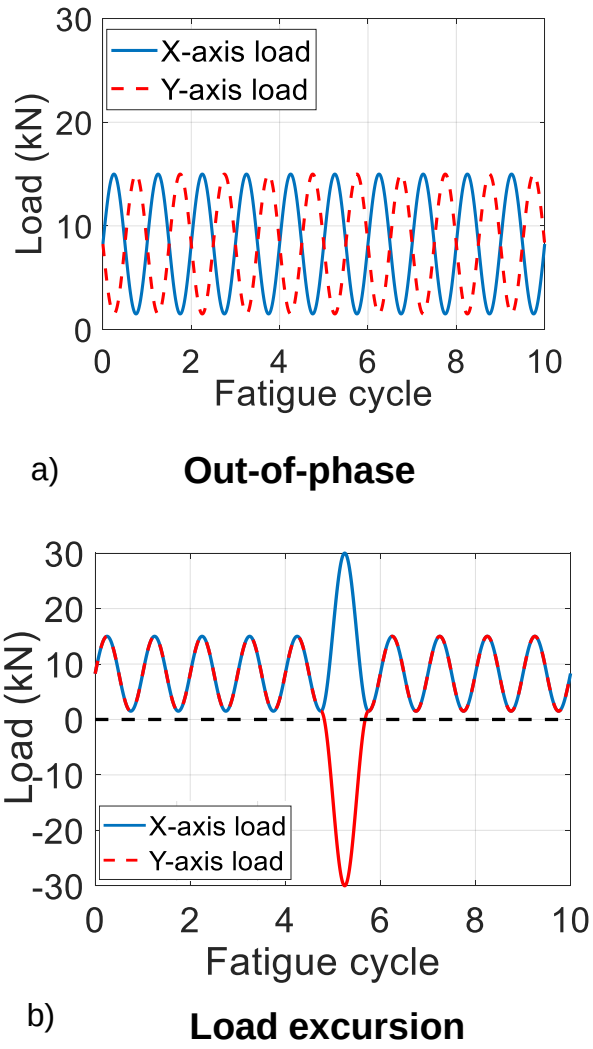

Figure 1.4: Different forms of multiaxial load: a) out-of-phase; b) load excursion.

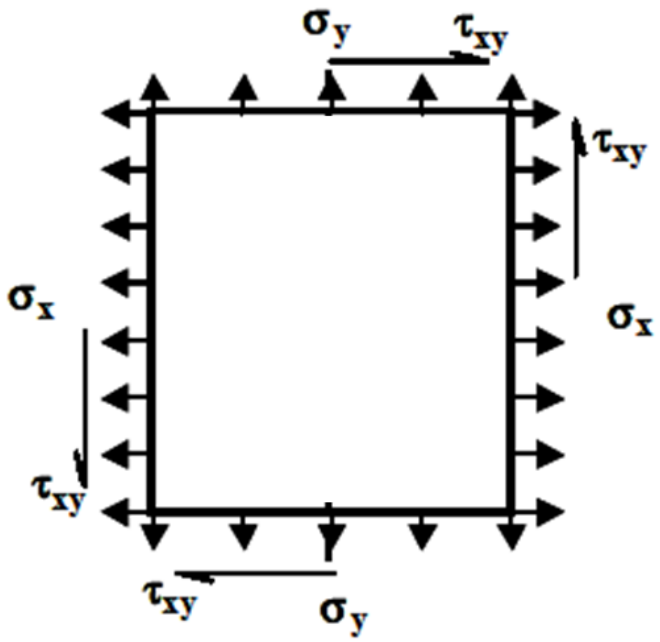

Figure 1.5: An inclined crack subjected to a biaxial stress state.

fatigue life and contribute to catastrophic failure. Therefore, as part of this thesis, systematic and comprehensive experimental investigations have been performed to characterize the micro- and macro-scale fatigue behavior under constant and variable amplitude multiaxial loading. In addition, the fatigue-fracture micromechanisms that govern crack nucleation and various stages of crack propagation in the presence/absence of an overload have been identified through quantitative fractography and correlated with macroscopic crack growth.

1.4. Objectives of the Work

The overreaching goal of the present work is to obtain a comprehensive understanding of fatigue damage evolution in an aerospace grade AA alloy under multiaxial loading conditions. This requires a detailed investigation on fatigue crack initiation and propagation behavior under a constant as well as a variable amplitude multiaxial loading.

Both the micro- and the macro-scale analyses are needed to identify the underlying micromechanism and corelate them with the macroscale fatigue damage behavior. The following are the principal objectives of this work:

- Assess fatigue crack initiation and propagation behavior in AA 7075 alloy subjected to uniaxial bending/torsional loading, and multiaxial mix-mode bending-torsion loadings. Gain comprehensive insight into fatigue damage initiation, crack orientation and trajectory, crack deflection, and crack propagation modes at various magnitudes of applied load and stress amplitude ratio. Identify micromechanisms governing crack nucleation and propagation behavior under complex multiaxial fatigue loadings at different stages of crack growth.
- Study the effects of shear (mode II) overloads under otherwise constant amplitude biaxial fatigue loading (mode I). Characterize the in-plane biaxial fatigue crack propagation behavior of AA 7075 in the transient region and investigate the underlying microscale mechanisms at different magnitudes of shear overload and at various fatigue crack lengths.
- Investigate fatigue crack growth behavior in AA 7075 subjected to load excursions of various mode mixity in otherwise constant amplitude in-plane biaxial fatigue loading (mode I). Identify micromechanisms governing crack growth when the overload is applied at different crack lengths. Analyze fracture surface morphology and correlate micro- and macroscale fracture features.
- Develop an empirical model to predict the crack growth rate in the transient region created by the load excursion in an otherwise constant amplitude biaxial fatigue loading.

Model should be capable of depicting the effects of overload ratio on the initial acceleration, delayed retardation, and gradual recovery while predicting the crack growth rate.

1.5. Outline

The dissertation is structured as follows:

Chapter 2 presents a detailed investigation conducted on fatigue crack initiation and propagation behavior in AA 7075 under multiaxial bending-torsion load conditions. A thin-walled tubular specimen was designed to achieve a combination of mode I and II loadings to study mix-mode bending-torsion fatigue behavior. Analyses of crack trajectory and crack growth modes were conducted for various amplitudes of bending and shear stresses at a constant stress amplitude ratio (λ). Tests were also conducted under pure bending and pure torsion loading to gain better insight into the mechanisms governing fatigue-fracture behavior under combined bending-torsion loading and segregate the effects of multiaxiality from uniaxial bending or torsion loading. This chapter also contains a detailed investigation on microscale fracture features that help identify the micromechanisms governing crack initiation and propagation behavior under combined bending-torsion loading at different stress levels and at various crack propagation stages. Finally, the results from non-proportional bending-torsion coupled loading are presented and compared with the findings obtained under proportional/in-phase bending-torsion load conditions.

Tensile biaxial fatigue loading and the effects of shear overloads in an otherwise constant amplitude are examined in chapter 3. The experiments were conducted on a cruciform specimen of AA 7075-T651 with a central circular hole with an inclined notch

at a 45° angle. Analyses of fatigue damage behavior in the transient region, generated by the application of overloads, were conducted at micro- and macro-scales for various combinations of overload ratios and crack lengths. The macroscale characterization results show the effect of shear overloads on fatigue life and recovery distance, the degree of initial acceleration, and the delayed retardation in the crack growth rate. On the other hand, microscale characterization reveals that the fracture features of the transient zone are important for identifying governing micromechanisms.

Chapter 4 describes an investigation conducted to understand the effects of overload mode-mixity on crack growth behavior and governing micromechanisms of AA 7075 T6. Cruciform AA 7075 T6 specimens were subjected to constant amplitude planar biaxial fatigue load with single overloads, and key fatigue damage behaviors including fatigue life, crack growth rate, and recovery distance were quantified and correlated to overload parameters. Additionally, scanning electron microscope (SEM) fractography was conducted to identify and relate fracture surface features to governing fatigue damage micromechanisms. The microscale analysis showed distinct fracture features in the pre-overload, transient, and post-overload regions for both tensile and shear dominant overloads.

In chapter 5, an empirical model is developed to predict the crack propagation behavior in the transient region created by the load excursion in an otherwise constant amplitude biaxial fatigue loading. The developed model is further validated to depict the effects of overload ratio on the initial acceleration, delayed retardation, and gradual recovery while predicting the crack growth rate.

Chapter 6 summarizes the research work presented in this dissertation and outlines the important contributions. It also suggests potential research directions and discusses future investigations to extend this work to meaningful applications.

2. CONSTANT AMPLITUDE BENDING-TORSION FATIGUE

2.1. Introduction

Fatigue load can manifest itself on a structure in a variety of ways which can lead to different kinds of loading scenario as experienced by different components. For example, the components of an aircraft, as shown in Figure 2.1, experiences different combinations of uniaxial as well as multiaxial load conditions during their normal service operation. Some of these include bending-torsion coupled load acting on the aircraft's tail; biaxial fatigue load experienced by the fuselage; overloads/underload applied during take-off and landing, etc. In all these cases, components can be subjected to proportional as well as non-proportional loading conditions which further complicates the loading scenario. Therefore, it is important to investigate the fatigue damage behavior of the components under various forms of multiaxial fatigue loading in order to better predict their useful life.

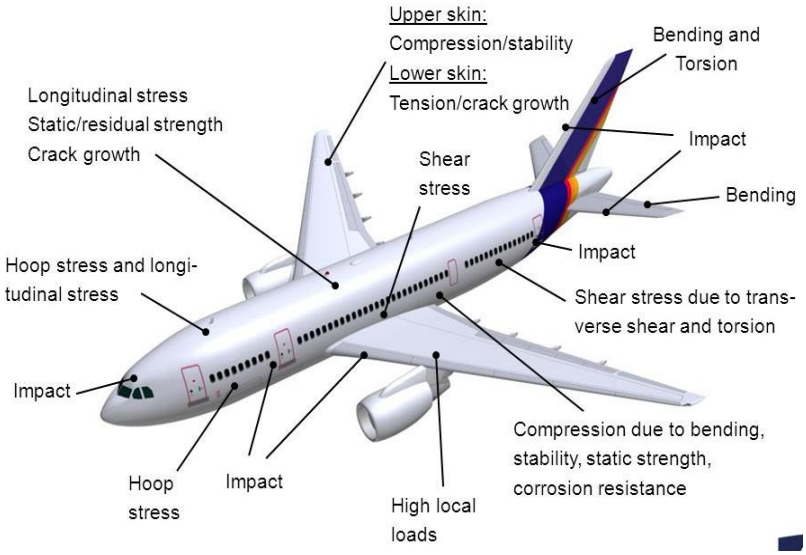

Figure 2.1: Components of aircraft under different load combinations.

As previously stated, nucleation and propagation of fatigue damage in structural components is a complex phenomenon and depends on a number factors such as material type and microstructural characteristics, and type of loading or stress state [1,19]. A vast majority of investigations have been limited to simple stress states conducted under uniaxial tension-compression conditions with the goal of determining the relationship between the number of cycles to failure and the magnitude of the applied load [30–32]. However, operational service conditions often involve more complex loading scenario, where various combinations of important fatigue variables, such as load magnitudes, mean stress, load non-proportionality, ratio among different modes of loads, specimen geometry, etc. may exist [33–37]. These variables can greatly influence the micromechanisms governing the crack initiation and the modes of crack propagation, which can subsequently affect the fatigue life of the component. Hua *et al*. [38] investigated fatigue crack growth under pure tension, combined tension and torsion, and pure torsion between high-cycle and low-cycle fatigue. It was found that under tension and combined tension-torsion, cracks propagated in mode I; whereas under pure torsion, a dominant single crack initiated that propagated in mode II until final failure in the high cycle fatigue regime. Tanaka *et al.* [16] studied crack growth behavior on a plate type specimen with an inclined central crack and observed that the fatigue crack growth rate under mix-mode loads were significantly higher than those under mode I load at the same magnitude. Socie [39] found that the load magnitude can significantly affect the mode of crack propagation and indicated that a shear mode growth (mode II) would occur at high strain ranges, while tensile growth (mode I) would occur at low loads in torsional fatigue tests. Similar observations were reported by

Brown and Miller [40] while investigating tubular specimens under combined tensile and torsional loading. It was found that when the shear strain to tensile strain ratio was less than 1.5, fatigue cracks that were initiated in mode II would turn to mode I propagation. However, when this ratio was larger than 1.5, cracks would continue to grow in mode II. Plank *et al.* [41] studied crack propagation behavior on compact tension specimen under proportional as well as non-proportional mix-mode loading. They found that under non-proportional mix-mode loading (mode I and mode II), two kinds of stable crack propagation occurred. When the effective mode II range exceeded the threshold stress intensity factor (mode II), shear mode growth occurred else the crack deflected and propagated in mode I loading. These observations clearly indicate that the crack initiation and propagation behavior can be easily influenced by changing any of the above-mentioned fatigue variables.

In the limited studies conducted on multiaxial loading, primary attention has been given to investigate axial-torsion coupling, in which either both the loadings were cyclic or one of them was cyclic while other was static [42,43]. Very few investigations have been reported on the fatigue behavior of metallic materials subjected to combined bending and torsion loadings [44–52]. Perhaps, Gough *et al.* [44] were the first to study the combined effect of bending and torsion load using a solid cylindrical bar of steel. Loads were applied with the help of intricate fixture design, in which a single loading arm was used to transmit the combined load to the specimen by adjusting the angle of orientation between the arm and the specimen. Thus, the mismatch in orientation was utilized to split the applied load into two components, i.e. bending moment and twisting moment. A similar test set-up was

used in the subsequent experiments by different authors in their research work [50–52]. Findley *et al.* [50] studied the behavior of 76S-T61 aluminum alloy for four different combinations; Marciniak *et al.* [51] used two different grades of steels (18G2A and 10HNAP); Niesłony *et al.* [52] investigated the behavior of AA 6068 and AA 2017A. All these studies [49–52] were conducted on solid cylindrical specimens using stress-life approach in order to determine fatigue life or endurance limit but none of the reported results provide any information either on the damage initiation mechanisms or on the crack propagation behavior of the materials under investigation, which are the two crucial aspects in the analysis of fatigue crack under mixed mode loading.

There is very limited experimental data available on combined bending-torsion fatigue that describes damage initiation or crack propagation behavior in the material [45–48]. Susmel *et al*. [45] studied the fatigue behavior of solid cylindrical Al 6082-T6 under fully reversed bending-torsion condition and found that when bending dominates in the loading ($\lambda < 1$), the crack initiation occurs in mode II at a point of maximum bending load, but the crack primarily propagates under mode I stresses. On the other hand, when the applied torque is dominant ($\lambda > 1$), multiple cracks nucleate on the gauge surface and are oriented along the extrusion direction. These observations remained consistent irrespective of the phase difference in the loading. Park *et al.* [46] investigated the behavior of small crack in A533B steel for in-phase and 90° out-of-phase loading and found that the crack growth rate varied linearly with the crack size. For all the cases, cracks initiated on the plane of maximum shear strain, but propagated differently for in-phase and 90° out-of-phase loading. While the crack continued to grow on the plane of initiation for 90° out-of-phase

loading, it transitioned from the plane of maximum shear strain to the plane of maximum normal strain for in-phase loading as the strain level or the ratio of shear-to-bending strain was reduced. Some researchers have also used a notched specimen in their study [47,48]. Park *et al.* [47] used solid round bars of steel with a circumferential semicircular groove and found that the cracks nucleated on the planes of maximum amplitude of shear stress, but propagated on the planes of maximum principal stress amplitude. An exception to this trend was observed for 90° out-of-phase tests when $\lambda < 0.5$, for which crack propagated on the planes oriented between the planes of maximum shear stress amplitude and the planes of maximum principal stress amplitude. Branco *et al.* [48] studied fatigue behavior of lateral notched round bars made of high strength steel and found that multiple cracks were nucleated on the fracture surfaces. With an increase in either normal stress amplitude or λ, early initiation of the crack was observed along with an increased rate of crack propagation. In the aforementioned studies, little attention was given to study the nature of crack initiation and propagation behavior under combined bending-torsion loading, and there is a significant lack of understanding into the underlying fatigue-fracture micromechanisms. In addition, all the investigations on bending-torsion loading till this date have been performed on specially designed complex test setup, which precluded the attainment of consistency in the test procedure, and complicated the load applying mechanism, making it less reliable. Since it is evident that the fatigue damage nucleation and crack propagation behavior depend on a multitude of factors such as material properties, stress amplitude ratio (λ), applied load, phase difference, presence of a notch, etc., it becomes imperative to investigate crack behavior under combined bending-torsional loading. To the authors'

knowledge, there is no reported literature on the behavior of AA-7075, a high-strength aluminum alloy often employed in aerospace components, under complex multiaxial bending-torsion loading.

This chapter presents an experimental investigation of fatigue damage behavior in tubular specimens of AA 7075 subjected to multiaxial bending-torsion loading with the help of a simple test setup. The primary goal is to obtain a comprehensive insight into fatigue damage initiation, crack orientation and trajectory, crack deflection, and crack propagation modes at various magnitudes of applied load, and stress amplitude ratio. A detailed characterization of the fracture surfaces is conducted to relate the macroscale observations with microstructural characteristics. The goal is to capture distinct fracture features and active micromechanisms operating along the direction of crack propagation at various stages in its propagation. The effect of load magnitude and/or stress amplitude ratio on micromechanism governing crack nucleation and propagation are also identified and characterized. Finally, the result of the tests conducted under non-proportional bending-torsion coupled loading is also presented to compare and contrast its behavior with proportional/in-phase bending-torsion load condition.

2.2. Material and Methods

2.2.1. Material

The material used in this bending-torsion fatigue study was procured in the form of cylindrical bars of aluminum alloy 7075-T6, which is often used in aircraft structural components, automotive industry, and other high-strength applications [53]. Material properties provided by the manufacturer include a yield strength of 503 MPa, the ultimate

tensile strength of 572 MPa, and modulus of elasticity of 71.7 GPa. It has a Brinell hardness value of 150 and the chemical compositions are in accordance with ASTM standard B211.

2.2.2. Specimen and Fixture Design

Specimen design plays an important role in investigating the fatigue crack initiation and propagation behavior, and there is no standardization of specimen geometries for testing mix-mode loading conditions. Richard [54] has presented nine different specimens, which are often used in mix-mode fracture and fatigue studies. These include plate specimen with inclined central crack under tension, plate specimen with inclined edge crack under tension,

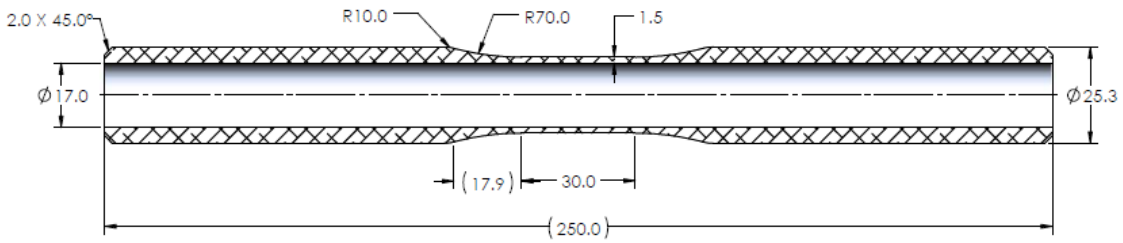

Figure 2.2: Design of tubular specimen used in bending-torsion fatigue. All dimensions are in mm.

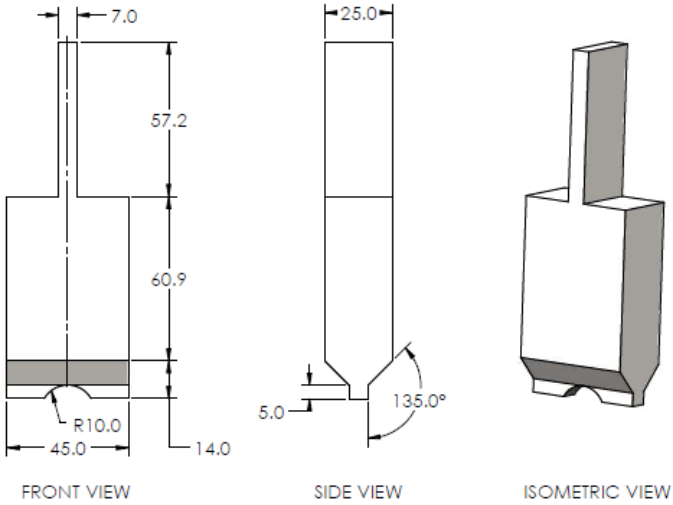

Figure 2.3: Design of fixture used in bending-torsion fatigue. All dimensions are in mm.

disc specimen with inclined central crack, cruciform specimen with inclined central crack, shear specimen with inclined central crack, tubular specimen with inclined crack under torsion, tubular specimen with transverse crack under combined tensile and torsional stresses, three or four-point bending and shear specimen with an offset edge crack, and compact tension and shear specimen. In the case of experiments involving torsion, either a solid cylindrical specimen or a tubular specimen is used. It is an established fact that a thin-walled tubular specimen is an efficient way to produce mode II crack growth under completely reversed torsional load [38,43,55,56]. On the other hand, circumferentially notched cylindrical specimens are found to be more useful in studying fatigue crack growth behavior during mode III loading [19,57]. For a mix-mode load condition, involving bending and torsion, it is advantageous to use a tubular specimen since a crack initiated in a transverse plane from a tubing shaft surface under bending and torsion is under a state of combined mode I, II and III loadings [19]. An added advantage of a tubular specimen over a solid cylindrical specimen is that the solid cylindrical specimen is subjected to a stress gradient along the specimen thickness and an ideal biaxial stress state is not obtained; therefore, a tubular specimen is adopted for investigating mix-mode bending-torsion fatigue behavior and analysis is conducted to validate the state of stress.

In this experiment, a tubular specimen is used, which was machined from solid bars of aluminum alloy (AA 7075-T6). The specimen, as shown in Figure 2.2, was designed in compliance with ASTM standard E2207-15 while the length of the gripping area was increased to 250 mm to accommodate the specimen into the test frame. The selected standard provides design recommendations for a thin-walled tubular specimen under axial-

torsional load coupling and it also fulfills the design requirements for the specimen under combined bending-torsion loading. As shown in Figure 2.2, the specimen has a gauge length of 30 mm in the central part, where outer and inner diameters are 20 mm and 17 mm respectively, making it possible to have a relatively thin wall (1.5 mm thickness).

A suitably designed fixture was necessary for the vertical actuators to apply the bending load on the designed specimen. As shown in Figure 2.3, the fixture was designed to accommodate the curved shape of the specimen, while distributing the bending load over a length of 7 mm along the longitudinal axis of the specimen. A CAD package (SOLIDWORKS) was utilized during the entire process to complete the fixture design.

2.2.3. Experimental Procedure

Experiments were conducted using the MTS planar biaxial/torsion load frame with a dynamic load capacity of 100 kN in both horizontal and vertical directions and a torsional capacity of 1100 Nm. The load frame is equipped with six independent controllers that allow the users to conduct tests under a wide range of load conditions, including in-phase, out-of-phase, proportional and non-proportional loading. As shown in Figure 2.4, the two horizontal actuators were used to apply torsional load while the bending load was applied with the help of a specially designed fixture mounted on one of the vertical actuators. Fatigue tests were conducted for both uniaxial (pure bending / pure torsion) and multiaxial (combined bending and torsion) load conditions, which are summarized in Table 2.1. All the multiaxial in-phase bending-torsion fatigue tests were carried out at a constant value of stress amplitude ratio ($\lambda = 0.6$) at room temperature. The value of λ was selected such that the fracture phenomenon comprised the effects of both torsion and bending loads at

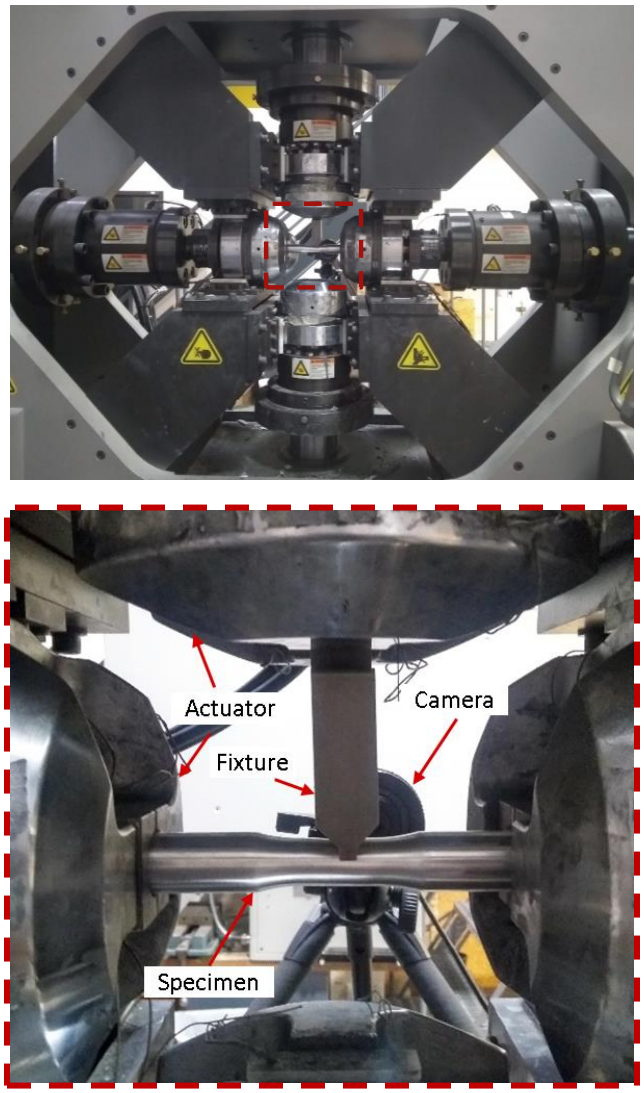

Figure 2.4: Experimental set-up used in bending-torsion fatigue tests.

different sets of load conditions (Load 1 - Load 3) used in the experiments. For each set of loads, 3-5 specimens were tested using constant amplitude sinusoidal loads at a frequency of 1 Hz and a load ratio (R) of 0.1, the details of which are presented in Table 2.1. The maximum values of bending load (P_{max}) and torsional load (T_{max}) varied for different experiments, which was reflected in the values of maximum tensile stress due to bending load (σ_b), and shear stress (τ_T) due to torsional load. Table 2.1 also contains the details of

Table 2.1:

Loading conditions for bending-torsion tests.

Load Case	Test ID	R-Ratio	P_{max} (N)	T_{max} (N.m)	Frequency (Hz)	τ_T (MPa)	σ_b (MPa)	λ (τ_T / σ_b)
Load 1	B3S4	0.1	8250	150	1	200	338	0.60
	B3S5	0.1	8250	150	1	200	338	0.60
	B3S6	0.1	8250	150	1	200	338	0.60
Load 2	B2S2	0.1	6350	120	1	145	260	0.60
	B2S3	0.1	6350	120	1	145	260	0.60
	B3S11	0.1	6350	120	1	145	260	0.60
	B3S12	0.1	6350	120	1	145	260	0.60
	B3S13	0.1	6350	120	1	145	260	0.60
Load 3	B3S8	0.1	5420	100	1	133	222	0.60
	B3S9	0.1	5420	100	1	133	222	0.60
	B3S10	0.1	5420	100	1	133	222	0.60
Load 4	B2S8	0.1	11000	0	1	0	451	0
	B2S9	0.1	11000	0	1	0	451	0
	B2S10	0.1	11000	0	1	0	451	0
Load 5	B3S1	0.1	0	120	1	145	0	∞
	B3S2	0.1	0	165	1	220	0	∞
	B3S3	0.1	0	200	1	266	0	∞

the tests conducted under pure bending (Load 4) and pure torsion (Load 5) load conditions. These tests were conducted to evaluate their individual contributions on crack propagation behavior and on fatigue life to better understand the effect of multiaxiality under combined bending and torsional loading. A high-resolution camera was positioned on the rear side of the specimen to capture the crack initiation and growth. The camera was programmed using LabVIEW to capture images at user-defined time intervals. The fatigue tests were interrupted once the surface crack length reached approximately 10-15 mm or if the crack has traveled completely through the thickness of the specimen for a length of 3-6 mm. For the microscale analysis of crack initiation and propagation behavior in AA 7075-T6, fracture surfaces were studied using a scanning electron microscope (SEM).

2.3. Results and Discussion

Initiation and propagation behavior of fatigue damage in AA 7075 were studied for pure bending, pure torsion, and in-phase multiaxial bending-torsion loadings. Initial tests were conducted with pure bending and pure torsional load conditions in order to gain better insight into the mechanisms governing the combined bending-torsional load and to segregate the effect of multiaxiality from uniaxial bending or torsional loading. Table 2.2 shows a summary of the experimental results for all the different load conditions, where τ_{max} = maximum shear stress due to torsional and bending loads, N_f = fatigue life, L= length of mode I dominant crack, L_{avg} = average length of mode I dominant crack, θ = orientation of mode I dominant crack, θ_{avg} = average orientation of mode I dominant crack. Load 4 and Load 5 correspond to the result of tests conducted under pure bending and pure torsion respectively, whereas, Load 1 – Load 3 are the result of combined bending-torsion tests.

Table 2.2:

Result from bending-torsion fatigue tests.

Load Case	Test ID	τ_{max} (MPa)	N_f (cycles)	L (mm)	L_{avg} (mm)	θ (°)	θ_{avg} (°)
Load 1	B3S4	388	30 195	2.1	2.4	49	48
	B3S5	388	26 233	2.65		48	
	B3S6	388	39 456	2.52		47	
Load 2	B2S2	305	82 584	4.56	4.2	46	45.8
	B2S3	305	84 159	4.92		47	
	B3S11	305	92 351	2.96		43	
	B3S12	305	55 586	4.18		47	
	B3S13	305	51 091	4.4		46	
Load 3	B3S8	257	301 869	6.35		43	42.3
	B3S9	257	296 964	6.51		42	
	B3S10	257	75 707	4.51		42	
Load 4	B2S8	251	54 476	-	-	-	-
	B2S9	251	393 132	-	-	-	-
	B2S10	251	76 135	-	-	-	-
Load 5	B3S1	145	$> 6.1 \times 10^5$	-	-	-	-
	B3S2	220	$> 4.1 \times 10^5$	-	-	-	-
	B3S3	266	$> 3.3 \times 10^5$	-	-	-	-

2.3.1. Fatigue Life

In pure bending, multiple coupons were tested at a selected bending load (Load 4). The value of bending load was selected in order to conduct a low-cycle fatigue test (N_f < ~10^5 cycles) without getting a fatigue runout. For the pure bending tests conducted below the selected load (P_{max} = 8600N), a fatigue runout was observed. Since, in all the cases, fatigue cracks nucleated on the plane of maximum shear stress range (explained in the next section), fatigue life is discussed against the values of maximum shear stress obtained in each load condition, i.e. in pure bending, pure torsion, and combined bending-torsional loading. In the case of combined bending-torsional loading (Load 1 - Load 3), the values of shear stress on a stress element at the neutral axis was simply determined by adding the individual shear stress values calculated from the flexure formula and the torsion formula since both the loads were acting in-phase. As shown in Table 2.2, variability in fatigue life was observed

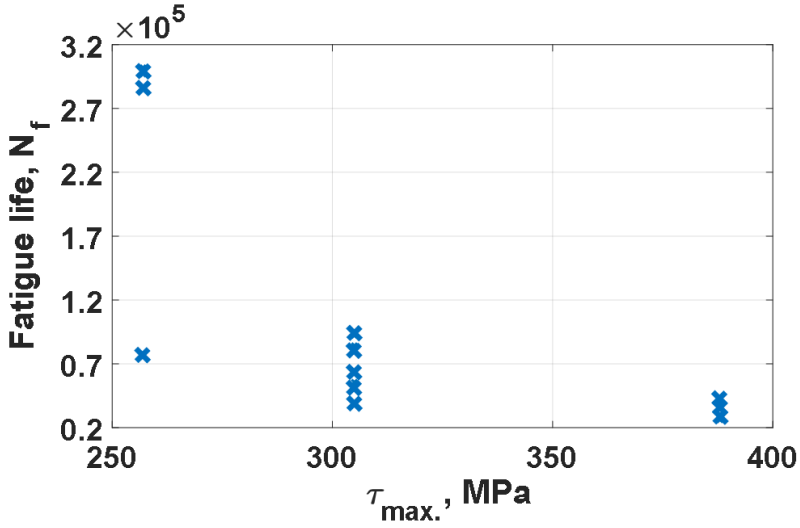

Figure 2.5: Plot of total fatigue life against the maximum value of shear stress under in-phase bending-torsion loading.

for different specimens tested under the same loading condition in pure bending load (Load 4); whereas, specimens tested under pure torsional load exhibited fatigue runout and crack nucleation could not be observed, even though the maximum value of shear stress in pure torsion was higher than the shear stress in pure bending load.

For multiaxial in-phase bending - torsion loads, specimens were investigated at three different stress levels (Load 1 – Load 3) as summarized in Table 2.2 and the variations in fatigue life are presented in Figure 2.5. As shown in Figure 2.5, higher fatigue life is obtained by reducing the value of maximum shear stress. An overall decrease of 34% in the shear stress value led to a six-fold increase in the average fatigue life. It is important to note that a high degree of scattering was observed in fatigue life at lower stress value, which was annihilated at a higher value of shear stress.

2.3.2. Crack Nucleation

Since crack did not nucleate in the specimens tested under pure torsional load, the subsequent sections compare and contrast the results of the tests conducted under pure bending and combined bending-torsion loads. Fatigue crack developed under pure bending load is shown in Figure 2.6. For all the tested coupons, a single crack nucleated on the surface of the specimen and was located on the plane of maximum shear stress (i.e. neutral axis), as shown in Figure 2.6(b). For multiaxial in-phase bending-torsion load, fatigue cracks propagating under three different stress levels are shown in Figure 2.7. In all the tests, irrespective of the applied load magnitude, a single crack nucleated (at point I) on the surface of the specimen similar to the result of pure bending tests, as shown in Figure 2.8(a). The crack nucleated at a point where the range of shear stress was maximum (i.e. plane of

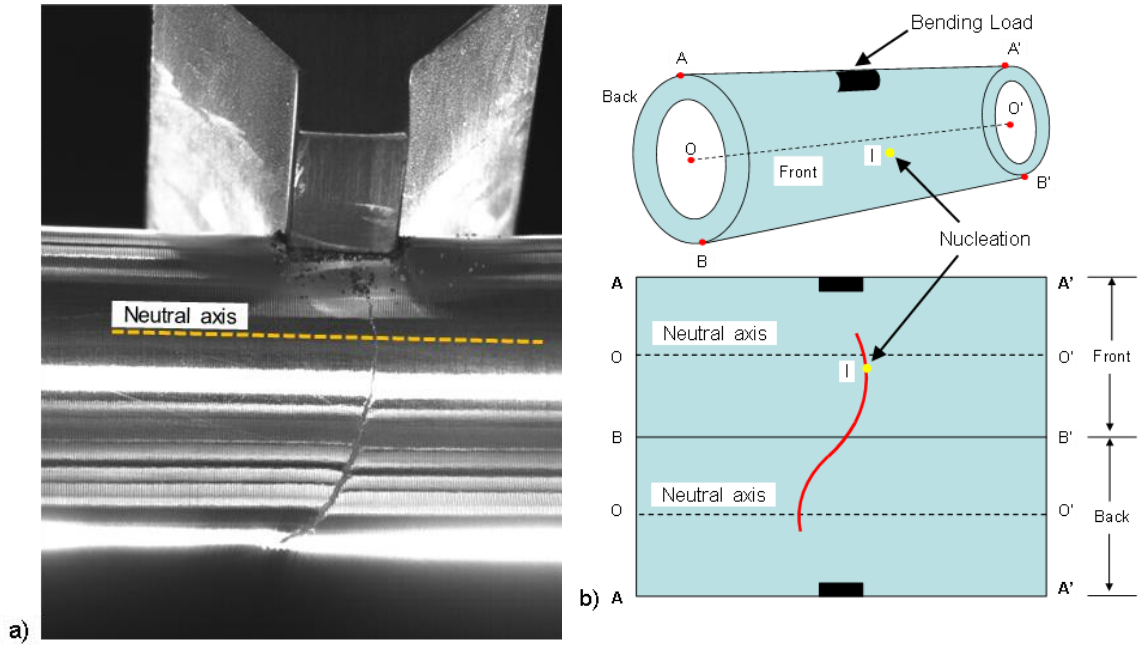

Figure 2.6: a) Actual crack trajectory, and b) schematic of the crack trajectory for the failed coupons tested under pure bending load.

maximum shear stress). These observations along with the similarities in crack initiation showed by different types of loading emboldens the fact that the fatigue cracks in a pristine specimen tend to nucleate on the planes of maximum shear stress; and in a high strength material, such as AA 7075, fail by a single dominant microcrack. It is evident from the literature that smooth specimens of a ductile material can develop several microcracks leading to multiple nucleation sites; however, high strength materials and/or tubular specimens exhibit very low tendency to develop multiple crack initiation sites and thus fail by a single dominant crack [21,58]. Additionally, there is extensive experimental evidence [40,50,58,59] in the literature supporting the hypothesis that naturally occurring fatigue cracks tend to initiate on planes of maximum shear stress.

2.3.3. Crack Propagation

Crack propagation in fatigue fracture can be divided into three stages, i.e. stage I, stage II and stage III. Stage I corresponds to the immediate growth of crack following nucleation, which propagates on the plane of maximum shear stress for a very short distance (may or may not be visible on a macroscopic scale), via mode II or/and mode III crack growth. In stage II, stable crack growth is observed, which may propagate via mode I or mode II or mix-mode mechanism, depending on the applied stress-state. Stage III is the final stage in which unstable crack growth leads to a fast fracture of the specimen.

Figure 2.6 shows a fully developed crack trajectory of a representative specimen of the tests conducted under pure bending load. As shown in Figure 2.6(b), crack traced the path to maximize mode II crack growth and predominantly grew on the planes of maximum shear stress in a continuously varying mix-mode condition. During the crack propagation, the value of mode mixity, ϕ_M, changed from Π/2 (pure mode II) at the neutral axis to Π/4 at the specimen's bottom region. As shown in Figure 2.6(b), an inverted *S*-shaped antisymmetric crack trajectory was obtained in which orientation of the crack with respect to longitudinal axis gradually deflected from approximately 90° at the neutral axis (front face) to approximately 45° at the bottom of the specimen (diametrically opposite to the applied bending load) and then again back to approximately 90° at neutral axis (back face). Since bending load introduces stress gradient (differently for shear stress and tensile stress) in the transverse direction, the local value of λ and ϕ_M at crack tip continuously changed with crack propagation. As a result, continuous deflection of crack orientation was observed, leading to a curved trajectory.

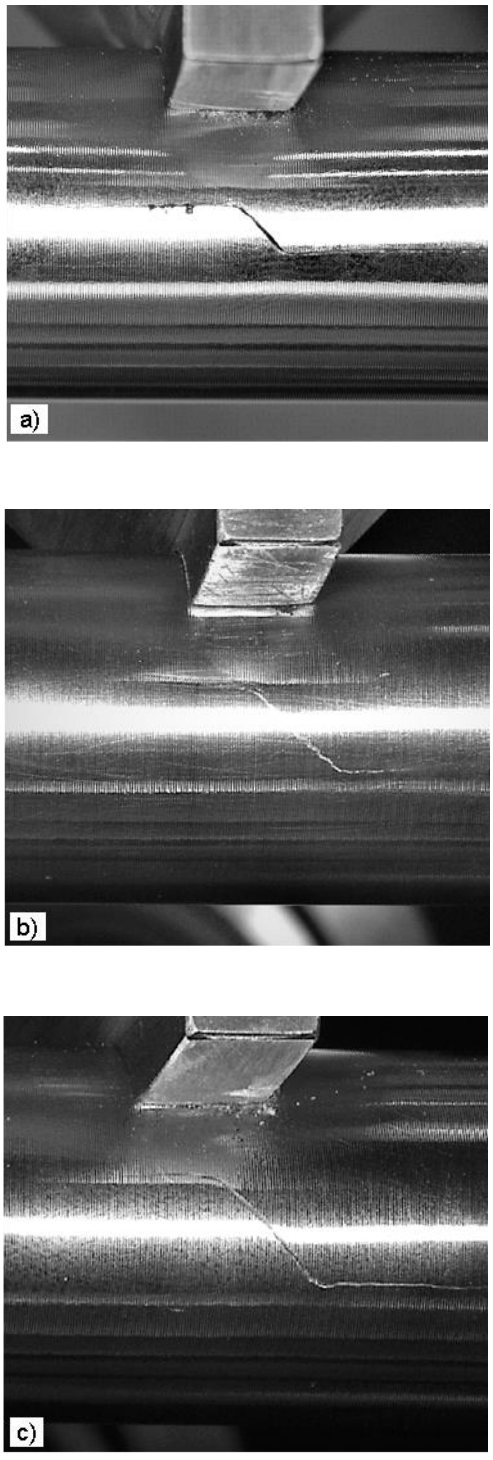

Figure 2.7: Fatigue crack trajectory under in-phase bending-torsion load: a) Load 1; b) Load 2; and c) Load 3.

Macroscopic fatigue cracks developed under combined bending-torsion load is shown in Figure 2.8. As shown in Figure 2.8(a), nucleation was immediately followed by a stable stage II crack propagation that defined crack trajectory and indicated different modes of crack growth (i.e. mode I, mode II or mix mode). Clearly, the propagation behavior of the fatigue crack can be characterized by dividing the crack trajectory into three regions: mode I dominant mix-mode region, crack transition region, and pure mode II region. As shown in Figure 2.8(a), orientation of the initial crack aligned closely with the maximum principal stress plane and thus showed mode I dominant growth. At the onset of stage II growth, initially, crack propagated on the plane of maximum principal stress, but because of the existing stress gradient (both for normal and shear stress) in the transverse direction, the magnitude and the direction of principal stress continuously changed at the crack-tip even though the crack propagated in its initially inclined direction. In other words, crack propagated in mode I dominant mix-mode loading due to a monotonic increase in the local value of λ and ϕ_M at the crack tip. Once the crack reached a critical length, a gradual deflection in the crack tip was observed to maximize mode II crack growth, which turned the crack completely in the direction of the longitudinal axis. After deflection, the crack propagated in pure mode II through the entire length of the gauge region until specimen failure. Experimental evidence suggests that the mode of crack growth in a smooth specimen depends on multiple factors including material, load magnitude, stress amplitude ratio, initial crack tip condition, mean stress and anisotropy [19]. For a crack, growing in mix-mode load condition, it is difficult to predict the orientation of crack growth as the crack can continue to grow in mix-mode or can deflect either to shear mode or to tensile

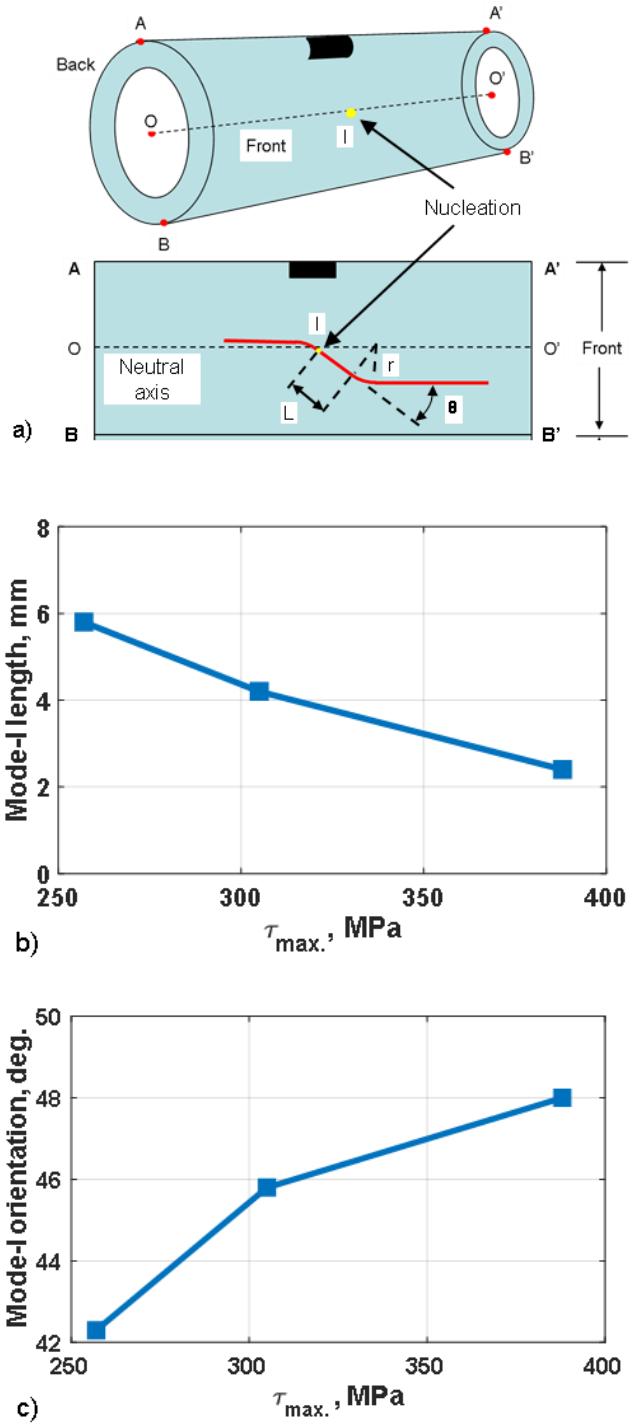

Figure 2.8: a) Schematic of crack trajectory for coupons failed under in-phase bending-torsion load. b) Average length of mode I dominant crack, and c) Average orientation angle of crack plotted against maximum value of shear stress in combined bending-torsion load.

mode depending upon the stress state near the crack tip. The transition of crack to tensile mode (mode I) is shown in several fatigue studies in literature, while only a few studies have reported the transition of crack to shear mode [60]. It has been observed in the past that the crack preferably deflects to a shear mode growth only when two conditions are simultaneously satisfied at the crack tip: a) stress intensity factor (SIF) in shear mode exceeded a critical value and; b) the value of λ or ϕ_M exceeded a critical value [19,50]. Since these critical values are sensitive to many parameters, such as material, microstructure, specimen geometry, crack-tip conditions, etc., quantitative information that could provide their accurate values has not been reported in the literature.

2.3.4. Effects of Load Magnitude and Microstructural Characterization

The effect of change in stress value was also investigated under multiaxial in-phase bending-torsion loading. A consistent behavior in fatigue crack initiation and crack trajectory was observed with various coupons tested under different sets of loading conditions mentioned in Table 2.1. It is important to note that despite having similarities in crack trajectories, magnitude of the applied load significantly affected the length of mode I dominant crack (L), orientation of mode I dominant crack (θ), and curvature of the crack deflection (Figure 2.8). As shown in Figure 2.8(b), the average length of mode I dominant crack increased with a decrease in the value of maximum shear stress. An overall decrease of 34% in shear stress led to an increase in average L by 1.4 times. On the other hand, the average value of the crack orientation angle decreased with a decrease in maximum shear stress and is shown in Figure 2.8(c). Here, a decrease in shear stress by 34% led to a decrease in the average value of θ by 12%. Moreover, deflection of the crack

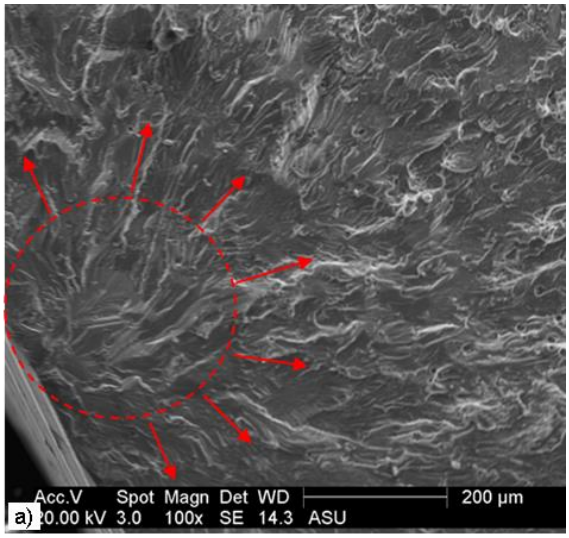
Acc.V Spot Magn Det WD 200 µm
20.00 kV 3.0 100x SE 14.3 ASU
a)

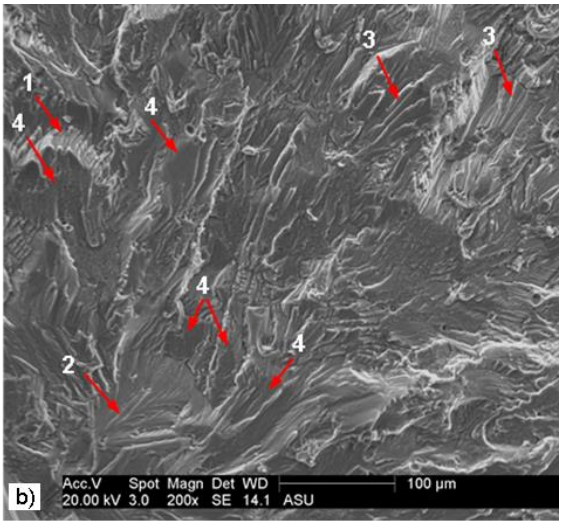
1
4
4
3
3
4
4
2
Acc.V Spot Magn Det WD 100 µm
20.00 kV 3.0 200x SE 14.1 ASU
b)

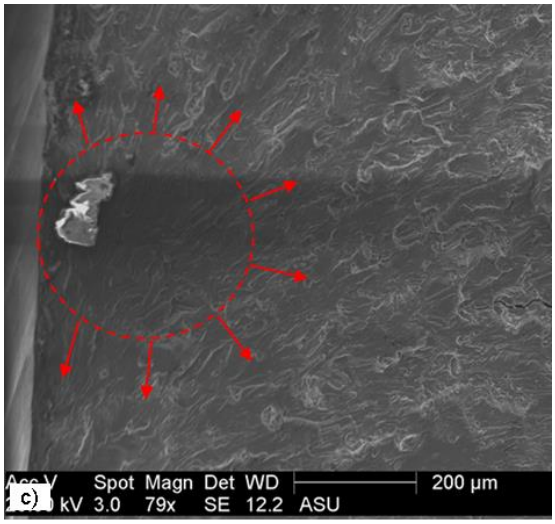
Spot Magn Det WD 200 µm
3.0 79x SE 12.2 ASU
c)

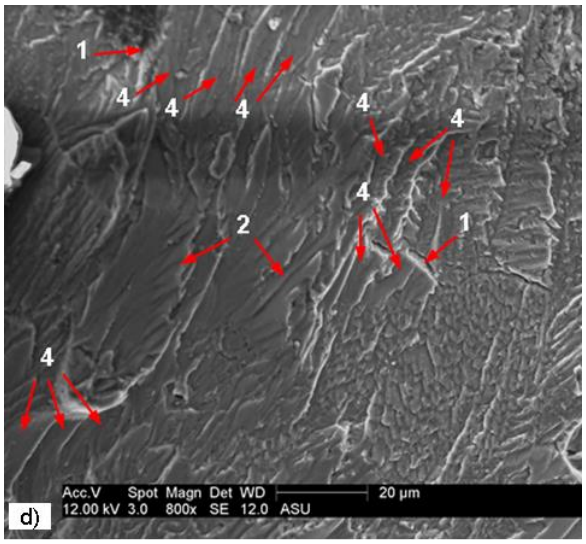

Figure 2.9: Fracture surfaces of specimens showing nucleation and stage I growth during: a) and b) Load 1 condition; c) and d) Load 3 condition. Fracture features are marked: 1– flute, 2–feather marking, 3– serpentine glide, 4– cleavage steps.

during crack transition became sharper as the testing load (maximum shear stress) was increased. These observations indicate that the mode-mixity at the crack tip and the dominance of shear mode in the mix-mode crack growth increases with the increased value of the applied load or maximum shear stress for the tests conducted at the constant value of λ.

Microstructural characterization of the fatigue-fracture surfaces was conducted with the help of SEM. The various fracture features, thus obtained, were analyzed to correlate the fracture surface morphology with the initiation and propagation of the fatigue crack under various loading conditions (combined bending-torsion load). Several distinct features were observed on the fracture surface in the regions of crack nucleation, stage I propagation, and stage II propagation. A considerable variation in the fractographic features was also observed when the stress amplitude in the specimens was changed.

SEM images of a typical stage I fatigue fracture, including crack nucleation, at two different values of applied stresses (Load 1 and Load 3) are shown in Figure 2.9. Irrespective of the applied stress level, stage I crack exhibited distinct features of cleavage fracture, such as river pattern, cleavage steps, facets, feather marking, flutes, and serpentine glide, suggesting the brittle nature of fracture [61–63]. As shown in Figure 2.9(a) and (c), cleavage fractures initiated on multiple parallel cleavage planes forming a river pattern and pointing back towards the origin of the fracture. Magnified pictures of the fracture surfaces reveal a highly tortuous path along with a higher degree of brittleness for the specimen tested under a higher stress value in comparison with that tested under lower stress value, as shown in Figure 2.9(b) and (d). Among all the characteristic features, cleavage steps are most frequently observed and are spread across the entire region. Some of the large cleavage facets exhibited an array of very fine cleavage steps, also known as feather marking. Flutes, which are elongated grooves that connect widely spaced cleavage planes, are also observed on the fracture surfaces. Comparing the fracture surfaces under two different loadings, it was observed that these features tend to appear more frequently for higher values of applied stress.

Fracture surfaces during stage II crack growth were analyzed by dividing the crack region into two segments. Segment-1 represents the portion of stage II growth in which macroscopic crack propagated in mode I dominant mix-mode loading (between nucleation and start of crack turning), while segment-2 represent macroscopic crack propagation in mode II loading after crack turning (Ref. Figure 2.8(a)). SEM images of segment-1 under

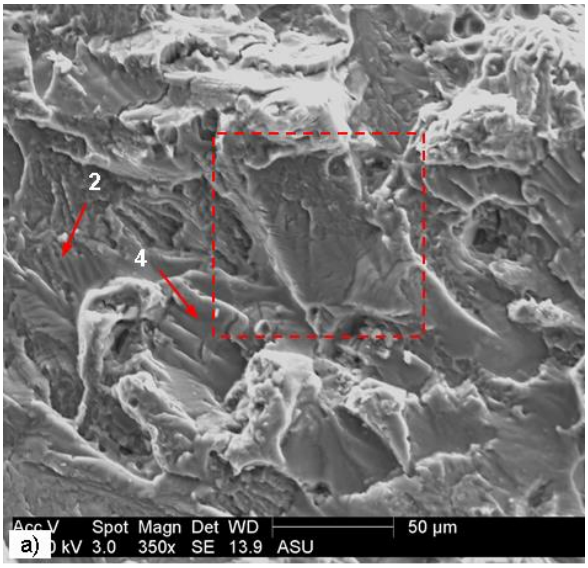
2
4
Acc.V Spot Magn Det WD 50 µm
a) kV 3.0 350x SE 13.9 ASU

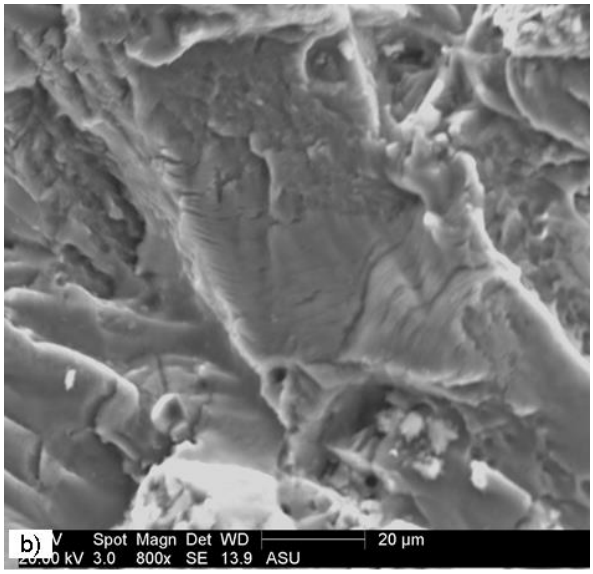
b) Spot Magn Det WD 20 µm
kV 3.0 800x SE 13.9 ASU

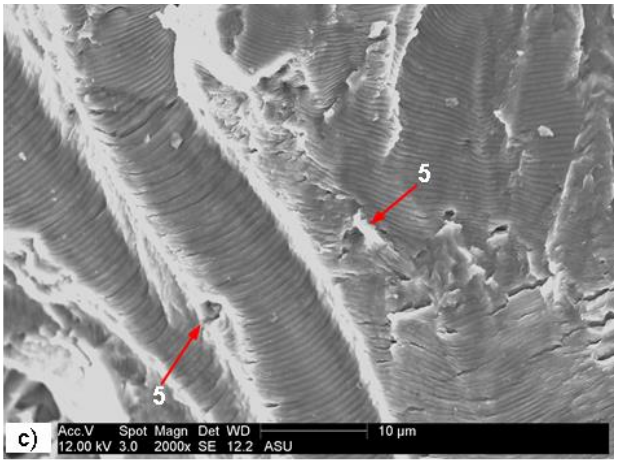
5
5
c) Acc.V Spot Magn Det WD 10 µm
12.00 kV 3.0 2000x SE 12.2 ASU

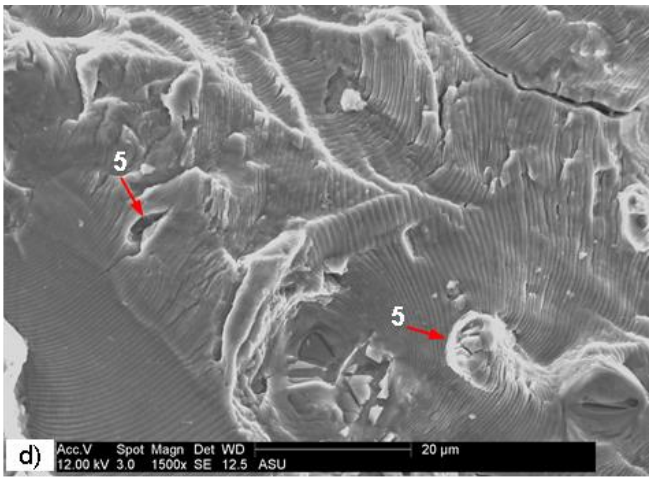

Figure 2.10: Fracture surfaces of specimens showing stage II crack growth in segment-1 during: a) and b) Load 1 condition; c) and d) Load 3 condition. Fracture features are marked: 2–feather marking, 4–cleavage steps, 5–secondary crack.

two different stress levels, i.e. high stress (Load 1) and low stress (Load 3), are shown in Figure 2.10. In Figure 2.10(a) and (b), the characteristic features of the fracture surface at a higher stress value (Load 1) is illustrated, which clearly shows the presence of cleavage steps and feather marks, similar to that of stage I crack, in addition to the striation marks. It is important to note that the striations are partially developed and are present only in a few localized regions. A magnified SEM image, as shown in Figure 2.10(b), clearly shows partial annihilation of these striations. Although the macroscopic crack appears to be mode I dominant, the SEM results of fractured surface indicate that the crack propagates in a mix mode condition where the effect of mode II loading is significant. On the contrary, fracture surface at lower stress level (Load 3) exhibited well-developed, fully grown striations as shown in Figure 2.10(c) and (d). Figure 9(c) shows fatigue striations developed on different ridges, in which the walls of adjacent ridges are well connected with the continuously growing striations propagating in the same direction. However, variations in local stresses

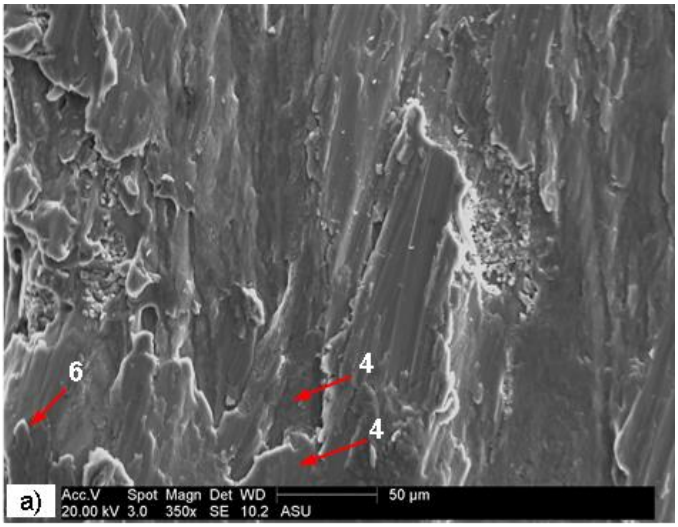
6
4
4
a)
Acc.V Spot Magn Det WD
20.00 kV 3.0 350x SE 10.2 ASU
50 µm

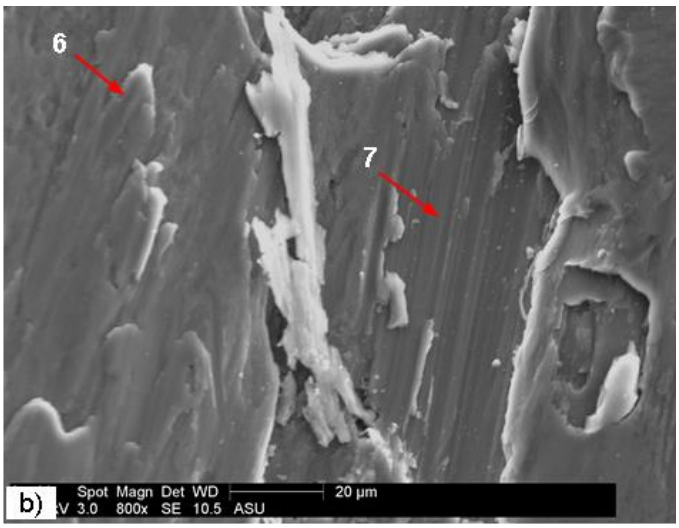
6
7
b)
Spot Magn Det WD
V 3.0 800x SE 10.5 ASU
20 µm

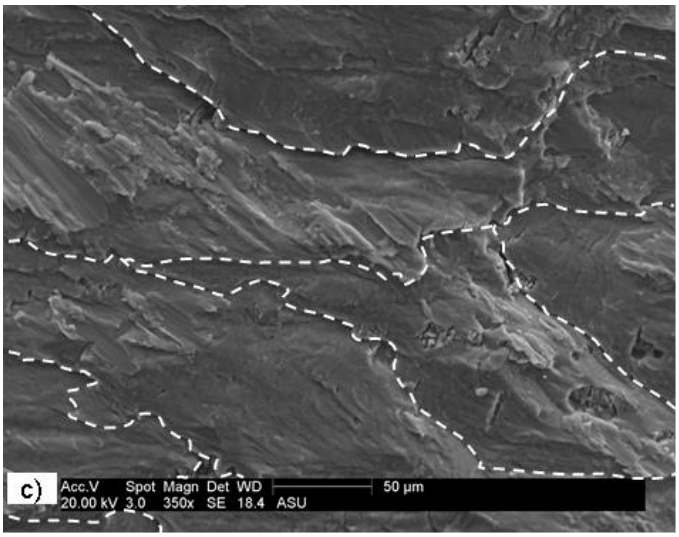
c)
Acc.V Spot Magn Det WD
20.00 kV 3.0 350x SE 18.4 ASU
50 µm

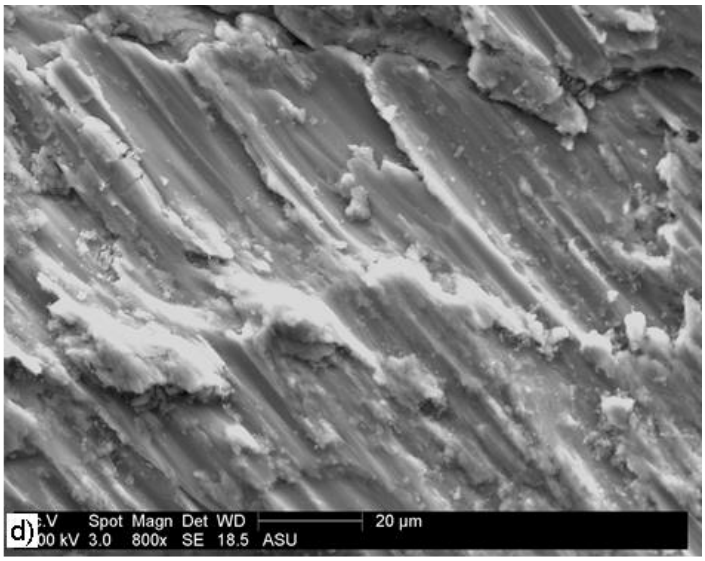

Figure 2.11: Fracture surfaces of specimens showing stage II crack growth in segment-2 during: a) and b) Load 1 condition; c) and d) Load 3 condition. Fracture features are marked: 4–cleavage steps, 6–Tongue, 7–Tire track.

and microstructure can change the orientation of the fracture plane and subsequently alter the direction of striation alignment, as shown in Figure 2.10(d). Furthermore, secondary cracks were also observed at multiple locations, which were generated due to the interaction of inclusions / hard particles with the propagating striations. These observations agree with the result of macroscopic crack growth mode and support the fact that the crack growth is primarily dominated by mode I loading at a lower stress level.

Figure 2.11 shows SEM images of segment-2 during high stress and low stress conditions. At higher stress, as shown in Figure 2.11(a) and (b), the fracture surface showed some interesting features. In addition to the cleavage steps, tongues were observed for the first time, which are formed when a cleavage fracture deviates from the cleavage plane and propagates a short distance along a twin orientation [61]. On magnification, distinct and

periodic markings can be observed on the surface, which is also known as tire track and is shown in Figure 2.11(b). These rows of parallel markings are the result of particles or protrusions on one surface being successively impressed into the surface of the mating half during the closing portion of the fatigue cycle in shear loading [61]. Unlike these observations, fracture surface at lower stress value predominantly showed an intergranular fracture, as shown in Figure 2.11(c). Tire tracks were also observed at higher magnification (Figure 2.11(d)) but they were not continuously spread on the surface and were spotted only at very few locations.

2.4. Governing Micromechanisms for Fatigue-Fracture Behavior

Fatigue crack initiation in a smooth specimen is governed by several competing mechanisms that are dependent on various mechanical, microstructural and environmental factors. On the application of cyclic load, intrusions and extrusion emerge on the surface of the specimen forming persistent slip band (*PSB*). During the loading portion of the cycle, slip occurs on the crystallographically favored plane, i.e. plane having maximum value of critically resolved shear stress (τ_{CRSS}) or Schmidt factor (m); whereas, during unloading, reverse slip occurs on a parallel plane because the slip on the original plane is inhibited by the hardening or/and the oxidation of the newly formed free surface. These cyclic slips continuously form extrusions and intrusions, which in turn leads to *PSB*s. The interface between the *PSB* and the matrix is a plane of discontinuity across which there are abrupt gradients in the density and the distribution of dislocations. In that case, when the *PSB*s interact with the existing structural defects, such as second-phase particles/inclusions, grain boundaries, a highly stressed region is formed around the defects due to the accumulation

of dislocations. Since the second-phase particles/inclusions are brittle and the matrix is ductile, crack is nucleated in a single shear when the critical elastic strain energy is reached inside the particle at the site of dislocation pile-up [1,64,65].

Crack growth behavior can be influenced by distinct concurrent and mutually competitive mechanisms, which can act either ahead of the crack tip or in the wake region of the crack. These mechanisms may include interlocking of fracture surface asperities, friction and roughness induced crack closure introduced by mode-mixity; crack tip blunting and strain hardening due to localized plastic deformation near the crack tip resulting in higher fracture toughness; crack closure caused by crack tip shielding due to compressive residual stresses ahead of the crack-tip; and plasticity induced crack closure caused by increased plasticity resulting from mode-mixity at crack tip. With the growth of stage II crack, the component of mode II load, in mode I dominant mix mode loading increased monotonically at the crack tip due to the presence of stress gradient along the transverse direction of the specimen. Since the size of the plastic zone in mode II is up to five times bigger than that in mode I for the same amplitude of far-field loading [1], an increase in mode II component of the load implied a larger plastic zone size at the crack tip as compared to the pure mode I load resulting in the attenuation of effective stress intensity factor (*SIF*), which is also the effective crack driving force. The larger size of the plastic zone was further manifested in the form of crack tip blunting, strain hardening, compressive residual stress and plastic wake, which in turn led to the enhancement of crack closure level and resulted in an additional reduction in the effective *SIF*. When the crack reached a certain critical length, where the value of ϕ_M was increased to a sufficiently

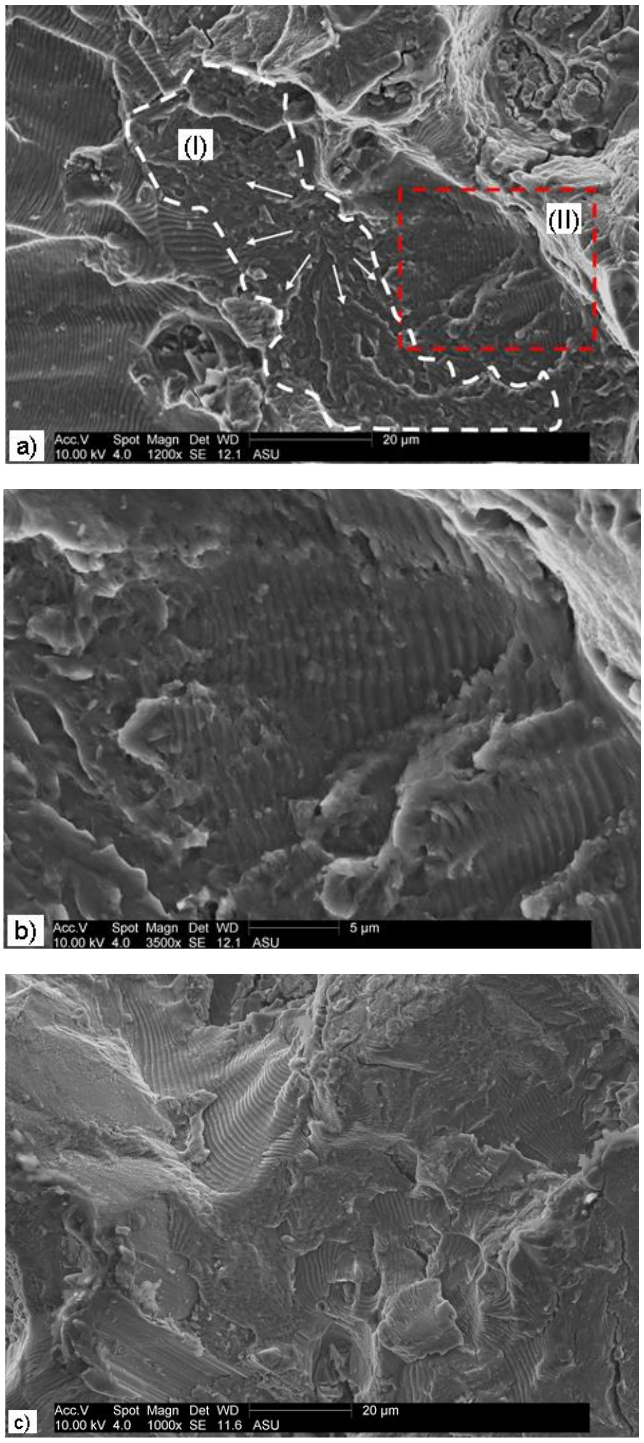

Figure 2.12: Fracture surface topology in crack transion region of the specimen fatigued under Load 1 condition: a) micrograph showing the regions of crack arrest and crack re-initiaion; b) Magnified image of region (II) showing stage II growth in re-initiated crack; c) micrograph showing crack arrest and crack re-initiaion on the other mating half of the fracture surface.

higher value, the size of the plastic zone became large enough to attenuate the effective *SIF* below the threshold *SIF* needed for the advancement of crack, which resulted in the crack arrest. After several fatigue cycles, the crack reinitiated on the crystallographically favored plane (maximum shear plane) deviating from its initial direction but grew only a small distance before being arrested again owing to the larger plastic zone resulting from the increased shear stress on the new crack plane. This cycle of incremental deviation and growth followed by crack arrest and re-initiation was continued till the crack face became parallel to the longitudinal axis. With each incremental deflection, the local stress state at the crack tip changed due to the rotation of stress element resulting in a higher value of shear stress or mode II component of loading. Once the crack became parallel to the longitudinal axis, the crack tip was exposed to pure mode II load having the maximum value of shear *SIF* that propagated the crack till failure. For the case when the applied external stress in the specimen was large, the critical size of the plastic zone responsible for bringing the effective *SIF* below the threshold value was achieved at a smaller crack length, leading to the decrease in the length of mode I dominant crack as shown in Figure 2.8(a). Because of the smaller crack length, a smaller value of crack tip opening displacement would occur resulting in an enhanced mode II induced crack closure. Furthermore, during the re-initiation phase of crack on the plane of maximum shear stress, the incrementally deflected crack experiences a higher increase in shear stress resulting in an increased plastic zone and more pronounced crack closure. Consequently, each time, crack re-initiation was followed by crack arrest after a relatively small growth, which led to a sharper deflection (smaller ‘r’) of mode I dominant mix-mode crack to pure mode II

crack at higher stress levels as compared to the lower stress level, where a gradual transition (larger r) was observed.

The experimental evidence obtained from the investigation of fracture surfaces in crack transition region corroborates the proposed mechanism for crack turning from mode I dominant mix mode growth to the pure mode II growth while capturing the effect of change in the magnitude of applied stress, as shown in Figure 2.12. Figure 2.12(a) depicts the entire phenomena involved in crack deflection process in a sequential manner (from left to right): crack arrest for mode I dominant crack propagation, crack re-initiation and stage I growth (region (I)), stage II crack propagation (region (II)). First, the crack propagated in mode I dominant load indicated by the well-developed and fully-grown striations traveling (left to right) on various planes, which suddenly stopped, implying crack arrest. Second, crack re-initiation occurred on an adjacent plane (region (I) in Figure 2.12(a) as indicated by the presence of river marking and small cleavage steps. Third, stage I propagation was immediately followed by stage II propagation (region (II) in in Figure 2.12(a)) as indicated by the formation of striations. An enlarged SEM image of stage II propagation is shown in Figure 2.12(b), which shows a rapid increase in striation distance over a short distance. This sequence was repeatedly observed on the fracture surface supporting the proposed mechanism. Furthermore, investigations were also conducted on the other mating half of the fracture surface, as shown in Figure 2.12(c), where the entire phenomena of crack deflection process were found to be repeated.

2.5. Non-Proportional Loading

In many cases, engineering components undergo complex multiaxial loadings that lead to the change in direction of principle stress during each cycle of fatigue loading. Such loading causes additional hardening in the material due to the rotation of principle stress and is considered to be the primary reason for the reduction of fatigue life under non-proportional loading as compared with that under proportional loading [66]. Among several other factors, crack initiation and propagation also depend on phase difference during non-proportional loading scenario [26], and therefore, it is important to investigate the effect of non-proportional loading under multiaxial bending and torsional load condition.

Non-proportional fatigue tests were conducted for bending - torsion coupled load conditions, which are summarized in Table 2.3. These tests were conducted at phase difference (φ) of 0°, 45°, and 90° and for each value of phase difference 3 specimens were tested. Similar to the proportional bending-torsional fatigue tests, all the non-proportional fatigue tests were carried out at a constant value of stress amplitude ratio ($\lambda = 0.6$) at room temperature. Using the experimental set-up shown in Figure 2.4, non-proportional fatigue tests were conducted under constant amplitude sinusoidal loads at a frequency of 1 Hz and a load ratio (R) of 0.1, for which load spectrum is shown in Figure 2.13. Under this investigation, fatigue cycle for the failure is considered when the specimen is completely broken into two pieces.

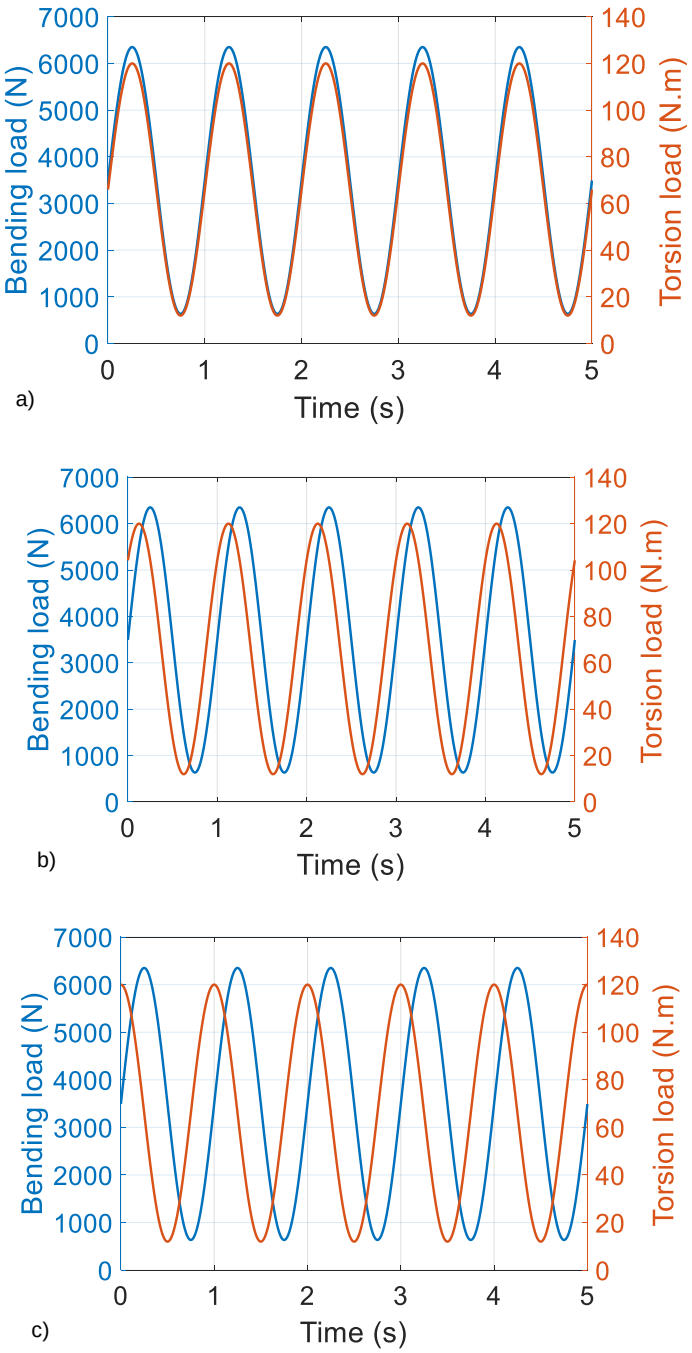

Figure 2.13: Load spectrum used in non-proportional bending-torsion fatigue tests with a phase difference of: a) 0 degree; b) 45 degree; and c) 90 degree.

Table 2.3:

Loading conditions for non-proportional bending-torsion tests.

Test ID	R-Ratio	P_{max} (N)	T_{max} (N.m)	Freq (Hz)	τ_T (MPa)	σ_b (MPa)	λ (τ_T / σ_b)	ϕ	N_f (cycles)
PBT-T1S1	0.1	6350	120	1	145	260	0.60	0°	102584
PBT-T1S2	0.1	6350	120	1	145	260	0.60	0°	102584
PBT-T1S3	0.1	6350	120	1	145	260	0.60	0°	119851
NBT-T1S1	0.1	6350	120	1	145	260	0.60	90°	86504
NBT-T1S2	0.1	6350	120	1	145	260	0.60	90°	69723
NBT-T1S3	0.1	6350	120	1	145	260	0.60	90°	78181
NBT-T2S1	0.1	6350	120	1	145	260	0.60	45°	51271
NBT-T2S2	0.1	6350	120	1	145	260	0.60	45°	67500
NBT-T2S3	0.1	6350	120	1	145	260	0.60	45°	44625

2.5.1. Fatigue Life

Figure 2.14 shows the fatigue life of the specimens under bending-torsion coupled loading investigated at three different values of phase difference (ϕ), i.e. 0°, 45°, and 90°. As shown in Figure 2.14, fatigue life of the specimen under proportional / in-phase loading (ϕ = 0°) is higher than that under non-proportional loading (ϕ = 45° and 90°). Among the conducted tests, the minimum fatigue life is observed when there is a phase difference of 45° between the bending and the torsional loading.

Lower fatigue life under non-proportional multiaxial loading is associated with change in direction of the principal stress or strain in ductile materials. As a result, dislocations are

activated in different directions blocking each other, which leads to the so-called multiaxial stress hardening. This multiaxial stress hardening under non-proportional loading causes lower fatigue life as compared to in-phase loading with constant principal stress direction [67–69].

There is a plethora of evidence in the literature confirming the relation between the dislocation structure in the non-proportional loading conditions [70–72] and an extra hardening of the material. Socie *et al*. [73] showed that the hardening curve stress values for phase shift angle equaling 90° are twice as big in relation to those achieved in the non-proportional loading conditions. Later, Fatemi *et al*. [74] proved that there is a relation between the extra hardening and the decreasing fatigue life. They showed that the increase in extra hardening by 10–15% caused the reduction of the life by half. When the extra hardening was larger by 100%, the life was ten times shorter. Also Socie *et al*. [73], on the basis of their study, estimated that the life in non-proportional loading conditions may be even ten times smaller.

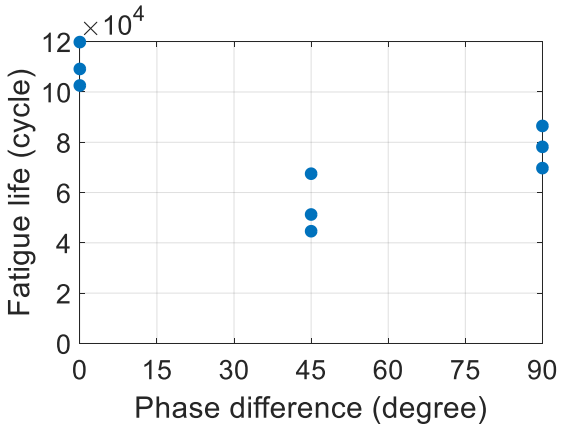

Figure 2.14: Plot of total fatigue life against phase difference in a non-proportional bending-torsion fatigue.

In characterizing fatigue response of materials under multiaxial loading, mode of local deformation is an important parameter to be considered [67]. When the applied load is in macroscopically elastic range, lower fatigue life is obtained under non-proportional loading for both the load-controlled and the deformation-controlled experiments whether notched or smooth specimen is used. However, if the applied load is in macroscopically plastic range, smooth specimens under load-controlled experiments show quite different result in which lower fatigue life is obtained under in-phase loading instead of out-of-phase (non-proportional) loading [67,68]. The higher fatigue life observed under non-proportional loading is mainly caused by the smaller increase of local deformations when compared to in-phase loading where uncontrolled increase in deformation occurs. Using deformation control, which eliminates the uncontrolled increase in deformation of smooth specimens and simulates the constraint present in notched specimens, the fatigue life under non-proportional loading is lower in comparison to in-phase loading [68]. It is important to note that the ductile metallic materials interact in a different way to non-proportional loading with changing principal stress or strain directions than brittle and semi-ductile metallic materials. An increase in fatigue life is observed under non-proportional loading for low-ductility (so-called brittle) materials but for semi-ductile materials no difference was observed between in and out-of-phase multiaxial loading [71].

2.5.2. Crack Initiation

For all the tests conducted either under in-phase (ϕ = 0°) loading or under non-proportional loading with phase difference of 45°, a single crack nucleated on the surface of the specimen and was located on the plane of maximum shear stress (i.e. neutral axis),

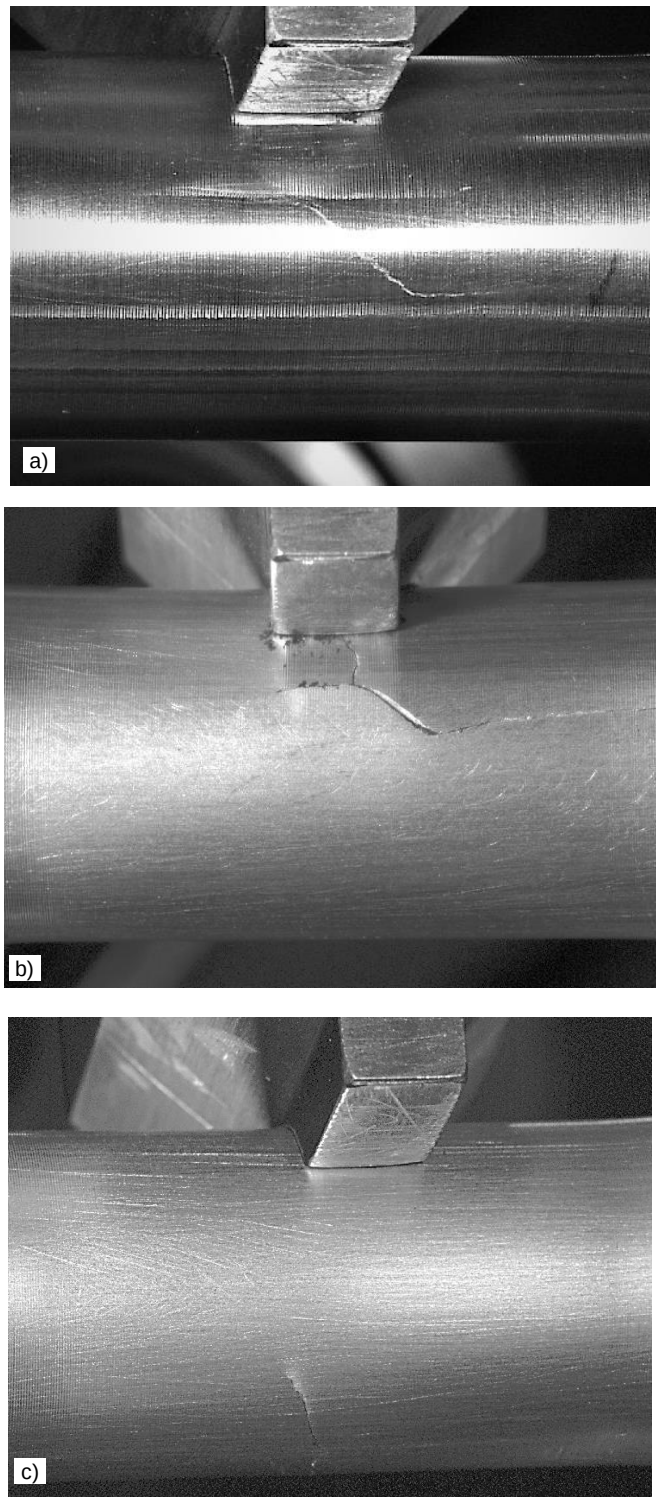

Figure 2.15: Crack trajectory under non-proportional bending-torsion fatigue with a phase difference of: a) 0 degree; b) 45 degree; and c) 90 degree.

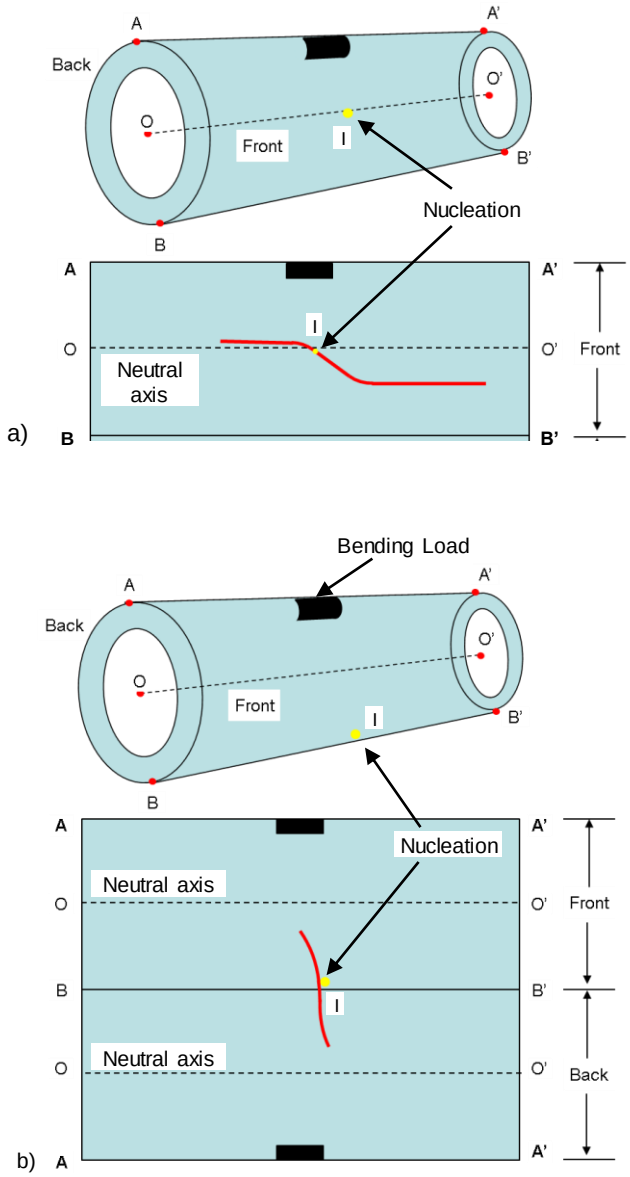

Figure 2.16: Schematic of crack trajectory of coupons failed under non-proportional bending-torsion fatigue with a phase difference of: a) 0 degree or 45 degree; b) 90 degree.

as shown in Figure 2.16(a). However, in the case of non-proportional loading with phase difference of 90°, again a single crack was nucleated but it was located on the plane of maximum bending stress as shown in Figure 2.16(b).

From the literature, it is evident that smooth specimens of a ductile material can develop several microcracks leading to multiple nucleation sites; however, high strength materials and/or tubular specimens exhibit very low tendency to develop multiple crack initiation sites and thus fail by a single dominant crack [3,22]. Furthermore, the experimental results reported in the literature supports the hypothesis that naturally occurring fatigue cracks, under in-phase loading (ϕ = 0°), tend to initiate on the planes of maximum shear stress; whereas, under non-proportional loading (ϕ = 90°), some studies reported that the crack was initiated at plane of maximum shear stress [47] while the other studies reported that it was initiated at the plane of maximum principle stress [75].

2.5.3. Crack Propagation

Under non-proportional loading, the fatigue crack is expected to experience a mix mode stress state with the mode-mixity ratio, $\phi_M = K_{II}/K_I$ (K_{II} = mode II *SIF*, K_I = mode I *SIF*), varying with the direction of the crack. The crack paths under different phase differences in loading are shown in Figure 2.15 and Figure 2.16. During in-phase loading (ϕ = 0°) as well as 45° out-of-phase loading, crack traced similar trajectories as shown in Figure 2.16(a). The entire crack trajectory can be divided into three regions: a) initially after nucleation near neutral axis, one end of the crack propagated towards the bottom of the specimen at approximately 45° from longitudinal axis; b) After propagating for a short distance, the crack deflected sharply towards the longitudinal axis and continued propagating till final failure; c) the other end of the crack (near neutral axis), also showed sharp deflection and continued propagating towards the longitudinal axis but in the opposite direction. However, in the case of 90° out-of-phase loading, crack traced a

different trajectory as shown in Figure 2.16(b). Figure 2.16(b) shows an inverted *S*-shaped antisymmetric crack trajectory, in which orientation of the crack with respect to longitudinal axis gradually deflected from approximately 90° at the bottom of the specimen to approximately 45° as crack tip approached near the neutral axis of the specimen. This behavior of crack trajectory is similar to the crack trajectory obtained under pure bending fatigue loading explained earlier in this chapter [76].

2.6. Conclusion

Thin-walled tubular specimens of AA 7075 were investigated to understand the microscale as well as the macroscale fatigue damage behavior (crack initiation and propagation). Tests were conducted under uniaxial loading (pure bending / pure torsion) as well as multiaxial in-phase bending-torsional loading. Additional tests were conducted for non-proportional bending-torsion fatigue with different phase angles to have a better insight into fatigue damage behavior. The presented results support the following observations:

- Under pure bending load, a single crack nucleated on the plane of maximum shear stress and propagated in an inverted *S*-shaped trajectory.
- In the case of in-phase bending-torsional load, though a single crack nucleated on the plane of maximum shear stress, crack propagation behavior was entirely different from the one observed previously under pure bending load. Here, crack trajectory showed a combination of mode I dominant region, crack transition region, and pure mode II region.

- For the non-proportional bending torsion load, again a single crack was nucleated for all the cases; however, it was located on the plane of maximum shear stress for 45° out-of-phase loading and on the plane of maximum bending stress for 90° out-of-phase loading. The observed crack trajectory for 90° out-of-phase loading was similar to the pure bending load, whereas, the trajectory for 45° out-of-phase loading was similar to the in-phase bending-torsional load.
- Micromechanism governing in-phase bending-torsion fatigue loading:
  - Nucleation was shear dominant brittle cleavage fracture, in which degree of brittleness increased with increase in stress.
  - Mode I dominant growth showed well developed striations at lower stress, but at higher stress partially annihilated striations along with features of cleavage fracture were observed.
  - Crack after deflection showed mode II growth having intergranular fracture at lower stress, but transgranular fracture at higher stress.

3. FATIGUE CRACK GROWTH BEHAVIOR UNDER SHEAR OVERLOADS

3.1. Introduction

Traditionally, fatigue investigations have been conducted under constant amplitude loadings [33,41,76–80]. However, in practical applications, components are often exposed to complex multiaxial load conditions with variable amplitude loading, as shown earlier in Figure 2.1. A few examples of such load conditions include over-/underload experienced by aircraft wings during take-off and landing; overload experienced by the rotor and bearings of the turbo-generator at start-up, etc. [29]. Since the damage tolerant design concepts incorporate the assumption that flaws exist in all structures and propagate according to the existing stress condition, the fundamental understanding of fatigue damage accumulation and propagation under multiaxial loading with overload excursions becomes critical in identifying the governing mechanisms and determining the component's useful life.

It is a well-established fact that the load excursions induce load-interaction effects, which can result in significant acceleration or retardation of the crack growth rate[81–85]. Zhao *et al*. [81] studied the effects of overload, underload, high-low sequence loading and stress-ratio (R) on fatigue crack growth of 7075-T651 aluminum alloy by using a compact-tension specimen. It was found that for the same *R*-ratio, the influence of specimen geometry on the relationship between crack growth rate and stress intensity factor was insignificant. However, the application of overload showed significant retardation of the crack growth rate; whereas, the application of a single underload caused a slight acceleration in the crack growth rate. The crack resumed its normal growth rate once it

propagated out of the influencing plastic zone created by the overload or underload. Dahlin *et al*.[82] studied the effect of mode II overload on subsequent mode I crack growth on a compact-tension-shear (*CTS*) specimen made of steel AISI 01 and found that the mode I crack growth rate decreased after a single mode II overload. This effect continued even after the crack propagated out of overload plastic zone created by mode II. Also, it was claimed that the crack closure due to tangential displacement of crack-surface irregularities was the reason behind this behavior. Tur *et al*.[83] investigated M(T) specimen of 2024-T3 aluminum alloy to study the crack growth behavior due to periodic tensile overloads and found that the crack retardation was affected by the periodicity of the overloads. Borrego *et al*. [84] used M(T) specimen of 6082-T6 aluminum alloy to study the effect of single tensile overload on crack growth rate and found that the extent of crack retardation increases with overload ratio but decreases with stress ratio (*R*). At each overload, crack growth showed a brief initial acceleration followed by subsequent decrease in crack growth rate until its minimum value was reached, after which the crack growth rate showed a gradual increase till it acquired its normal growth rate. This study also claimed that the plasticity-induced crack closure is the main governing mechanism behind the crack retardation behavior but did not explain the reason for the brief initial acceleration. In contrast, Sadananda *et al*.[85] examined overload effects on fatigue crack growth and concluded that the residual stresses ahead of the crack tip created by the overload plastic zone are the main reason causing crack retardation, rather than the plasticity induced crack closure appearing behind the crack tip.

All the above investigations involving overload excursions were conducted on metallic materials subjected to uniaxial load conditions and not much attention was given to biaxial/multiaxial load conditions. Perhaps, the sophisticated nature of the test set-up and the high expense associated with the multiaxial fatigue experiments have limited the investigations made by the researchers in the case of multiaxial loadings. Few researchers [33,86–88] have adopted a simplistic approach to implementing multiaxial load condition by changing the orientation of the crack or/and using a complex fixture on a uniaxial test frame rather than actually applying the multiaxial loads [33,86–88]. Such arrangements don't account for the real loading conditions in the practical applications. A handful of researchers [26,89–91] have also used different variants of the cruciform specimens to investigate the biaxial load conditions, but their focus was limited only to understand the multiaxial fatigue behavior under the constant amplitude loading. Lee *et al*. [89] investigated the effect of biaxiality ratio on fatigue life and crack orientation by subjecting the specimens of aluminum alloys 1100-H14 and 7075-T651 to in-phase and out-of-phase loading. Mall *et al*. [90] characterized the crack growth behavior of aluminum alloy 7075-T6 under in-plane biaxial tension– tension fatigue with phase differences of 90° or 180°. Misak *et al*. [91] investigated the crack growth behavior of aluminum alloy 7075-T6 under in-plane biaxial tension–tension fatigue for different biaxiality ratios. Neerukatti *et al*. [26] studied fatigue damage characteristics of Al 7075-T651 under in-phase and out-of-phase loading conditions and examined the effect of different biaxiality ratios. With the exception of Datta *et al*. [20] and Singh *et al*. [24], there is no experimental data available in the literature for biaxial loading with load excursion or variable amplitude loading. Datta *et al*.

[20] in their research investigated crack propagation behavior and the governing crack growth micromechanisms in aluminum alloy 7075 under in-plane biaxial fatigue loading with single tensile overloads of different magnitudes and at different fatigue crack lengths. It was found that crack retardation at lower overload ratios was governed by plasticity-induced crack closure in the form of crack-tip blunting. Whereas, at higher overload ratios, it was a result of the combined influence of crack-tip deflection, plasticity-induced crack closure, and crack-tip splitting. The recovery distance, which is the distance traveled by the crack-tip after an overload until the crack retardation effects wear off, was found to be directly proportional to overload magnitude as well as the crack length at overload. Singh *et al*. [24] have demonstrated that the fatigue life of the specimen is increased with increase in the magnitude of shear overloads in an otherwise constant amplitude biaxial loading. It was found that the crack growth rate in the transient region showed an initial acceleration that was followed by immediate retardation. When the magnitude of shear overload ratio was increased, the value of initial acceleration further increased in addition to the increase in the crack retardation value that followed the initial acceleration, i.e. crack growth rate is decreased. Though this study talked about the effect of shear overload in biaxial loading, very few overload cases were considered which is not enough to give an accurate and complete analysis of the fatigue damage behavior. Moreover, this investigation does not contain any information on the mechanisms governing the crack behavior in the transient region created by the overload. Furthermore, there is very limited information available on the micromechanism, and it is insufficient to correlate the microscale fracture features with the macroscale fatigue crack behavior.

The available experimental data and the crack propagation behavior under biaxial load with cruciform specimens are not only limited but also contradictory to some extent when compared with the uniaxial or biaxial conditions. Furthermore, the governing micromechanisms are not yet fully understood and there exist significant disagreements in determining the precise mechanism while incorporating the effects of overloads. So far, attention has been limited to tensile overloads; to the best of the authors' knowledge, the effects of shear or mix-mode overloads under biaxial loading has not been fully investigated. This chapter presents an experimental investigation to gain a comprehensive insight into the nature of crack propagation under the influence of shear (pure mode II) overloads in an otherwise constant amplitude biaxial fatigue loading. The primary goal is to characterize the in-plane biaxial fatigue crack propagation behavior of AA-7075 aerospace grade alloy in the transient region and to investigate the underlying microscale mechanisms at different magnitudes of shear overloads and at different fatigue crack lengths.

3.2. Material and Methods

3.2.1. Material

The material used to study the overload effects in biaxial fatigue loading was procured in the form of aluminum alloy 7075-T6 sheets, which is often used in aircraft structural components, automotive industry, and other high-strength applications due to its high strength, low density, good fatigue strength, stiffness and corrosion resistance [53]. Material properties provided by the manufacturer include a yield strength of 503 MPa, an ultimate tensile strength of 572 MPa, modulus of elasticity of 71.7 GPa, and Brinell

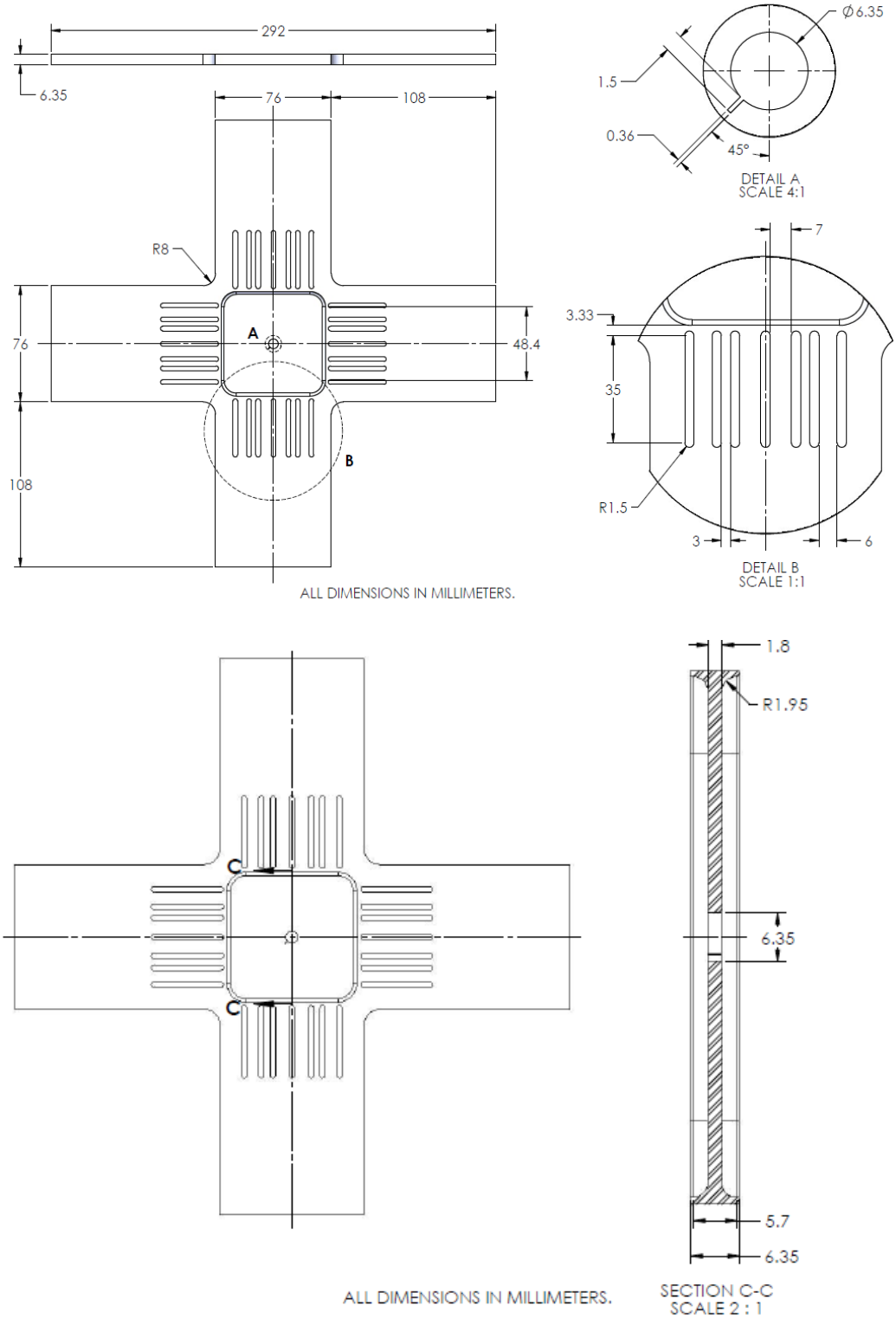

Figure 3.1: Design of the cruciform specimen used in biaxial fatigue experiments.

hardness value of 150. The chemical compositions of the material are in accordance with the ASTM standard B211.

3.2.2. Specimen Design

Specimen geometry and dimensions are the important parameters that affect fatigue damage behavior at the given loading condition [19]. But as of now, there is no standard geometry available for the study of biaxial load conditions; therefore, specimen design becomes imperative in determining accurate fatigue life and crack growth behavior under such biaxial load condition. Richard [54] has presented nine different specimens, but in experiments involving in-plane biaxial load condition, generally, a cruciform type specimen is employed for characterizing crack growth behavior. Such a specimen facilitates the means for accurate application of various kinds of cyclic biaxial loads, including overloads, underloads, in-phase and out-of-phase loadings. As shown in Figure 3.1, the specimen was designed to ensure a uniform stress distribution in the central web area for initial yielding. These specimens were machined from a 6.35 mm thick rolled plate of AA 7075-T651. The overall horizontal and vertical lengths of the cruciform arms are 292 mm each and they have a thickness of 1.8 mm in the central web region. This region contains a hole of diameter 6.35 mm, at which a notch of length 1.5 mm and width of 0.36 mm is made at an angle of 45° to accelerate crack initiation and ensure the favorable orientation for the crack propagation along the 45° plane with respect to the loading axes under pure mode I fatigue loading; thus preventing any arbitrary orientation that may have arisen from the periphery of the central hole in the absence of this notch. Similar notch designs at the center hole of cruciform specimens are used by various authors in the

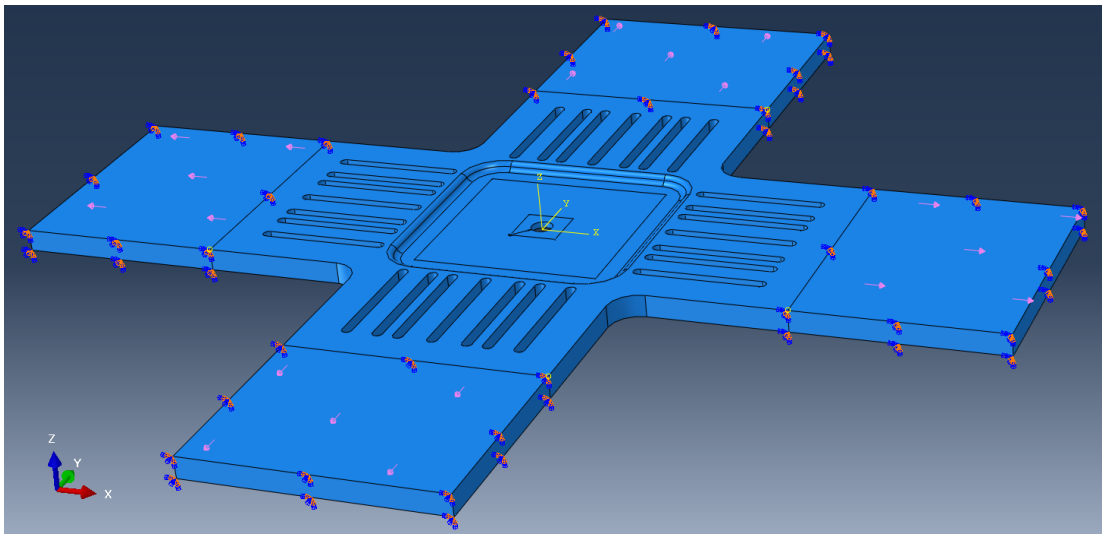

Figure 3.2: Finite element model (FEM) used to evaluate SIF under mode I and mode II loading.

literature [20,26,91] for their studies on the effect of in-phase loading, out-of-phase loading, tensile overloads, etc.

3.2.3. Finite Element Analysis

A numerical approach was adopted to determine the value of *SIF* in a cracked cruciform specimen in the presence of a biaxial tensile fatigue loading as shown in Figure 3.2. The geometry of the cruciform specimen was generated using a commercially available CAD (computer aided design) software, SOLIDWORKS. A different commercially available software, ABAQUS, was used for the FEM simulation in order to obtain the *SIF* range, stress variation in front of the crack tip etc. A quasi-static model was thereby implemented in ABAQUS/Standard where three-dimensional continuum elements were used (both hexahedra and quadrilateral). While hexahedra or brick element (C3d20R) was used in the gauge region and in some portions of the cruciform arm, quadrilateral element (C3D10I)

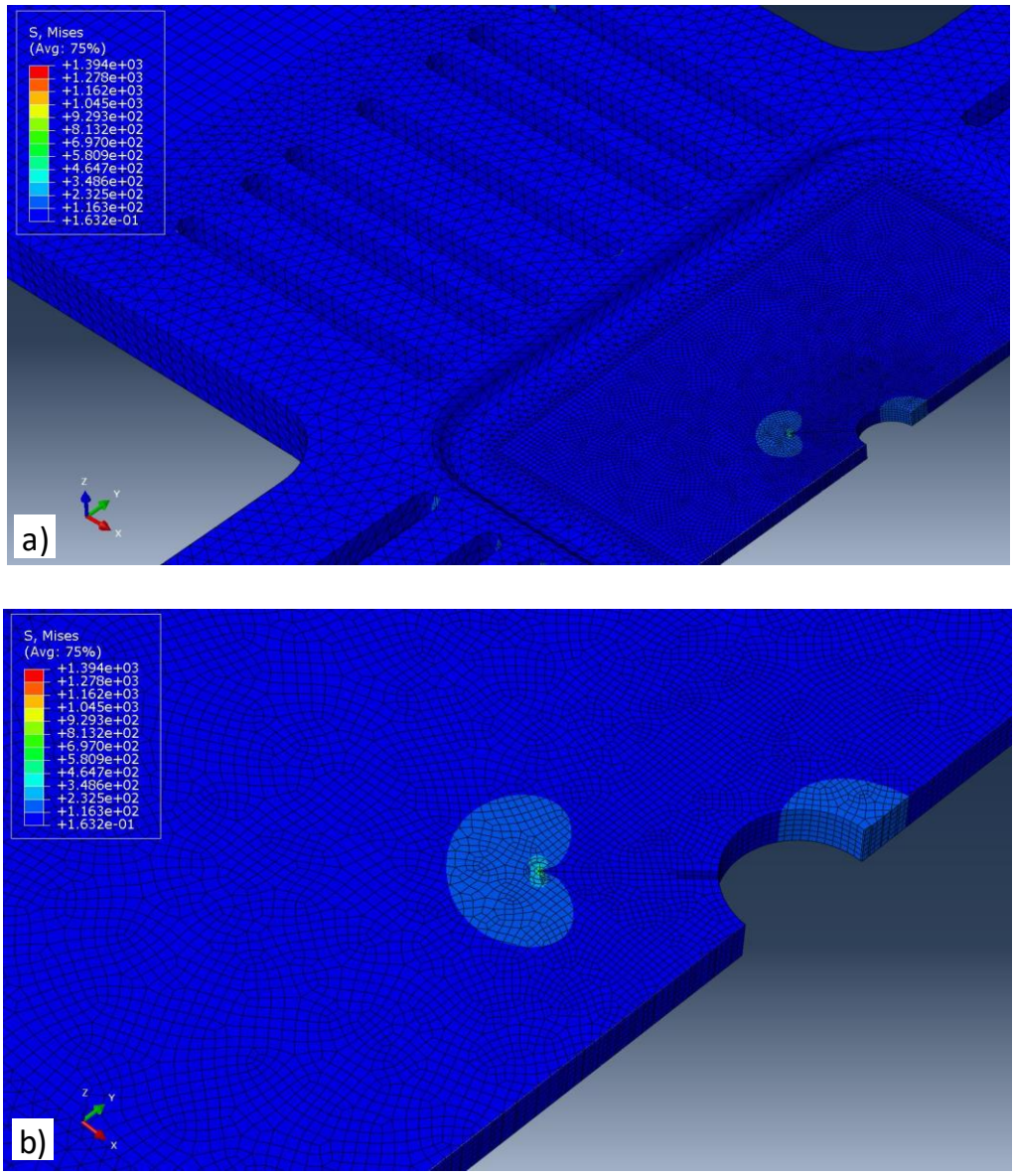

Figure 3.3: a) Detail of the mesh used in the FEM model and the stress distribution in the specimen during mode I loading; b) Magnified image showing the stress concentration around the crack tip.

was used in the remaining portion of the cruciform, as shown in Figure 3.3. Moreover, the global element-size was taken to be 1.75 mm while the element size in the gauge region was 0.6 mm. A more refined mesh was created in the vicinity of the crack region, where the element size was reduced to 0.3 mm, shown in Figure 3.3(b). The material and the

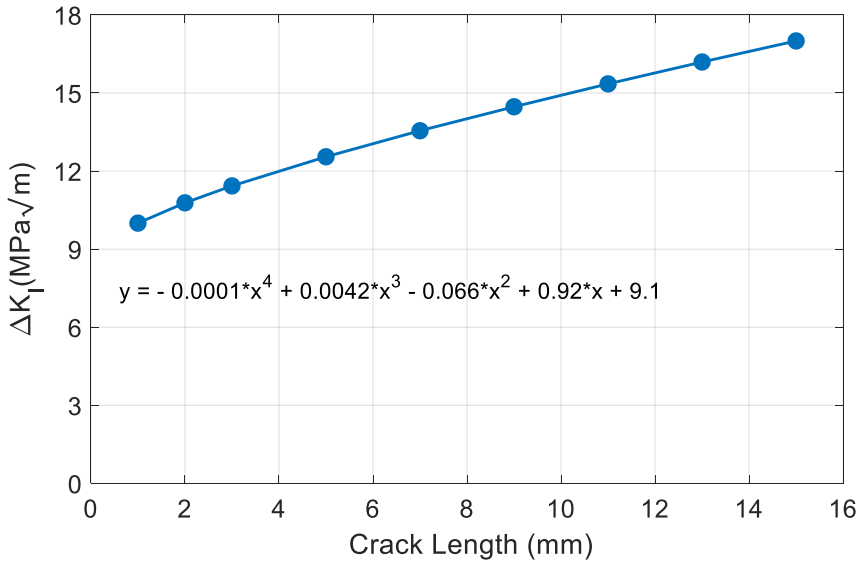

Figure 3.4: Regression curve obtained from the plot between ΔK_I values and the crack lengths to estimate the ΔK_I values at any given crack length.

geometric properties were specified in accordance with the test specimen. Loading conditions were assigned following experimental setup and were implemented through traction forces as shown in Figure 3.2. It was applied on the surfaces of all the four arms (front and back), which extend for a length of 50.8 mm from their respective free ends. The loaded regions of the horizontal and vertical arms were constrained to move only in horizontal and vertical directions respectively. Since the fatigue tests were conducted with a biaxiality ratio (λ) of 1, the fatigue crack in all the tests grew along the 45° notch, resulting in pure mode I crack growth, hence the value of K_{II} and K_{III} were not considered for crack-tip *SIF* calculations. Based on the actual direction of crack propagation obtained from experimental results, crack propagation for the simulation was assigned along the 45° notch. To ensure an accurate value of *SIF*, contour integral calculations were performed using 6 contours at each node surrounding the crack-tip. Multiple simulations were run to find out

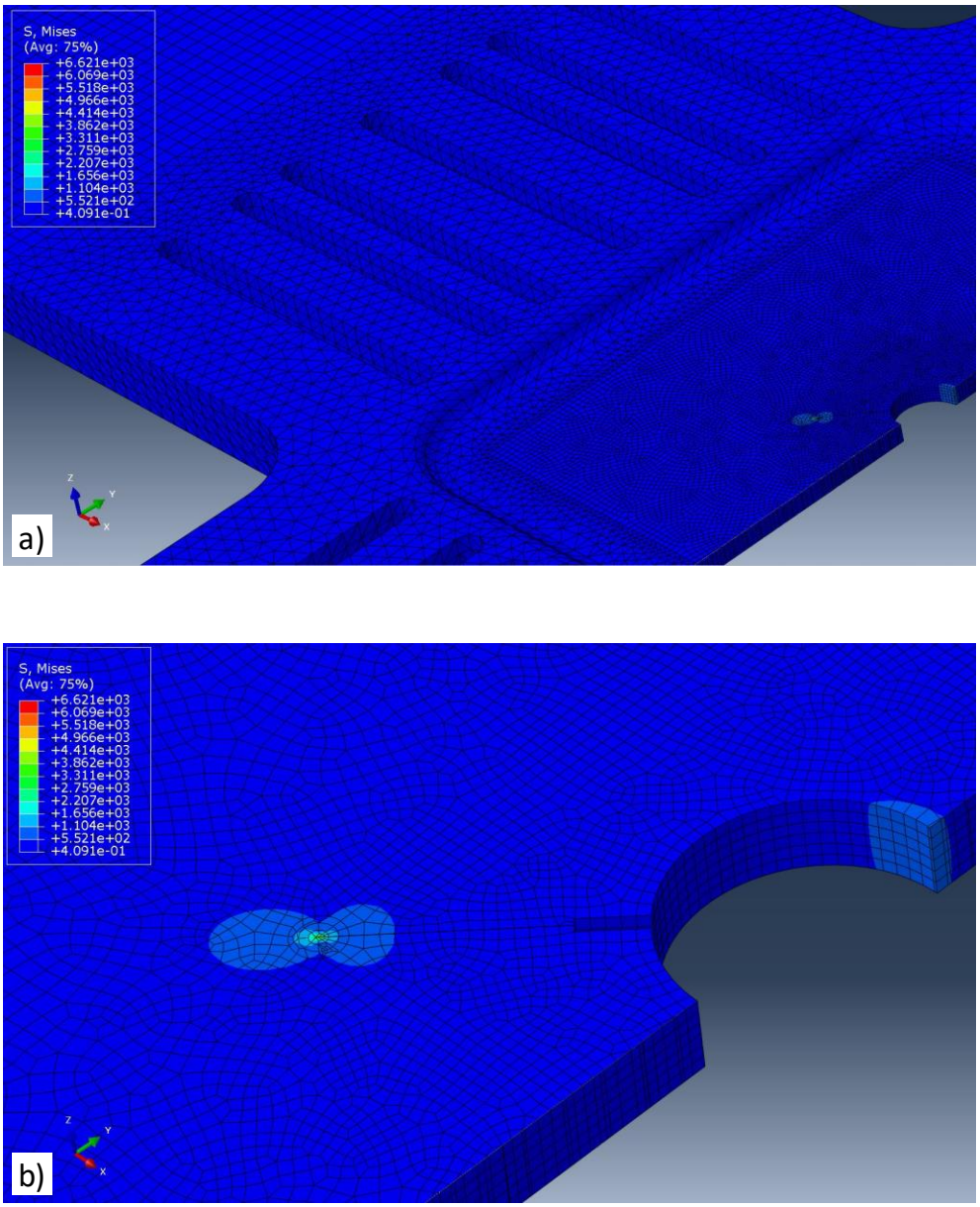

Figure 3.5: a) Details of the mesh used in the FEM model and the stress distribution in the specimen during mode II loading; b) Magnified image showing the stress concentration around the crack tip.

the converged values of K_I at different crack lengths (shown in Figure 3.4), which were later used to fit a regression curve in order to determine the K_I value at any given crack length.

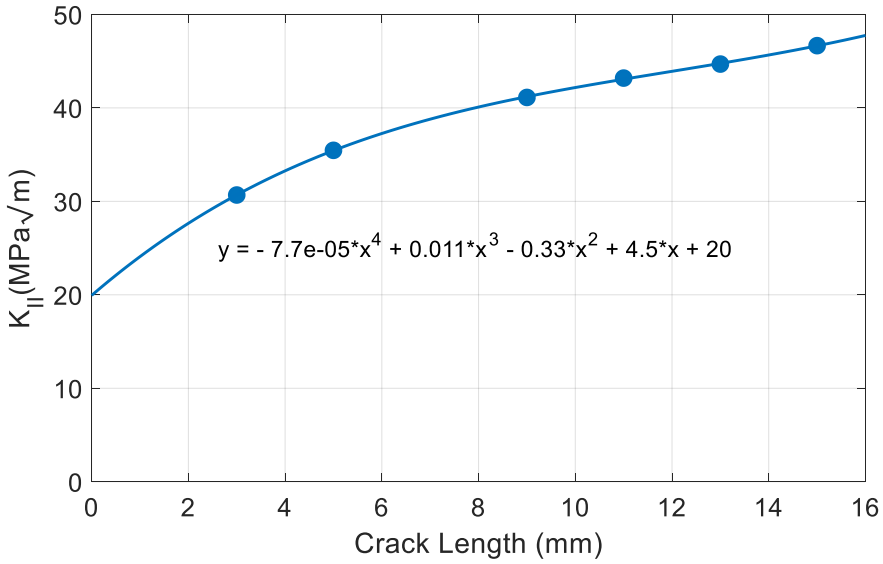

Figure 3.6: Regression curve obtained from the plot between K_{II} values and the crack lengths to estimate the K_{II} values at any given crack length.

The value of *SIF* (K_{II}) during the shear overload was found using a similar FEA model in which the direction of load in the Y-axis was reversed. Thus, the specimen was exposed to tensile loading in X-axis while a compressive loading of the same magnitude was applied in Y-axis to ensure pure shear (K_{II}) loading at the crack tip inclined to 45° angle, for which the stress distribution and the meshing are shown in Figure 3.5. Since the crack tip, in this case, was exposed to pure shear loading (mode II), the value of K_I and K_{III} were not considered for *SIF* calculations. The values of K_{II} obtained from multiple converged simulations conducted at different crack lengths were used to fit another regression curve, as shown in Figure 3.6, to find the values of K_{II} at any given crack length.

3.2.4. Experimental Procedure

All the experiments were conducted using the MTS planar biaxial/torsional load frame, which has a dynamic load capacity of 100 kN in both horizontal and vertical directions and

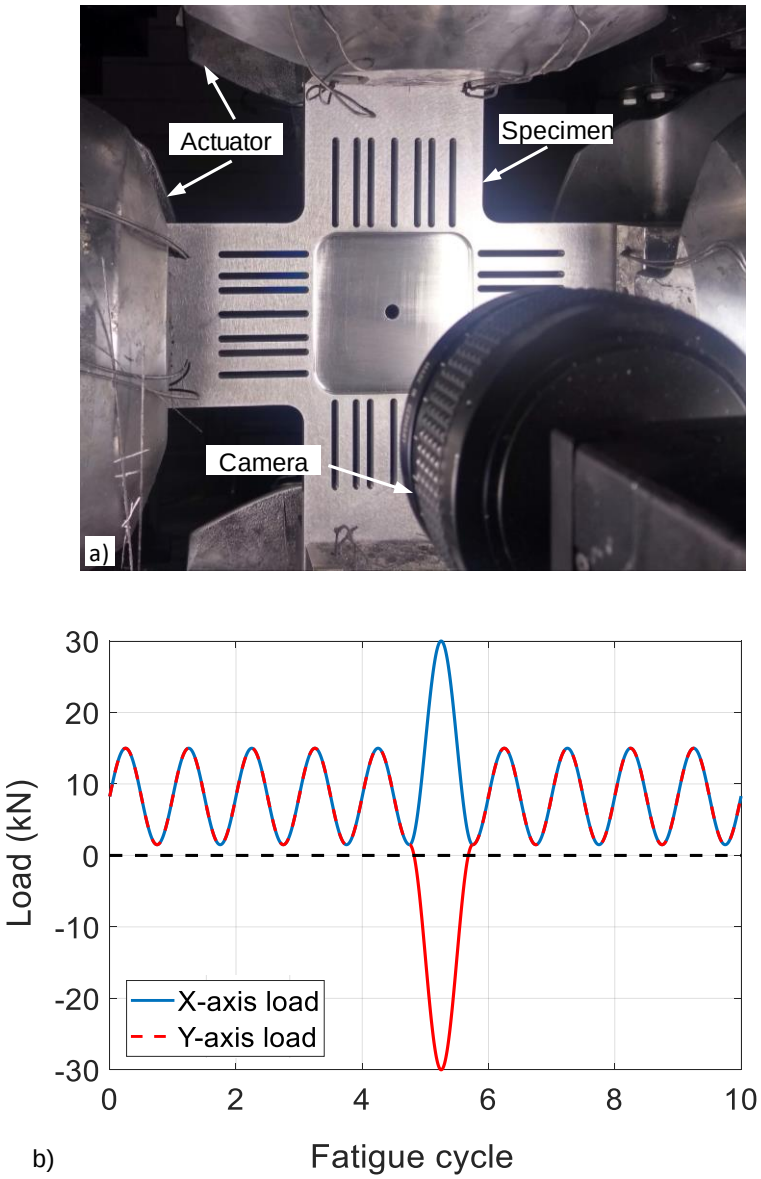

Figure 3.7: a) Experimental set-up; b) Load spectrum used in conducting fatigue tests under various overload conditions.

a torsional load capacity of 1100 Nm, shown in Figure 3.7(a). The testframe is equipped with six actuators, which can be independently controlled to conduct fatigue tests under a wide range of biaxial loading conditions, including in-phase, out-of-phase, spectrum loading, overloads, and underloads. To study the effects of a single overload on biaxial

fatigue crack propagation, fatigue load spectra were generated with single overload excursions in an otherwise constant amplitude (CA) loading with P_{max} (maximum cyclic load) = 15 kN, R (stress ratio) = 0.1 and a frequency of 10 Hz, as shown in Figure 3.7(b). Tests were conducted at five different values of shear overload ratio, i.e. (R_{OL-X}, R_{OL-Y}) = (1, -1), (1.5, -1.5), (1.75, -1.75), (2, -2), and (2.5, -2.5); where R_{OL-X} = Overload ratio in X-axis, R_{OL-Y} = Overload ratio in Y-axis; N_{OL} = Fatigue cycle at overload; P_{OL-X} = Overload in X-axis; ; P_{OL-Y} = Overload in Y-axis. For each value of overload, three specimens were tested in order to investigate the effect of overload magnitude on fatigue crack growth behavior at different crack lengths or fatigue cycles as detailed in Table 3.1. A high-resolution camera was positioned on the rear side of the specimen to capture the crack initiation and growth. The camera was programmed using LabVIEW to take images at user-defined time intervals and image processing software ImageJ was used to measure the fatigue crack lengths at different fatigue cycles. This allowed calculation of the cycles for crack initiation, propagation and final failure, and the crack growth rate at each crack increment.

Following the fatigue tests, quantitative fractography was performed on the fatigued specimens using SEM. The microstructural crack growth features obtained were correlated to the load history, crack growth rate and crack-tip plasticity. Fracture features corresponding to overloads of different magnitudes were identified and their influence on crack growth rate was investigated. Specifically, the transient region, which is the overload affected region where crack acceleration as well as retardation, was observed, was scanned for fracture modes known to govern crack propagation. Fracture surfaces were cut out from

Table 3.1:

Loading conditions for tests under shear overloads.

OL Type	Test ID	*R*-Ratio	P_{max} (kN)	$P_{OL\text{-}X}$ (kN)	$P_{OL\text{-}Y}$ (kN)	$R_{OL\text{-}X}$	$R_{OL\text{-}Y}$	N_{OL} (cycles)
Case-1	OL1_T4	0.1	15	15	-15	1	-1	30,000
	OL1_T4	0.1	15	15	-15	1	-1	60,000
	OL1_T5	0.1	15	15	-15	1	-1	30,000
	OL1_T5	0.1	15	15	-15	1	-1	60,000
	OL1_T6	0.1	15	15	-15	1	-1	30,000
	OL1_T6	0.1	15	15	-15	1	-1	60,000
Case-2	OL4_T1	0.1	15	22.5	-22.5	1.5	-1.5	30,000
	OL4_T1	0.1	15	22.5	-22.5	1.5	-1.5	60,000
	OL4_T2	0.1	15	22.5	-22.5	1.5	-1.5	30,000
	OL4_T2	0.1	15	22.5	-22.5	1.5	-1.5	60,000
	OL4_T3	0.1	15	22.5	-22.5	1.5	-1.5	30,000
	OL4_T3	0.1	15	22.5	-22.5	1.5	-1.5	60,000
Case-3	OL5_T1	0.1	15	26.25	-26.25	1.75	-1.75	30,000
	OL5_T1	0.1	15	26.25	-26.25	1.75	-1.75	60,000
	OL5_T2	0.1	15	26.25	-26.25	1.75	-1.75	30,000
	OL5_T2	0.1	15	26.25	-26.25	1.75	-1.75	60,000

OL Type	Test ID	*R*-Ratio	P_{max} (kN)	$P_{OL\text{-}X}$ (kN)	$P_{OL\text{-}Y}$ (kN)	$R_{OL\text{-}X}$	$R_{OL\text{-}Y}$	N_{OL} (cycles)
	OL5_T3	0.1	15	26.25	-26.25	1.75	-1.75	30,000
	OL5_T3	0.1	15	26.25	-26.25	1.75	-1.75	60,000
Case-4	OL2_T1	0.1	15	30	-30	2	-2	30,000
	OL2_T1	0.1	15	30	-30	2	-2	60,000
	OL2_T2	0.1	15	30	-30	2	-2	30,000
	OL2_T2	0.1	15	30	-30	2	-2	60,000
	OL2_T3	0.1	15	30	-30	2	-2	30,000
	OL2_T3	0.1	15	30	-30	2	-2	60,000
Case-5	OL3_T1	0.1	15	37.5	-37.5	2.5	-2.5	30,000
	OL3_T1	0.1	15	37.5	-37.5	2.5	-2.5	60,000
	OL3_T2	0.1	15	37.5	-37.5	2.5	-2.5	30,000
	OL3_T2	0.1	15	37.5	-37.5	2.5	-2.5	60,000
	OL3_T3	0.1	15	37.5	-37.5	2.5	-2.5	30,000
	OL3_T3	0.1	15	37.5	-37.5	2.5	-2.5	60,000

the fatigued cruciform specimens using a low-speed diamond saw and then sonicated in acetone to remove debris and the cutting fluid. Cleaned fracture surfaces were dried using compressed air and then mounted onto metallic stubs for SEM analysis.

3.3. Results and Discussion

Specimens failed under fatigue load having load excursions (shear overloads) are shown in Figure 3.8, in which Figure 3.8(a) - (e) correspond to the results obtained with R_{OL} of (1, -1), (1.5, -1.5), (1.75, -1.75), (2, -2), and (2.5, -2.5) respectively. For all the load cases, the macroscopic crack continued to propagate along the direction of initial notch, i.e. at 45°, and the crack trajectory remained unaffected by the presence of shear overload applied in the form of spike load at different crack lengths. Since the applied load was biaxial with the biaxiality ratio (λ) equal to 1, the propagation of crack at 45° during the constant amplitude cycles implies pure mode I loading at crack-tip, which is anticipated and observed by other authors in their uniaxial or biaxial tests [89,91]. However, the tendency of the crack to continue its original trajectory post overload and in the transient region is different from the general understanding presented in the literature that advocates the deviation of the crack tip or branching in an event of shear or mix-mode loading [33,87].

3.3.1. Fatigue Life

Throughout the tests, pictures were taken at predefined regular intervals to capture crack lengths corresponding to various fatigue cycles, which were then used by image processing software ImageJ to measure the fatigue crack lengths is shown in Figure 3.9. Figure 3.9 shows the effect of shear overloads on the macroscopic fatigue crack when the overloads were applied after 30, 000 (1^{st} overload) and 60,000 fatigue cycles (2^{nd} overload) at five

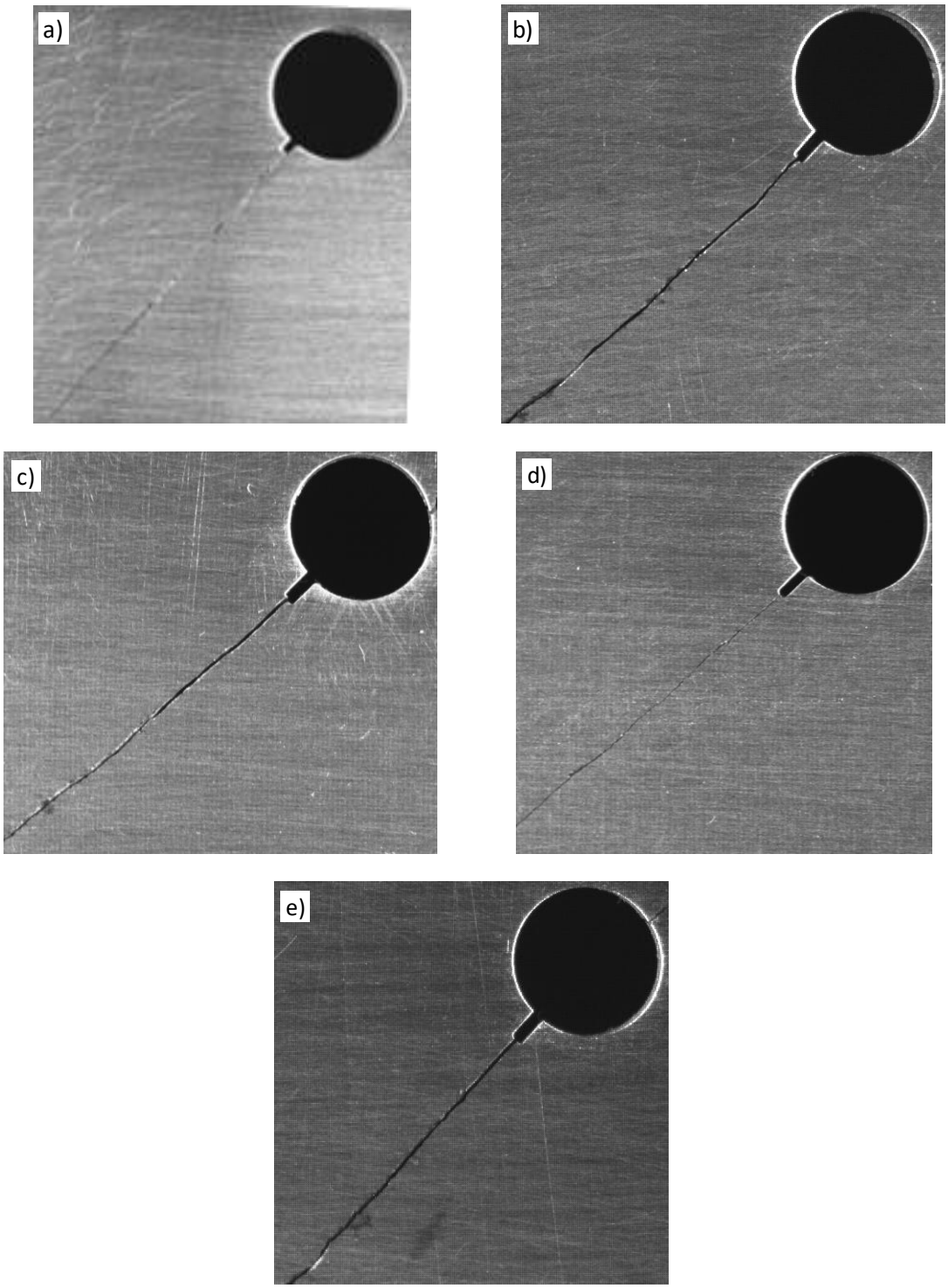

Figure 3.8: Orientation and trajectory of fatigue crack under shear overloads with overload ratio of: a) R_{OL} = (1, -1); b) R_{OL} = (1.5, -1.5); c) R_{OL} = (1.75, -1.75); d) R_{OL} = (2, -2); e) R_{OL} = (2.5, -2.5).

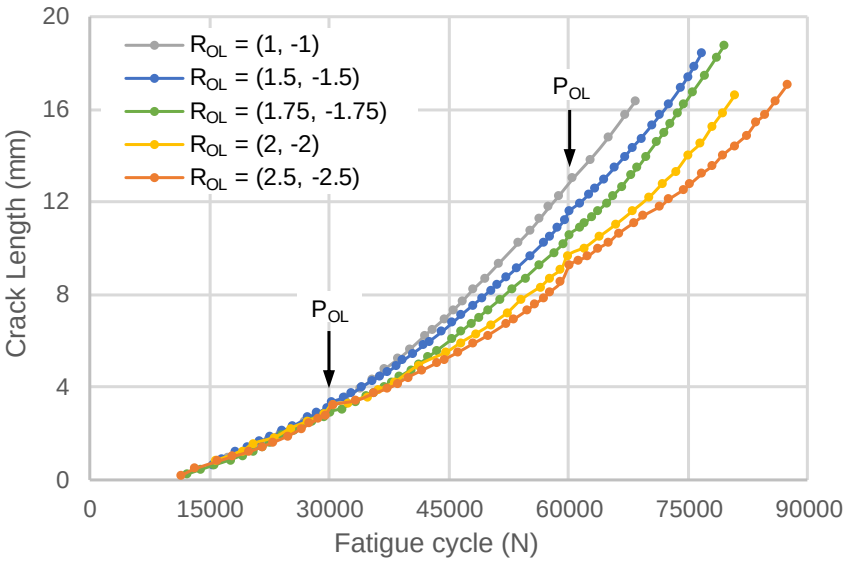

Figure 3.9: Plot of crack length against fatigue cycle for five different values of shear overload applied at the end of 30,000 cycles and 60,000 cycles.

different magnitudes of the overload ratios, i.e. (1, -1), (1.5, -1.5), (1.75, -1.75), (2, -2) and (2.5, -2.5). In all the cases, fatigue crack propagated the same length and followed the same trajectory until the application of the 1st overload, as shown in Figure 3.9. This behavior is anticipated because the loading condition up to this point was the same for all the five cases. However, after the application of first overload, the original trajectory of the crack length – fatigue cycle curve under different overload ratios deviated in different ways from their initial path, indicating that the fatigue life, measured by design tolerance approach for the same crack length, increases with the increase in the magnitude of shear overload. The maximum and the minimum increase in fatigue life can be observed for the overload ratios of (2.5, -2.5) and (1, -1) respectively. Second shear overload applied at the end of 60,000 cycles, further increased the fatigue lives of the specimens for all the overload ratios and repeated the behavior observed for the 1st overload. A greater impact on fatigue life was

observed when the 2nd shear overload was applied as compared to the 1st shear overload, which is more clear from the comparison of the overload ratios of (2, 2) and (2.5, -2.5) at 1st and 2nd shear overloads. At these two overload ratios, there is a little difference between their fatigue lives until the application of 2nd shear overload. But after 2nd shear overload a significant difference can be observed between their fatigue lives. Similar observations of increase in fatigue life were reported by other authors when the tests were conducted for tensile overloads either in a biaxial loading or in a uniaxial loading condition [20,24,81,82]; however, the crack growth rate and the crack governing micromechanism showed a different behavior for the shear overloads (presented in the next section) when compared with the results of tensile overloads presented by the other authors.

3.3.2. Crack Propagation

The experimentally observed fatigue crack growth rate, *da/dN*, is presented against the *SIF* range in pure mode I for five different cases of single shear overload excursions of different overload ratios in Figure 3.10. As shown in Figure 3.10, no observable change was noticed in the fatigue crack growth rate at the minimum value of shear overload ratio ((1, -1)); therefore, this case was used as a baseline reference to describe and compare the effects of the other four overload ratios on the fatigue crack growth rate. For every value of shear overload ratio, except for overload ratio of (1, -1), the crack growth rate showed a distinct behavior in the transient region. At first, the crack growth rate showed an instant and drastic acceleration which was followed by immediate and significant retardation. The acceleration was a short-lived and abrupt phenomenon; whereas, the retardation lasted for a much longer duration introducing a new parameter, referred to as ‘recovery distance’, to

Table 3.2:

Crack growth behavior under shear overloads.

OL Type	a_{OL} (mm)	ΔK_I (MPa.m$^{1/2}$)	K_{II_OL} (MPa.m$^{1/2}$)	R_d (mm)	*da/dN* (mm/cycle)			N_{OL} (cycles)
					Pre-OL (x 10^{-4})	OL (x 10^{-4})	Post-OL (x 10^{-4})	
Case - 1	2.54	11.33	15.11	-	1.95	2.22	1.76	30,000
	11.79	16.08	22.01	-	4.0	4.26	3.77	60,000
Case - 2	2.51	11.24	22.39	0.494	1.30	2.96	0.947	30,000
	9.81	15.08	31.77	1.293	3.28	5.27	2.35	60,000
Case - 3	2.73	11.38	26.64	0.863	1.57	3.62	1.06	30,000
	10.20	15.20	37.28	1.878	3.24	6.29	1.58	60,000
Case - 4	2.13	11.10	29.21	1.044	1.73	4.06	0.378	30,000
	8.37	14.38	40.93	2.058	2.42	6.71	1.73	60,000
Case - 5	2.63	11.3	37.63	3.086	1.84	4.20	0.715	30,000
	8.13	14.3	50.87	4.333	3.07	5.99	1.92	60,000

characterize the transient region. It is interesting to note that the magnitude of increase in the crack growth rate during acceleration was higher than the maximum decrease in the crack growth rate during retardation when compared with the constant amplitude crack growth rate before the application of shear overload. Once the crack growth rate reached the minimum value, it started to recover rapidly and then gradually approached the stable

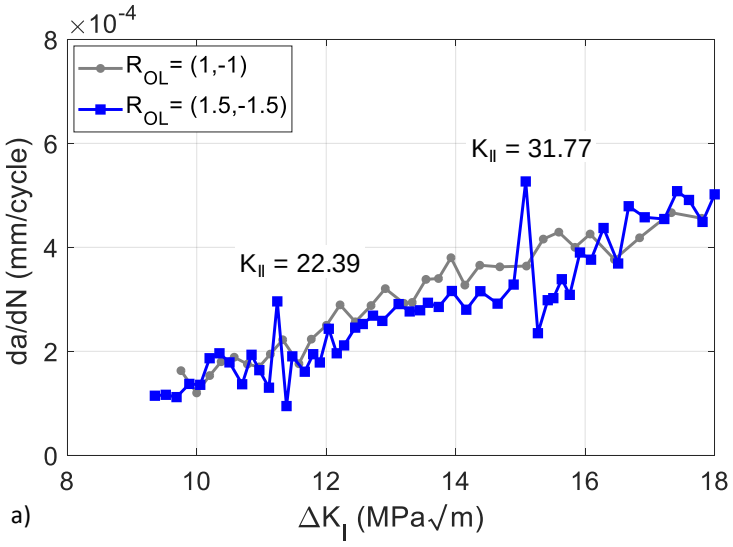
×10^-4
R_OL = (1,-1)
R_OL = (1.5,-1.5)
K_II = 31.77
K_II = 22.39
da/dN (mm/cycle)
ΔK_I (MPa√m)

a)

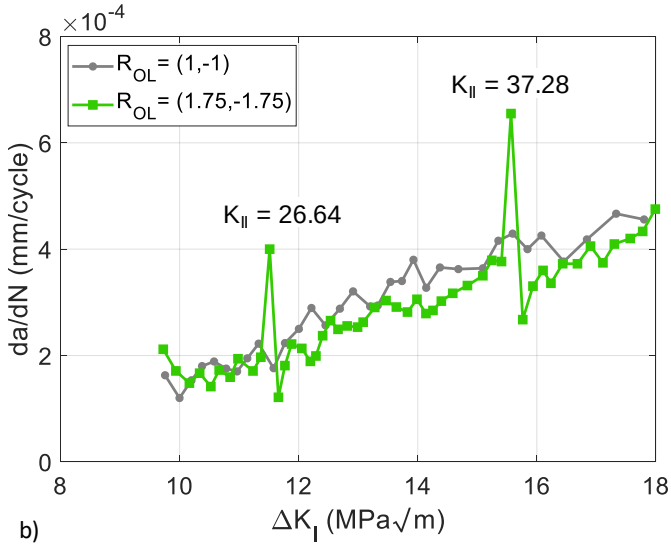
×10^-4
R_OL = (1,-1)
R_OL = (1.75,-1.75)
K_II = 37.28
K_II = 26.64
da/dN (mm/cycle)
ΔK_I (MPa√m)

b)

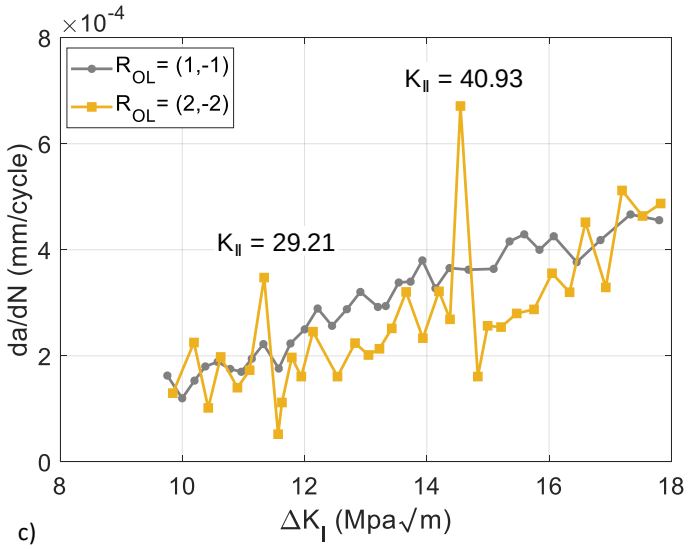
×10^-4
R_OL = (1,-1)
R_OL = (2,-2)
K_II = 40.93
K_II = 29.21
da/dN (mm/cycle)
ΔK_I (Mpa√m)

c)

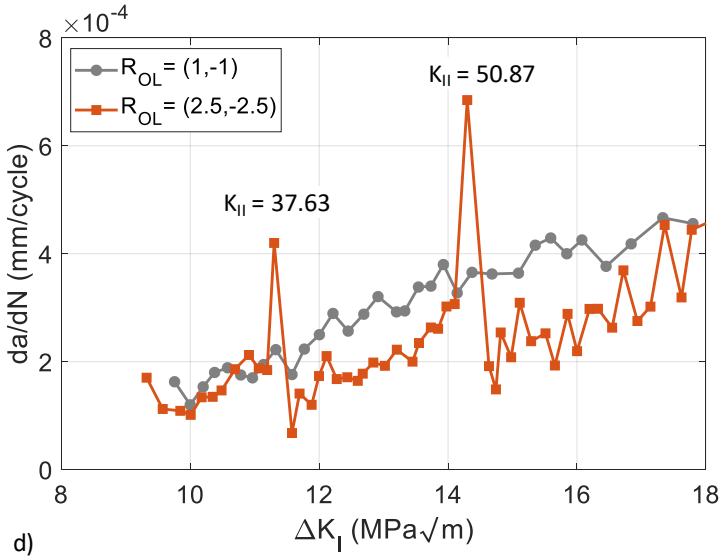

Figure 3.10: CGR is plotted against ΔK_I values in which mode II overloads were applied after 30,000 cycle and 60,000 cycle for: a) R_{OL} = (1.5, -1.5); b) R_{OL} = (1.75, -1.75); c) R_{OL} = (2, -2); d) R_{OL} = (2.5, -2.5).

crack growth rate; however, its value was not fully recovered when compared with the baseline reference curve (R_{OL} = 1, -1) and an offset in the data points, after the overload, can be clearly seen in each plot. With an increase in the magnitude of shear overload ratio or K_{II} (mode II *SIF*) at a given K_I (mode I *SIF*), the value of initial crack growth rate increased but the value of crack growth rate during retardation further decreased as shown in Figure 3.10(a) – (d). By comparing these changes, it can be seen that the magnitude of shear overload ratio (or K_{II}) has a greater impact on the initial acceleration than the retardation when the extreme values (maximum/minimum) of the crack growth rate are concerned. This observation was consistent even when the value of applied shear overloads was small with ΔK_I = 11 MPa√m (1st overload) or large with ΔK_I = 15 MPa√m (2nd overload). Similar crack growth behavior was also observed when the value of ΔK_I increased from 11 MPa√m to 15 MPa√m just before the application of the 2nd shear

overload, as shown in all the plots of Figure 3.10. The values of crack growth rates, crack length, and the *SIF* (ΔK_I and K_{II}) at the time of shear overloads are presented in Table 3.2 for all the five cases; where, a_{OL} = crack length at overload, K_{II_OL} = mode II *SIF* at overload, R_d = recovery distance, *OL* = overload, N_{OL} = fatigue cycle at overload. The effect of overload on crack growth rate in a uniaxial or a biaxial loading has been presented by many researchers in the literature; however, there are some disagreements in the results reported by them. While most of the researchers have not observed the initial acceleration [20,81,82], some authors observed this phenomenon [24,84,92] and hypothesized that the initial acceleration depends on material ductility, and is observed only at higher overload ratio [85].

3.3.3. Recovery Distance

Variable amplitude loading in the form of an overload or underload creates a transient zone ahead of the crack tip that can either accelerate or retard the crack growth rate. Recovery distance (R_d) is introduced to quantify the extent of the transient zone. It is defined as the distance traveled by the crack-tip after an overload until the crack retardation/acceleration effects wear off and the crack growth rates resume their normal values. Figure 3.11 shows the values of crack growth rate as crack acquired different lengths during the course of propagation while overload excursions were introduced in the form of shear overloads (mode II) in an otherwise constant amplitude tensile biaxial fatigue loading (mode I). Since there was not any observable change in crack growth rate for the overload ratio of (1, -1), R_d was calculated only for the overload ratios of (1.5, -1.5), (1.75, -1.75), (2, -2) and (2.5, -2.5). In order to determine the values of the R_d, first, linear

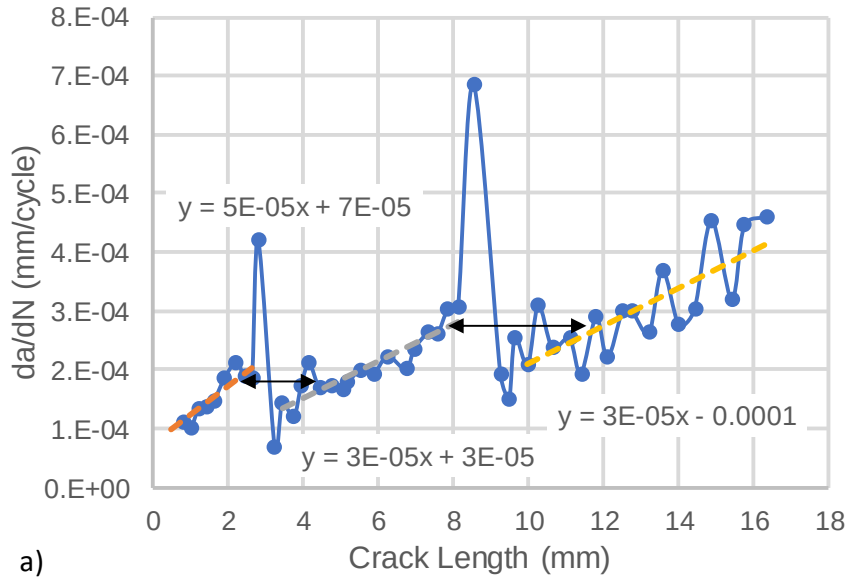

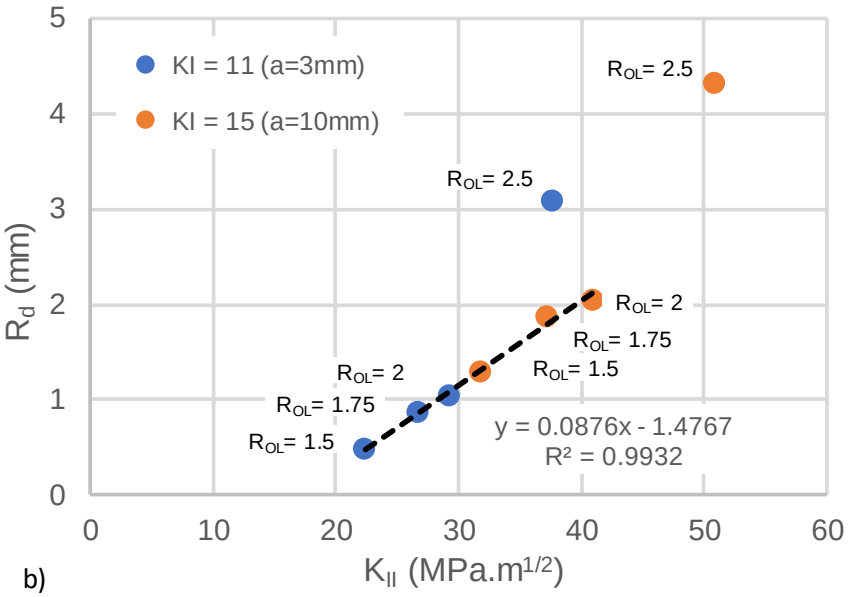

Figure 3.11: a) Crack growth rate is plotted against crack length to demonstrate the technique used to calculate recovery distance; b) Recovery distance is plotted against the overload K_{II} value that was applied when ΔK_I was 11 MPa$\sqrt{m}$ (after 30K cycle) or 15 MPa$\sqrt{m}$ (after 60K cycle).

regression curves were fitted between the crack growth rate and the crack length on the two sets of data separated by the overload position as shown in Figure 3.11(a), i.e. separate curve fitting for the data obtained before and after the application of overloads. Second, the crack growth rate just before the application of overload was obtained from the regression curve. Third, position of the crack on the post-overload regression curve that has the same crack growth rate just before the overload was identified. Fourth, the difference between the two crack lengths having the same crack growth rate was obtained as recovery distance and its values for different shear overload ratios are presented in Table 3.2. As shown in Figure 3.11(b), R_d corresponding to different values of shear overload ratios, applied after 30,000 cycles (ΔK_I = 11 MPa√m) and 60,000 cycles (ΔK_I = 15 MPa√m), was plotted against the overload stress intensity factor (K_{II}). The data points in blue were obtained when the value of ΔK_I was 11 MPa√m (a_o ~3mm) at the time of shear (mode II) overload and for the data in red, the value of ΔK_I was 15 MPa√m (a_o ~10 mm). Irrespective of the initial values of ΔK_I at the time of shear overload, a linear relationship between the R_d and K_{II} values was obtained, except for the shear overload ratio of (2.5, -2.5). Datta *et al*. [20] have presented the value of recovery distance for a similar biaxial fatigue experiment during a tensile (mode I) overloads. The values obtained by them were 2-4 times smaller than the recovery distance observed here under shear (mode II) overloads with the same overload ratio. The difference in the values is justified (explained in the next section) since the size of plastic zone ahead of the crack tip in mode II loading is up to five times bigger than that in mode I loading at the same amplitude of far-field loading [1].

3.3.4. Crack Growth Mechanism

Crack growth behavior under the influence of overloads is a complex phenomenon governed by multiple distinct and competitive mechanisms that depend on several factors including microstructure, magnitude of loading, stress ratio, environmental conditions, etc. [85,93]. Some of these mechanisms as reported in the literature include: crack tip blunting; crack deflection, branching and secondary cracking; strain hardening; residual compressive stresses; plasticity-induced closure etc., which may operate either ahead of the crack tip or in the wake region of the crack under the effect of mode I overload / underload in an otherwise constant amplitude loading. The crack growth behavior as explained by these mechanisms was based solely on the size of the overload plastic zone obtained from various models such as Irwin and Dugdale models, in which the estimated plastic zone size was the length of the plastic zone along the crack line; however, the largest size of the plastic zone in mode I overload is found not along the crack line but along a line approximately perpendicular to the crack line. Such approximation/models undermine the effect that arises due to the shape of the plastic zone created ahead of the crack tip during the overload and is not completely reliable to explain the characteristics of crack growth during the other overload types. Thus, it's important to correlate both the shape and the size of the plastic zone with the crack growth behavior (initial acceleration, crack growth retardation, recovery distance) as they are complimenting and competing in determining the mechanism governing the crack growth behavior.

It is a known fact that the fatigue crack during stage II propagation grows through the duplex slip mechanism in mode I and has been well documented in the literature [1].

However, an entirely different mechanism operates when a load excursion (overload) is applied. In contrast to the tensile overload (mode I), where initial acceleration is generally not observed, here in the case of a pure shear overload (mode II), not only the initial acceleration was observed but was also found to be proportional to the crack length and the magnitude of shear overload. As shown in Figure 3.12, on the application of shear overload, there is a sudden change in the stress state near the crack tip causing an increase in the magnitude of maximum shear stress and also a change in the orientation of the plane of maximum shear stress, which in turn activates multiple slip planes along the direction parallel to the crack line. While the increased stress accelerates the dislocation motion, the new orientation of slip planes provides lower resistance to the dislocation motion, thereby, increasing the existing acceleration. This accelerated motion of the dislocations on the slip plane is responsible for the initial acceleration in the crack growth rate. The initial acceleration was immediately followed by the retardation in the crack growth rate, which was also observed to be proportional to the crack length and the magnitude of shear overload. Considering all the mechanisms reported in the literature, crack retardation behavior under shear overload was found to be dominated by the combined effect of three concurrent mechanisms that interact with each other as the crack propagates. These mechanisms include residual compressive stress, plasticity induced crack closure and strain hardening. Immediately after a shear overload, the effect of residual compressive stress is maximum, and it is the main contributing mechanism responsible for the onset of the crack retardation; however, as crack propagates, the plasticity in the overload wake region increases rapidly leading to the crack closure, which gradually dominates over the

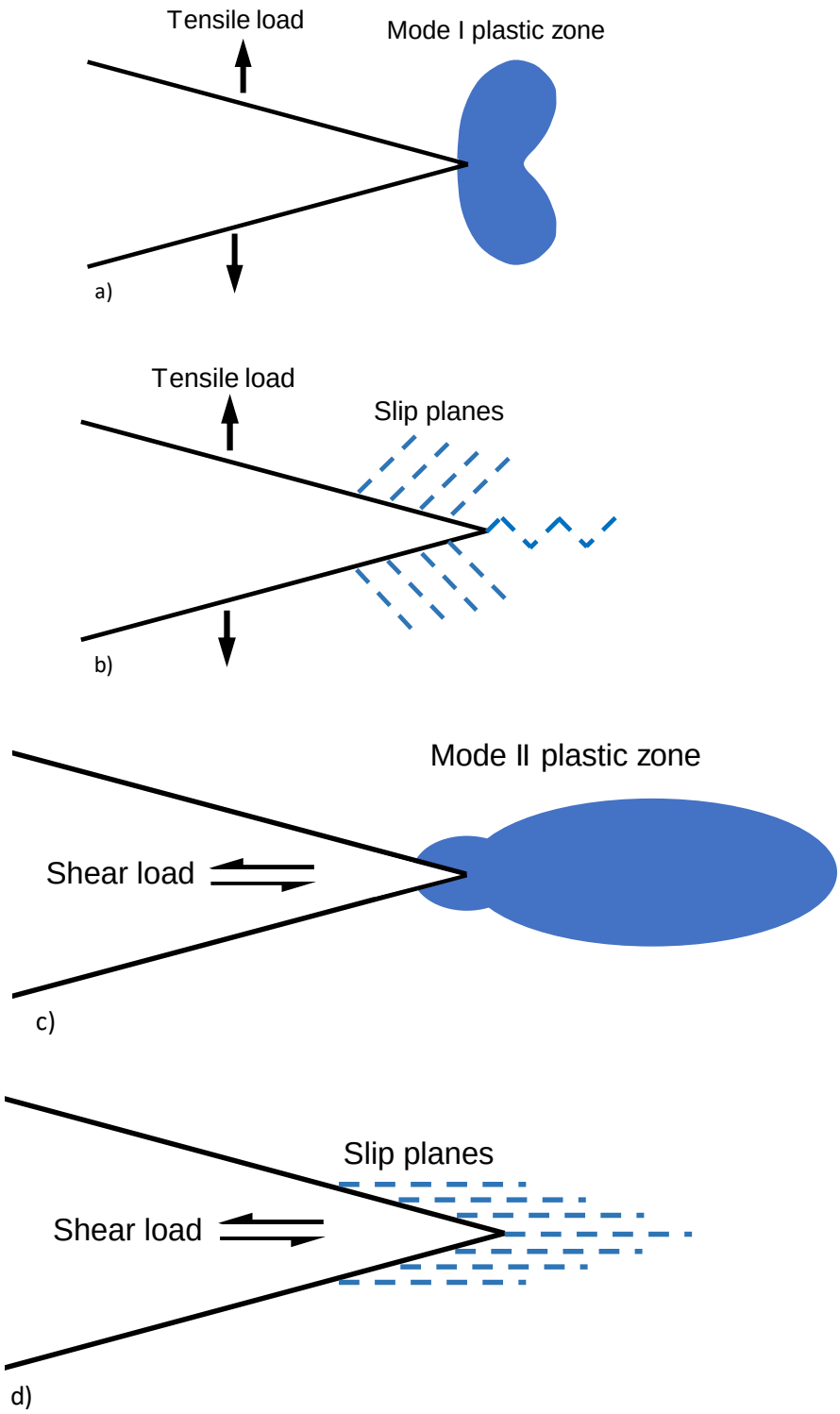

Figure 3.12: a) Plastic zone ahead of the crack tip and b) dislocations motion for mode I (tensile) loading. c) Plastic zone and d) dislocations motion for mode II (shear) loading.

compressive residual stress as a governing mechanism for crack retardation. On the other hand, the effect of strain hardening persists throughout the transient zone and is responsible for increasing the material's strength, thereby causing further retardation.

The stress state around the crack tip and the shape of the plastic zone under shear loading in the cruciform specimen is obtained from Shlyannikov *et al*. [94] as shown in Figure 3.12. Overloads cause a higher degree of plastic deformation which results in an increased size of the plastic zone near the crack tip. This extended-plastic zone induces reverse yielding ahead of the fatigue crack that gives rise to the compressive residual stresses. The presence of compressive residual stress ahead of the crack tip reduces the effective crack driving force that impedes crack propagation resulting in a sudden decrease in crack growth rate. Since, the residual stress depends on the size of plastic zone ahead of the crack tip, which in turn depends on the magnitude of stress intensity factor (overload ratio, crack length), an increase in *SIF* should essentially translate into the sudden drop in the value of crack growth rate (*da/dN*) and the same has been observed as shown in Figure 3.12. Moreover, when the drop in *da/dN* values of tensile overload having the same overload ratio and under the same experimental conditions, obtained by Datta *et al.* [20], was compared with the results of shear overloads in this chapter, it was found that the drop in *da/dN* values for tensile overload was 4-5 times more than what it was for shear overloads, which further supports that the initial retardation is dominated by compressive residual stress. Because of the orientation of the plastic zone, a bigger plastic zone size is created in the direction perpendicular to the crack line for mode I (tensile) overload than mode II overload (shear) as shown in Figure 3.12. As a result, a large compressive residual stress is obtained during

mode I overload leading to a bigger drop in *da/dN* values. Similar behavior in *da/dN* was also observed and reported by Hua *et al*. [95].

With the advancement of the crack into the transient region, the effect of compressive residual stress gradually decreases, but at the same time, the plasticity in the overload wake region increases rapidly causing the premature closure of the crack faces even under fully tensile far-field cyclic load, also known as plasticity induced crack closure. This leads to a continuous decrease in the effective crack driving force until the crack reaches a certain distance into the transient region, after which the effect of plastic wake starts to diminish and gradually fades away once the crack-tip moves some distance away from the overload plastic zone. The experimental evidence showing the delayed retardation, irrespective of the combination of K_{II} and ΔK_I values at the time of shear overload (Figure 3.10), strongly supports the presence of plasticity induced crack closure as one of the dominating mechanisms governing the crack propagation behavior. The phenomenon of delayed retardation is also observed by several other researchers [20,95] in their investigation, who have identified plasticity induced crack closure as the governing mechanism.

Strain hardening is another mechanism governing the crack propagation along with the residual compressive stress and plasticity induced crack closure. The additional dislocations generated during the plastic deformation results in the strain hardening that increases the strength of material by further resisting the dislocation motion. As a result, the driving force has to overcome an increased resistance, which leads to a decrease in crack growth rate. The recovery distance obtained from different experiments is found to be proportional to the magnitude of stress intensity factor corresponding to the overload

(Figure 3.11(b)), which in turn is proportional to the stretch of plastic zone ahead of the crack tip resulting in the strain hardening. When compared with the values of recovery distance obtained under pure tensile load by Data *et al*. [20], it was found that the recovery distance under pure shear overload is 2-4 times bigger. This behavior is anticipated, and it supports the strain hardening mechanism because the size of the plastic zone (along the crack line) under mode II loading is up to five times bigger than that in mode I loading for the same amplitude of far-field loading [1].

3.4. Governing Micromechanisms

An SEM was used to analyze the fracture features of the specimen, tested at three different values of biaxial overload ratio, i.e. (1, -1), (2, -2) and (2.5, -2.5), to correlate the fracture surface morphology with crack propagation behavior and to evaluate the effect of shear overload ratio on microscale mechanism. SEM analysis was mainly conducted in the proximity of the two shear overloads that were applied after the completion of 30,000 and 60,000 fatigue cycles in each case of overload ratio, and a comparative analysis of the fracture features in the pre-overload region, overload region, and the post-overload region (after transient zone) is presented.

3.4.1. R_{OL} = (2.5, -2.5)

Microscale fracture features for the first shear overload, applied at 30,000 cycles, are shown in Figure 3.13 and Figure 3.14. Figure 3.13(a) shows the fracture features of the specimen corresponding to the transient zone created in the immediate vicinity of the overload. Unlike tensile overload, where an overload line is formed on the tortuous surface, the transient zone under shear overload produced a “narrow-region” of smooth surface in

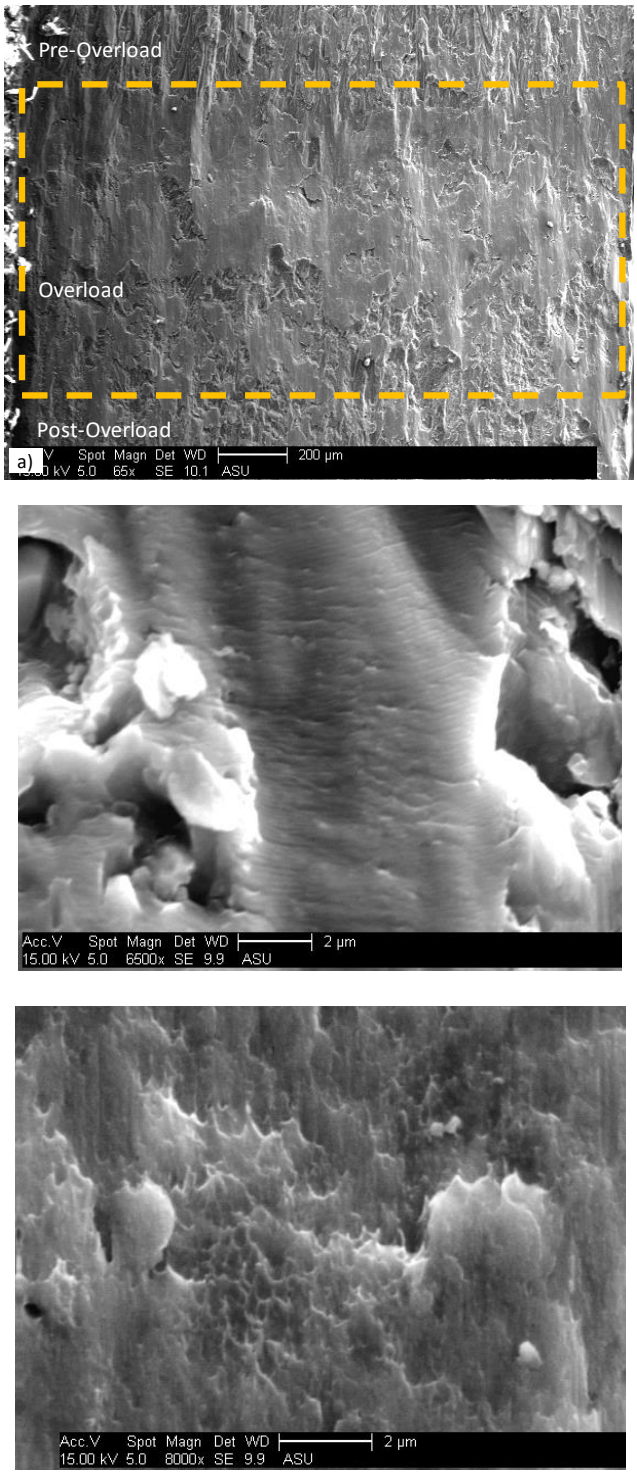

Figure 3.13: a) Microscale fracture features in the transient region of the specimen after the application of 1st shear overload (30k cycles) with R_{OL} = (2.5, -2.5). Magnified images of transient region showing: b) annihilated striations; c) elongated dimples.

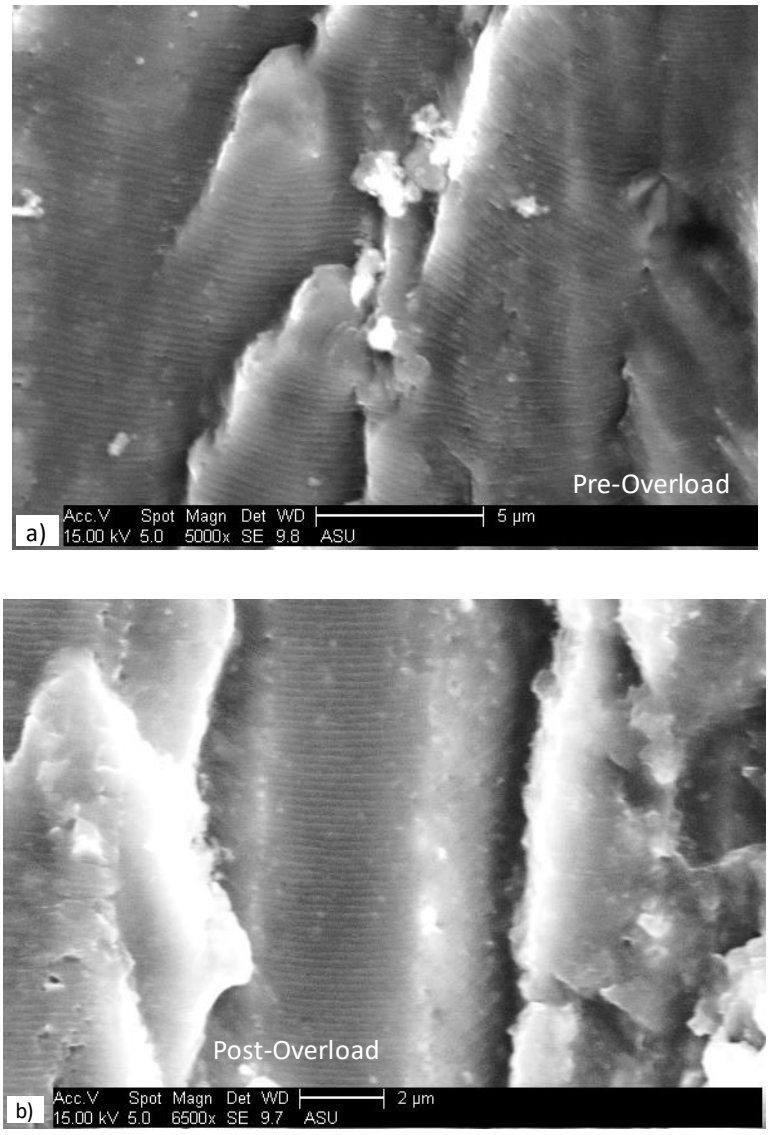

Figure 3.14: Well developed and fully-grown striations were observed in: a) pre-overload region; b) post-overload region for the1st shear overload with R_{OL} = (2.5, -2.5).

an otherwise tortuous region, as shown in Figure 3.13(a). Magnified images of the transient zone showed the presence of annihilated striations and elongated dimples as shown in Figure 3.13(b) and Figure 3.13(c) respectively. These two fracture-features co-existed in the transient zone and were observed in the entire region. Presence of annihilated striations in Figure 3.13(b) suggests a strong influence of mode II loading. This observation is further

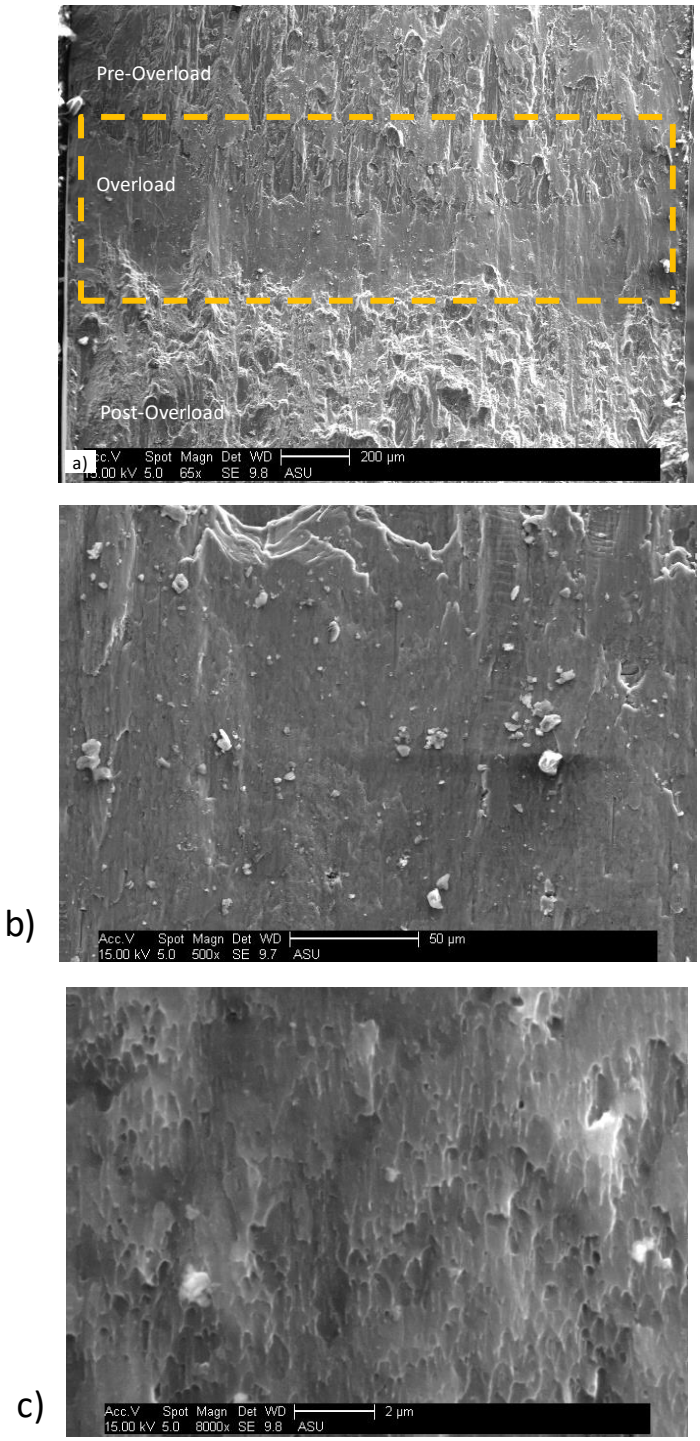

Figure 3.15: a) Microscale fracture features in the transient region of the specimen after the application of 2nd shear overload (60k cycles) with R_{OL} = (2.5, -2.5). Magnified images of transient region showing features of shear fracture: b) cleavage steps, tongue etc; c) elongated dimples.

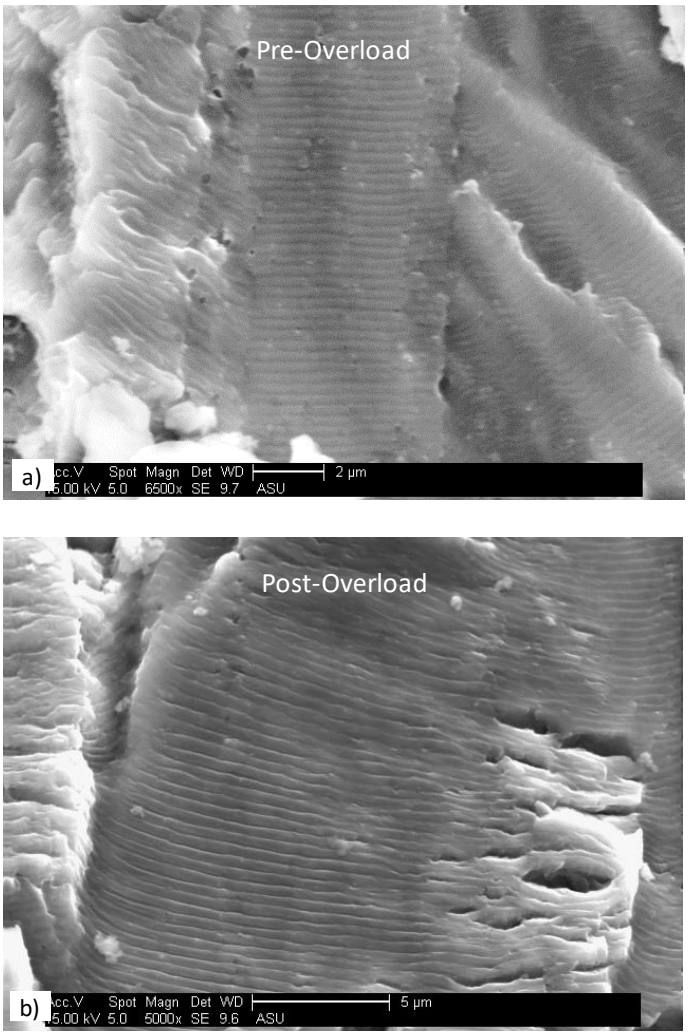

Figure 3.16: Well developed and fully-grown striations were observed in: a) pre-overload region; b) post-overload region for the 2nd shear overload with R_{OL} = (2.5, -2.5).

strengthened by the findings of Figure 3.13(c) that shows small-sized elongated dimples on the fracture surface, which are the result of high-magnitude mode II (shear) loading. Figure 3.14(a) shows the fracture feature of the specimen just before the application of shear overload, which consists of well-developed and fully-grown striations present on the adjacent ridges and propagating in the same direction. These features typically represent a stable stage-II mode I crack growth. The fracture surface of the specimen post overload

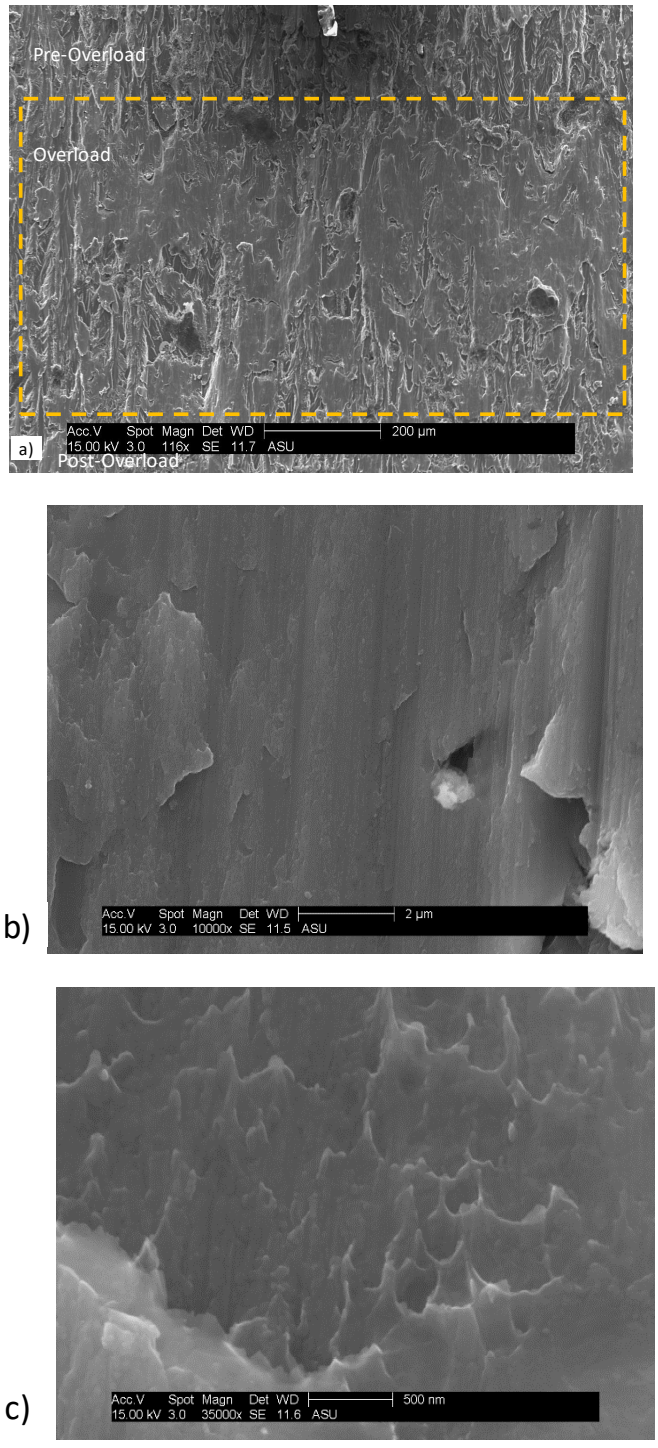

Figure 3.17: a) Microscale fracture features in the transient region of the specimen after the application of 1st shear overload (30k cycles) with R_{OL} = (2, -2). Magnified images of transient region showing features of shear fracture: b) tire tracks, tongue etc; c) elongated dimples.

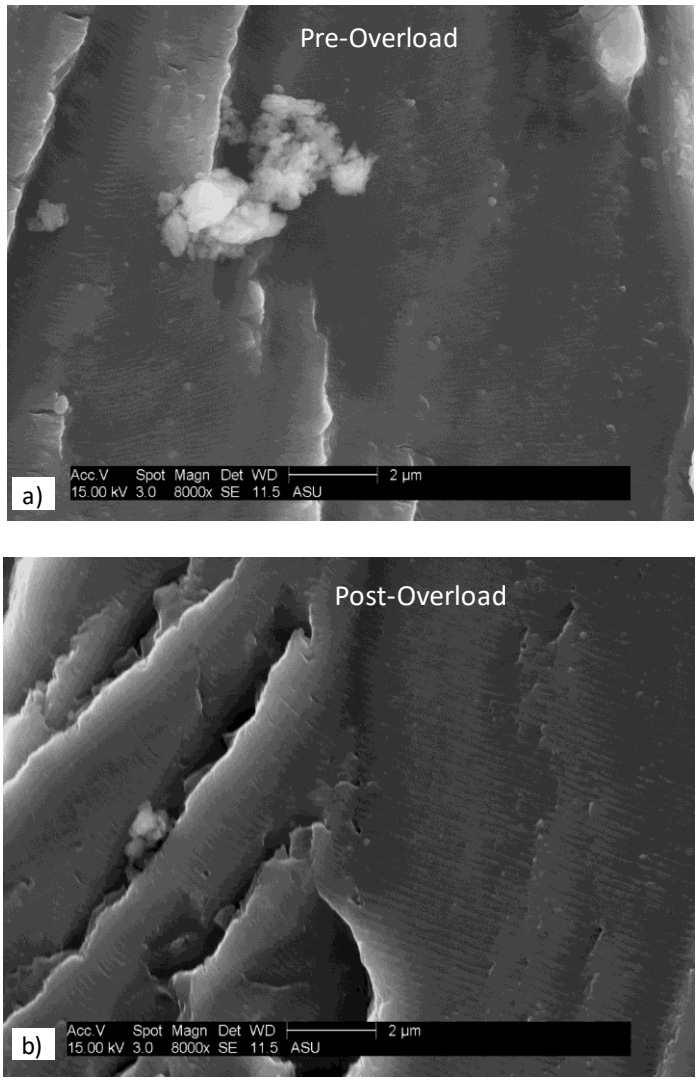

Figure 3.18: Well developed and fully-grown striations were observed in: a) pre-overload region; b) post-overload region for the 1st shear overload with R_{OL} = (2, -2).

region is shown in Figure 3.14(b). Again, striation is the main feature defining this region and suggesting mode I crack propagation.

Fracture features for the second shear overload, which was applied after the completion of 60,000 fatigue cycle, are shown in Figure 3.15 and Figure 3.16. It can be clearly seen that there is no significant difference in the fracture features that can be observed at the

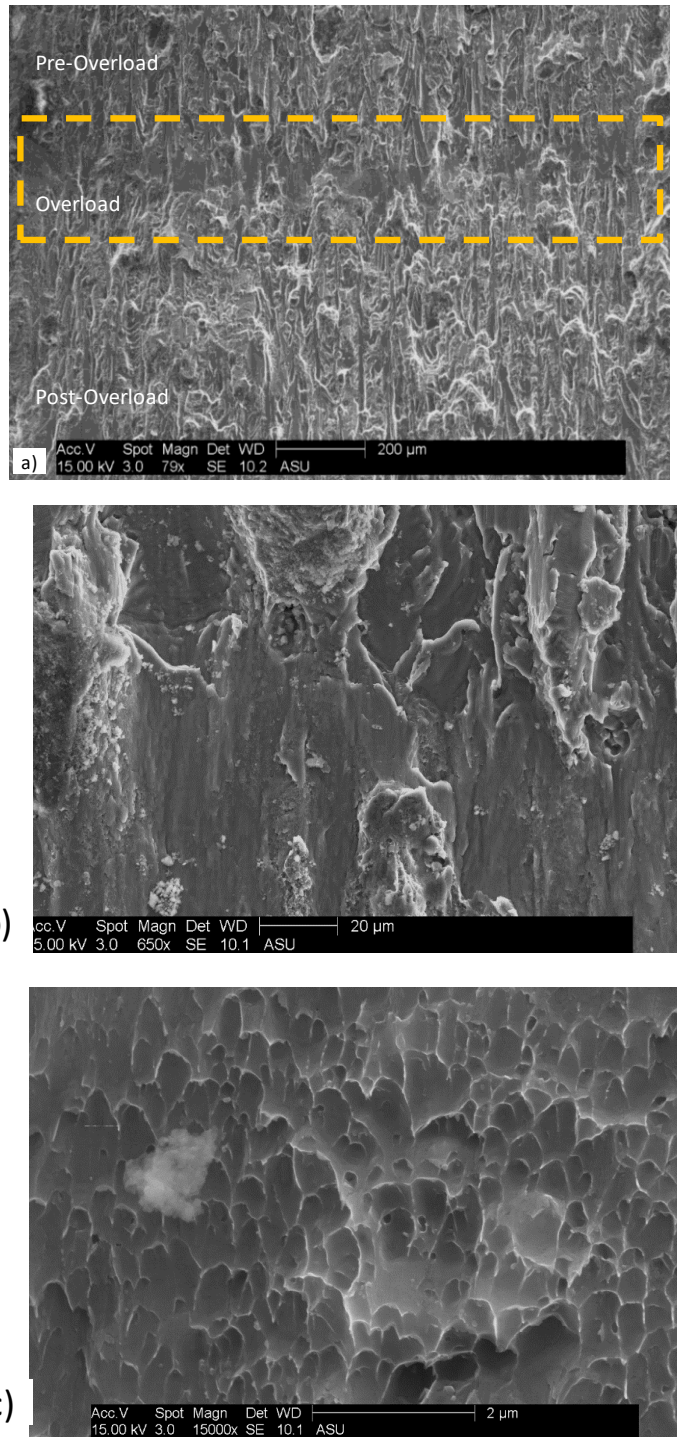

Figure 3.19: a) Microscale fracture features in the transient region of the specimen after the application of 2nd shear overload (60k cycles) with R_{OL} = (2, -2). Magnified images of transient region showing features of shear fracture: b) cleavage steps, tire tracks, tongue etc; c) elongated dimples.

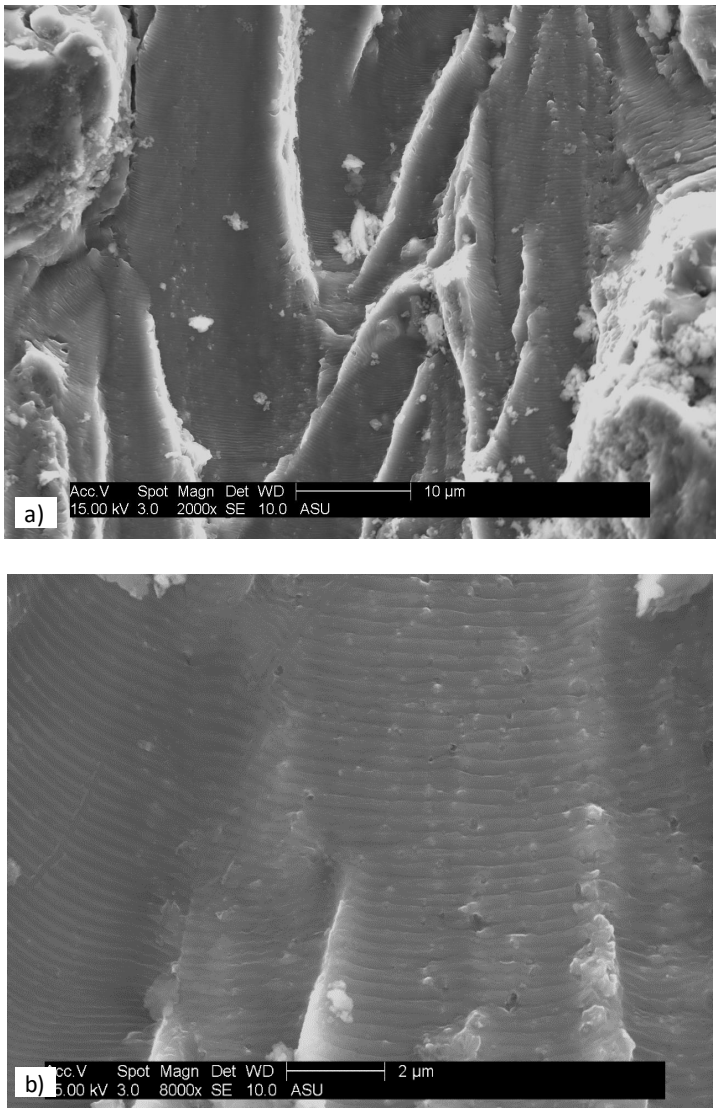

Figure 3.20: Well developed and fully-grown striations were observed in: a) Pre-overload region; b) post-overload region for the 2nd shear overload with R_{OL} = (2, -2).

longer crack length (2nd shear overload) in comparison with its corresponding fracture features observed at the shorter crack length (1st shear overload) for the pre-overload region, overload region, and post-overload region.

3.4.2. R_{OL} = (2, -2)

Microscale fracture features of the specimen corresponding to the shear overload ratio of (2, -2) are presented in Figure 3.17 - Figure 3.18 and Figure 3.19 - Figure 3.20 when the overload was applied at 30,000 cycles and 60,000 cycles respectively. In both the cases, similar to the R_{OL} = (2.5, -2.5), the overloads produced transient zones which consist of a "narrow-region" of smooth surface in an otherwise tortuous region as shown in Figure 3.17 and Figure 3.19 respectively. Magnified images of the transient zones are shown in Figure 3.17(b)-(c) and Figure 3.19(b)-(c) respectively, which show the presence of shear fracture including cleavage steps, tire tracks, tongue and elongated dimples. Figure 3.18(a) and Figure 3.20(a) show the fracture features in pre -overload region, whereas, Figure 3.18(b) and Figure 3.20(b) show the fracture features in the post-overload region. Again, for both the cases (1^{st} overload and 2^{nd} overload), pre-overload and post-overload regions are characterized by the presence of fully-grown striations. These behaviors of the fracture features are similar to the result obtained when the applied overload ratio was (2.5, -2.5).

3.4.3. R_{OL} = (1, -1)

Figure 3.21 and Figure 3.22 show the fracture features for the shear overload ratio of (1, -1). Unlike the previous two overload ratios, where the fracture surface showed a clear distinction between pre-overload region, overload region and post-overload region, here different regions were only partially clear at the 1^{st} overload and there was no distinction found at the 2^{nd} overload. Figure 3.21(b) and Figure 3.21(c) represent the magnified images of the transient region, in which the typical features of shear fracture can be seen; however, there are no features visible on the surface that indicate a fast fracture. Figure 3.22(a) shows

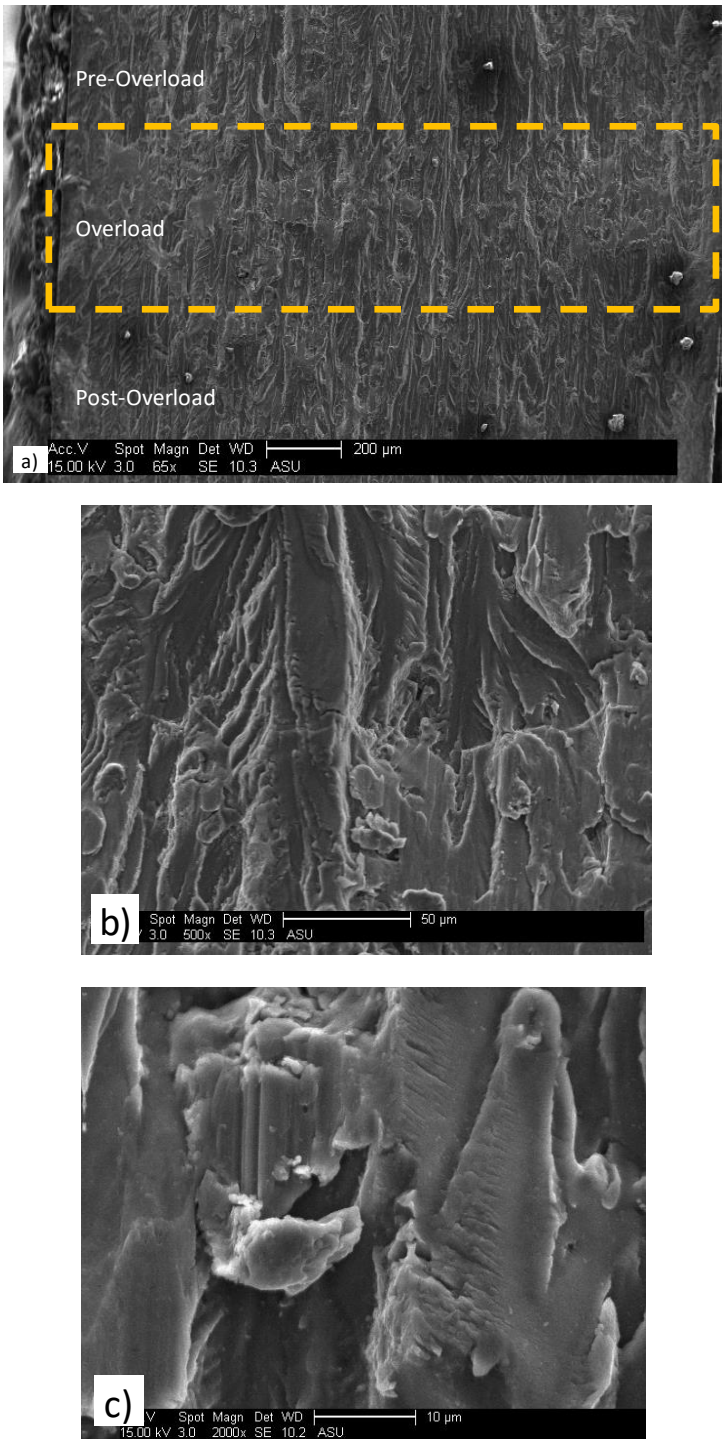

Figure 3.21: a) Microscale fracture features in the transient region of the specimen after the application of 1st shear overload (30k cycles) with R_{OL} = (1, -1). Magnified images of transient region showing features of shear fracture: b) cleavage steps; c) tongue and tire tracks.

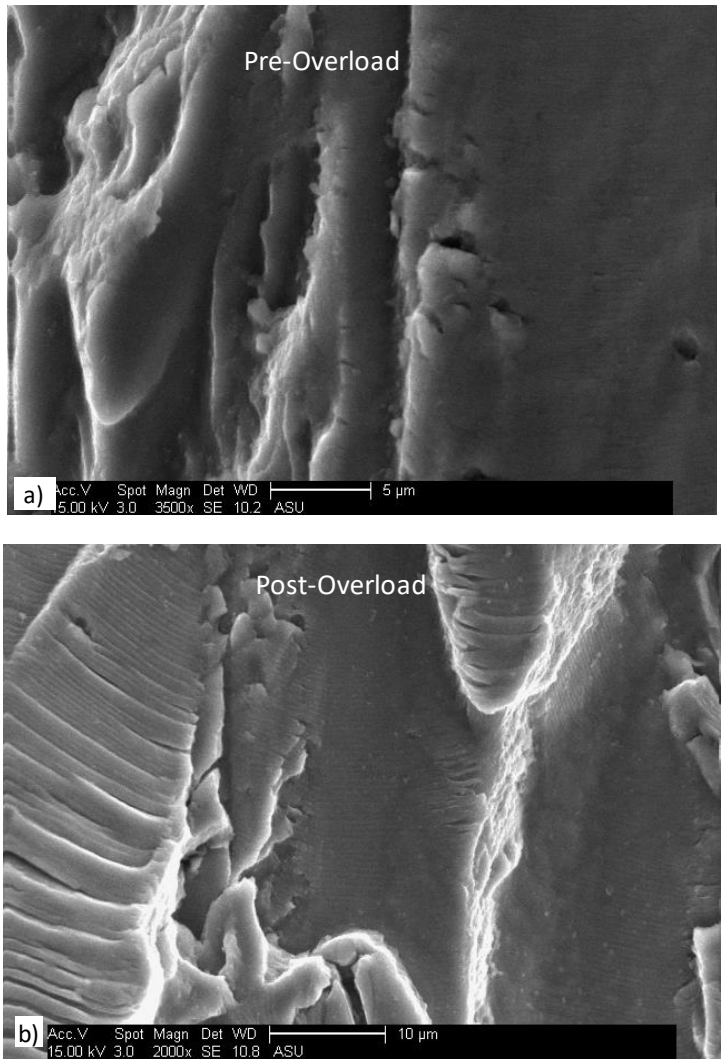

Figure 3.22: Well developed and fully-grown striations were observed in: a) Pre-overload region; b) Post-overload region for the 1st shear overload with R_{OL} = (1, -1).

the pre-overload region which has partially annihilated striations, whereas, the post-overload region has fully-grown striations as shown in Figure 3.22(b).

3.5. Conclusion

In-plane biaxial fatigue tests were performed using cruciform specimen of AA 7075-T651 in order to investigate the effects of shear overloads on fatigue crack propagation

behavior. Furthermore, microscale analysis of the fracture surface was conducted in the vicinity of the transient region to understand the competing micro-mechanism governing fatigue crack propagation behavior. The presented results support the following observations:

- Fatigue life of the specimen increased with the application of shear overload and was found to be proportional to the magnitude of applied overload.
- Crack growth rate showed initial acceleration followed by crack retardation and gradual recovery to the original crack growth rate. The magnitudes of initial acceleration as well as delayed retardation increased with an increase in the values of shear overload. On the other hand, recovery distance showed a linear relationship with the magnitude of overload *SIF* (K_{II}).
- Microscale fracture analysis showed features of shear (fast) fracture in the overload (transient) affected region, whereas, it showed a stable mode I crack growth in pre-overload and post-overload regions.

4. FATIGUE CRACK GROWTH BEHAVIOR UNDER MIX-MODE OVERLOADS

4.1. Introduction

Multiaxial stress states may arise due to material inhomogeneity, residual stresses, specimen geometry, orientation of defects, or external loading [76,80] and is shown in Figure 4.1. Under such conditions, the presence of load fluctuations or random amplitude loading that induces load-interaction effects can further complicate the existing complex multiaxial stress state and often leads to premature failure. These multiaxial variable loadings are often experienced in many critical applications including aircraft, rotorcraft, wind turbines, etc. As shown in Figure 2.1, primary components of an aircraft are exposed to various forms of multiaxial fatigue loading that affects their life in different ways. Any accidental failure of these components during their service life can lead to catastrophic

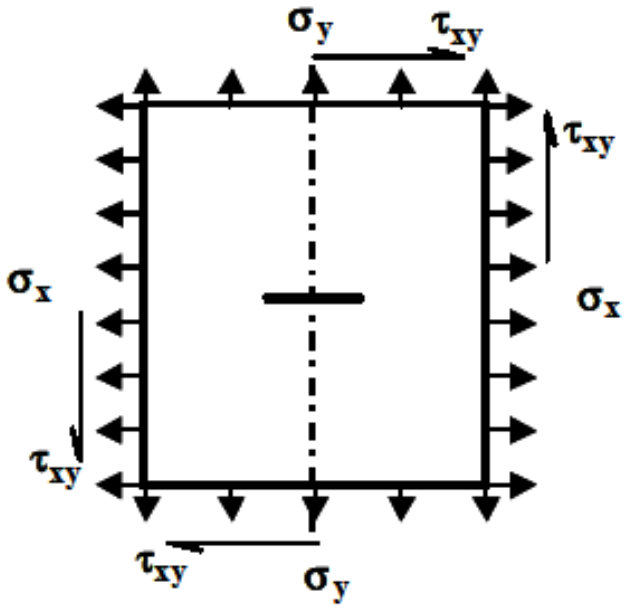

Figure 4.1: Schematic of multiaxial stress state.

damage to life, property, and environment. Therefore, it is important to understand the nature of fatigue damage behavior and identify the underlying micromechanisms governing failure under load excursions in multiaxial fatigue load conditions.

The fracture mechanics (damage tolerance) approach to fatigue failure has had many proponents in the past few decades who have sought to accurately determine the nature of fatigue damage and predict the fatigue life of the specimen. A great majority of the research, following this approach, has been conducted to characterize fatigue behavior in uniaxial loading conditions with or without the presence of overloads [78,81,83,85,96–101]. Several mechanisms, including residual stresses, crack closure, crack tip blunting, strain hardening, crack branching, and reversed yielding have been proposed to explain crack propagation behavior during overload [84,102]. Salvati *et al*. [103] attempted to separate the contribution of residual compressive stress and plasticity-induced crack closure by using energy dispersive X-ray diffraction (EDXRD). Similar techniques were employed by Simpson *et al*. [93] to evaluate the effects of crack closure and residual stress on crack growth behavior. Lopez-Crespo *et al*. [104] demonstrated the presence of plasticity-induced crack closure using digital image correlation (DIC). Despite these efforts, the governing mechanisms for crack propagation due to overloads are not yet fully understood and there exists significant disagreement in the description of precise overload-induced crack growth mechanisms.

In many situations, uniaxial load cases do not accurately depict the exact nature of loading on components in realistic service conditions. As a result, research on the effects of multiaxial stress states on the fatigue behavior of many materials has gained significant

attention. In most of the reported studies, multiaxial load conditions were implemented simply by changing the orientation of the crack or/and using a complex fixture on a uniaxial test frame rather than actually applying external multiaxial loads [33,86–88]. Recently, some researchers have used test frames capable of applying external biaxial loading to study fatigue damage in cruciform specimens in a constant amplitude loading [26–28,89,91,105,106]. Misak *et al*. [91] investigated the crack growth behavior of aluminum alloy 7075-T6 under in-plane biaxial tension–tension fatigue for different biaxiality ratios. Lee *et al*. [89] characterized the effects of biaxiality ratio on fatigue life and crack orientation in aluminum alloys 1100-H14 and AA 7075 T651 subjected to in-phase and out-of-phase loading. Duan *et al*. [28] studied the crack behavior of aluminum alloy 2A12-T4 on cruciform specimens subjected to in-plane biaxial loadings applied in horizontal (X-axis) and vertical (Y-axis) directions. Neerukatti *et al*. [26] studied fatigue damage characteristics of AA 7075 T651 under in-phase and out-of-phase loading conditions and examined the effects of different biaxiality ratios. Wolf *et al*. [27] investigated fatigue crack growth in austenitic steel and aluminum alloy under in-phase as well as phase-shifted loading using cruciform specimens. Meng *et al*. [105] investigated the effects of phase difference and stress ratio on in-plane biaxial tension–tension fatigue crack propagation behavior of rolled ZK60 magnesium alloy. Skinner *et al*. [106] studied damage accumulation and propagation behavior in carbon fiber reinforced polymer (CFRP) composites under complex in-phase biaxial fatigue loading. Although biaxial loadings were used in all the aforementioned studies, the investigation was limited to constant amplitude loading, which rarely is the case in service load condition.

Very few researchers have investigated the effects of load fluctuations under biaxial loading conditions [20,23,24,107,108]. Datta *et al*. [20] investigated crack propagation behavior and the governing micromechanisms in aluminum alloy 7075 under in-plane biaxial fatigue loading with single tensile overloads. It was found that crack retardation at lower overload ratios was governed by plasticity-induced crack closure in the form of crack-tip blunting; whereas, at higher overload ratios, it was a result of the combined influence of crack-tip deflection, plasticity-induced crack closure, and crack-tip splitting. In recent work by the authors [23], the effects of shear overloads on fatigue damage behavior of AA 7075 in biaxial fatigue loading were demonstrated. The fatigue life of the specimen increased with increasing shear overload magnitude, and the crack growth rate in the transient region showed an initial acceleration that was followed by immediate retardation. When the shear overload ratio was increased, the value of initial acceleration further increased, and the subsequent crack growth retardation decreased. Singh *et al*. [107] suggested that the fatigue life of the specimen and its crack propagation behavior is affected by the presence of overload mode-mixity. Despite these investigations, the crack growth behavior and the governing micromechanisms under variable amplitude biaxial loading are not fully understood and remains largely unexplored. In addition, the available experimental data is not only limited but also contradictory when compared with the results under uniaxial load conditions [85,98–100]. The various results presented in the literature suggest that the application of overload, whether in uniaxial or biaxial loading, increases the fatigue life of the specimen [19,20,81,83]; however, crack growth behavior and governing micromechanism displayed different trends in different studies. While most of

the studies on tensile (mode I) overload under uniaxial loading reported only crack retardation [99,101], some studies also showed initial acceleration before the beginning of crack retardation [85,98]. On the other hand, under biaxial loading, initial acceleration was observed only in the case of shear (mode II) overload [23], but not during tensile (mode I) overload [20]. Moreover, the microscale analysis of fracture surfaces showed distinct features and governing mechanisms for tensile (mode I) overload when compared with shear (mode II) overload under biaxial fatigue loading. This brings the need to further investigate the underlying micromechanisms to accurately determine the dominating mechanism that governs post-overload crack propagation behavior in the transient region. Since fatigue damage behavior depends on many factors including material property, specimen geometry, crack orientation, loading conditions, underloads/overload, phase difference, mode-mixity, etc., it is imperative to investigate these complex mechanisms in order to provide accurate estimates of fatigue life. To the best of the author's knowledge, there has not been any comprehensive investigation made to understand the effects of mix-mode overloads on aluminum metallic structures under biaxial fatigue loading.

This chapter presents an experimental investigation to gain a comprehensive insight into the fatigue life and crack propagation behavior in AA 7075 specimens under the influence of mix-mode overloads in an otherwise constant amplitude biaxial fatigue loading. The primary goal is to investigate and characterize macroscale crack growth behavior under such loading and to identify the governing micromechanisms by correlating fracture surface features with loading parameters. The subsequent sections of this chapter are organized as follows: section 2 talks about the specimen design and the methodology used

for conducting macroscale as well as microscale experimental investigations. Section 3 characterizes the macroscale fatigue damage behavior, whereas, section 4 describes the microscale fracture surface analysis and the governing micromechanism. Finally, the last section concludes the chapter and provides a summary of future work.

4.2. Materials and Methods

4.2.1. Material and Specimen Design

The specimens were machined from 0.25” thick aluminum alloy 7075-T6 plate (48” x 48”). This alloy is often used for high-strength applications especially in the aircraft and automotive industries. The material has a yield strength of 503 MPa, ultimate tensile strength of 572 MPa, and modulus of elasticity of 71.7 GPa as per the specification provided by the manufacturer.

Specimen geometry plays an important role in the fatigue behavior of a material, so designing a proper specimen is crucial for accurately determining fatigue life and crack growth behavior. Cruciform specimens have been widely used for planar biaxial loading and are accepted by the research community as they facilitate uniform biaxial stress in the gauge region and readily allow for cyclic biaxial loads, including load excursions during proportional as well as non-proportional loadings [26]. Because of these advantages, a cruciform specimen has been adopted for this investigation. As shown in Figure 4.2, the specimen was designed to ensure a uniform stress distribution in the central web area for initial yielding. These specimens were machined from a 6.35 mm thick rolled plate of AA 7075-T6. The overall horizontal and vertical lengths of the cruciform arms are 292 mm each and they have a thickness of 1.8 mm in the central web region. This region contains a

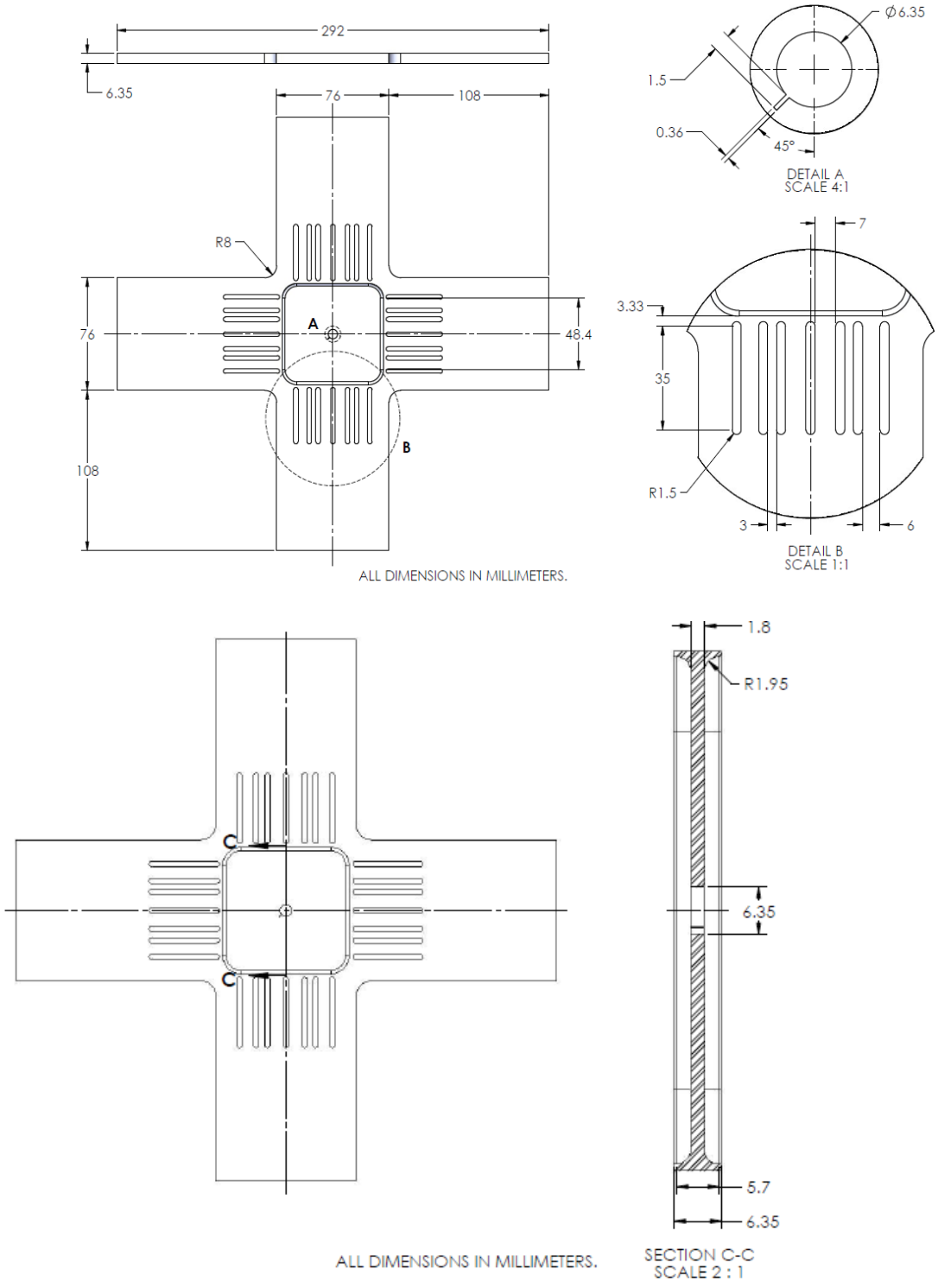

Figure 4.2: Design of cruciform specimen used in biaxial fatigue tests under mix-mode overloads.

hole of diameter 6.35 mm, at which a notch of length 1.5 mm and width of 0.36 mm is made at an angle of 45° (equally inclined to LT and TL direction) to facilitate crack initiation and ensure the favorable orientation for the crack propagation along the 45° plane with respect to the loading axes under pure mode I fatigue loading; thus preventing any arbitrary orientation that may have arisen from the periphery of the central hole in the absence of this notch. Similar notch designs at the center hole of cruciform specimens are used by various authors in the literature [26,91] for their studies.

4.2.2. Experimental Procedure

Fatigue experiments were performed using an MTS planar biaxial/torsion load frame, shown in Figure 4.3, which has a dynamic load capacity of 100 kN in both horizontal and vertical directions and a torsional load capacity of 1100 N.m. The load frame is equipped with six actuators as shown in Figure 4.3(a), which can be independently controlled to conduct fatigue tests under a wide range of biaxial load conditions, including load excursions during proportional as well as non-proportional loadings. A magnified image of the test setup is shown in Figure 4.3(b), in which the two vertical and the two horizontal actuators grip the cruciform specimen and apply loads in vertical and horizontal directions simultaneously. All the tests were conducted in a load-controlled mode having a maximum cyclic load, P_{max}, of 15 kN with the stress ratio (R) of 0.1 applied at a frequency of 10 Hz. Load excursions of different mode-mixity were introduced in the loading spectra by varying the magnitudes of overloads in horizontal (X-direction) and vertical (Y-direction) axes in an otherwise constant amplitude biaxial fatigue loading as shown in Figure 4.4. To generate the required load spectra corresponding to different values of overload magnitude,

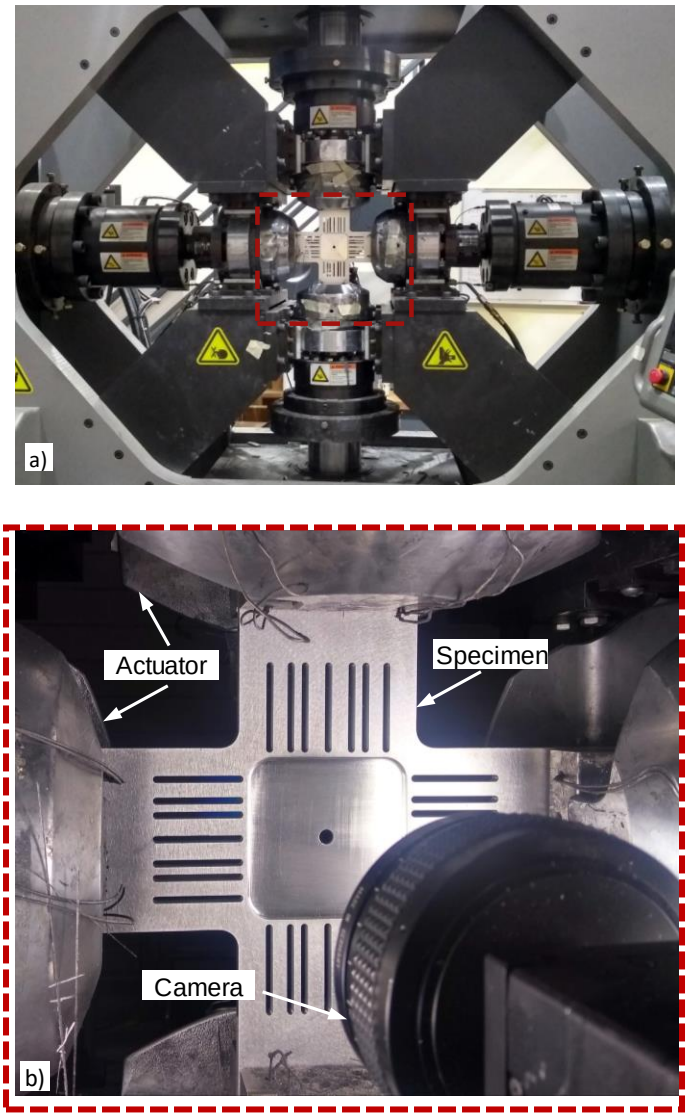

Figure 4.3: Experimental set-up used to conduct fatigue tests under different load conditions: a) biaxial test frame; b) magnified image showing cruciform specimen mounted on test frame.

mode-mixity, and crack length, separate scripts were written in the machine supported format and then implemented in the load frame to conduct various fatigue tests. For each value of mix-mode overload, several specimens were tested to investigate its effect on fatigue life and crack propagation behavior as detailed in Table 4.1; where, *OL* = overload,

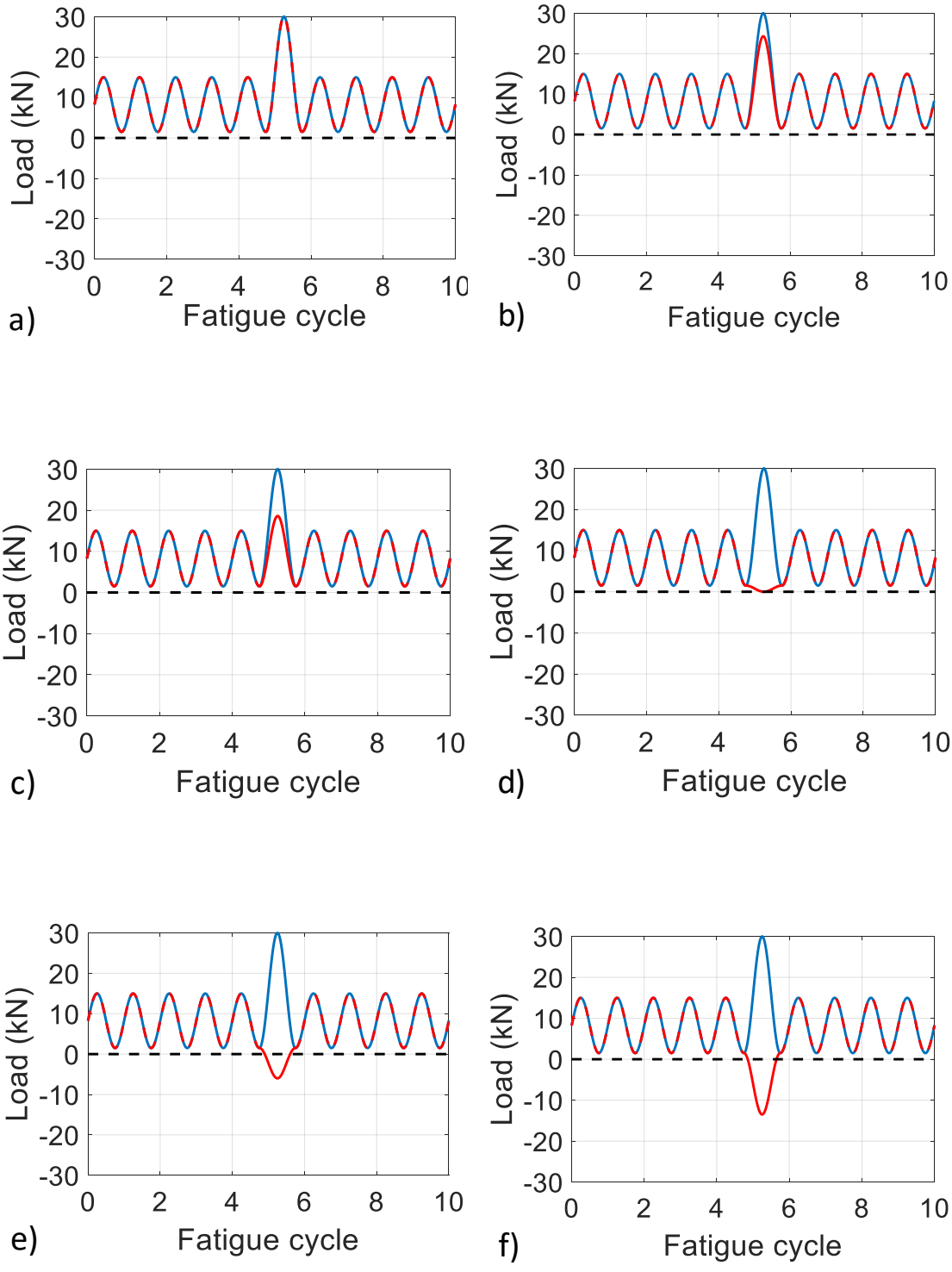
Load (kN)
Fatigue cycle
a)
b)
c)
d)
e)
f)

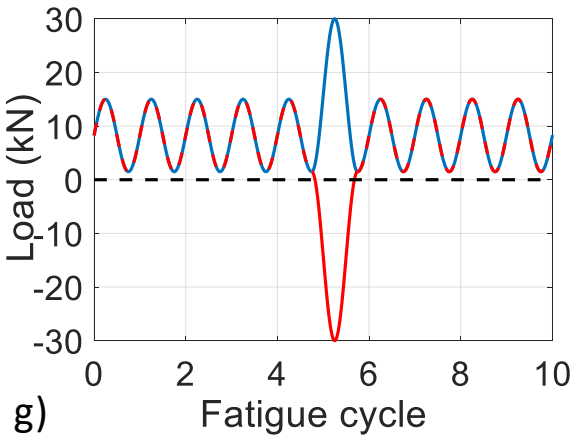

Figure 4.4: Schematic of load spectrums used to generate different values of mode-mixity during the applied overload: a) ϕ_M = 0° (pure tensile); b) ϕ_M = 6.3°; c) ϕ_M = 14°; d) ϕ_M = 45°; e) ϕ_M = 56.3°; f) ϕ_M = 66.8°; g) ϕ_M = 90° (pure shear). The loadings in X- direction and Y- direction are shown by blue and red lines respectively.

$P_{OL\text{-}X}$ = overload in X-axis; $P_{OL\text{-}Y}$ = overload in Y-axis, $R_{OL\text{-}X}$ = overload ratio in X-axis ($P_{OL\text{-}X}/P_{max}$), $R_{OL\text{-}Y}$ = overload ratio in Y-axis ($P_{OL\text{-}Y}/P_{max}$), λ_{OL} = overload biaxiality ratio ($R_{OL\text{-}Y}/R_{OL\text{-}X}$), ϕ_M = mode-mixity ($\tan^{-1}\frac{K_{II}}{K_I}$), N_{OL} = fatigue cycle at overload. These overloads were applied at two different crack lengths corresponding to 30,000 and 60,000 fatigue cycles to study the effects of overload mode-mixity on fatigue cracks of different lengths. A high-resolution camera was mounted on the rear side of the specimen to continuously monitor crack length. The camera was programmed using LabVIEW to take images at user-defined time intervals to capture crack initiation and propagation behavior. An image processing software ImageJ was used to measure the fatigue crack lengths at different fatigue cycles. This allowed calculation of the cycles for crack initiation, crack propagation, final failure, and the crack growth rate at each crack increment.

Table 4.1:

Loading conditions for fatigue tests under mix-mode overloads.

OL Type	**P_{OL-X} (kN)**	**P_{OL-Y} (kN)**	**R_{OL-X}**	**R_{OL-Y}**	**λ_{OL}**	**φ_M**	**N_{OL} (cycles)**
MM1	30	30	2	2	1	0°	30,000
							60,000
MM2	30	24	2	1.6	0.8	6.3°	30,000
							60,000
MM3	30	18	2	1.2	0.6	14°	30,000
							60,000
MM4	30	0	2	0	0	45°	30,000
							60,000
MM5	30	-6	2	-0.4	-0.2	56.3°	30,000
							60,000
MM6	30	-12	2	-0.8	-0.4	66.8°	30,000
							60,000
MM7	30	-30	2	-2	-1	90°	30,000
							60,000

To understand the governing micromechanisms, fractography was performed on the fatigued specimens using SEM. Fracture surface morphology was studied to identify the microscale fracture features corresponding to the overloads of different mode-mixity and to correlate them with macroscopic crack growth behavior in the pre-overload region, overload affected transient region, and post-overload region. These analyses were conducted for both the crack lengths corresponding to 30,000 and 60,000 fatigue cycles where the overloads were applied. The fractographic analysis was conducted by cutting out a portion of the fracture surface from the fatigued cruciform specimens using a low-speed diamond saw. The segment was then sonicated in acetone to remove debris and the cutting fluid. Cleaned fracture surfaces were dried using compressed air and then mounted onto metallic stubs for SEM analysis.

4.3. Result and Discussion

A total of 22 specimens were tested to investigate the effects of mix-mode overloads for seven different values of mode-mixity as shown in Table 4.1. These overloads were applied at 30,000 and 60,000 fatigue cycles to compare the effects of mode-mixity at a shorter crack length against a longer crack length. For all the tests, irrespective of the values of overload mode-mixity, the macroscopic crack continued to propagate along the direction of initial notch, i.e. at 45°, and the crack trajectory remained unaffected by the presence of mix-mode overload applied in the form of spike load at different crack lengths as shown in Figure 4.5. Since the cyclic portion of the applied load was biaxial with the biaxiality ratio (λ) equal to 1, the propagation of crack at 45° implies pure mode I loading at crack-tip, which is anticipated and observed by other authors in their uniaxial or biaxial tests

[103,109]. However, the tendency of the crack to continue its original trajectory after the applied overload and in the transient region is different from the general understanding presented in the literature that advocates for the deviation of a crack tip or branching in an event of shear or mix mode loading [1,19].

4.3.1. Fatigue Life

The damage tolerance design concept (fracture mechanics) was invoked to determine the effect of overload mode-mixity on the fatigue life of the specimen. Crack lengths corresponding to different values of the fatigue cycle were measured for all the tests using the image processing software (ImageJ) and is shown in Figure 4.6. This figure shows seven different curves corresponding to results obtained under seven different values of overload mode-mixity, i.e. 0°, 6.3°, 14°, 45°, 56.3°, 66.8°, 90°. In all these cases, the trajectory of the crack length – fatigue cycle curve; and the crack lengths corresponding to their respective fatigue cycle in different tests remained the same until the application of the first overload at 30,000 cycles because the loading conditions are identical until this point. Immediately after the application of overload, all the curves indicate various levels of crack growth retardation as they deviate from the initial trajectory and thereafter trace separate paths. As a result of the crack retardation, additional fatigue cycles are required to attain the same length of the crack that would have been achieved without the overload. The resulting increase in specimen fatigue life depends on the value of mode-mixity during the overload. For clarity, analysis of tensile-dominant overloads was separated from shear-dominant overloads and are presented in Figure 4.6(a) and Figure 4.6(b), respectively.

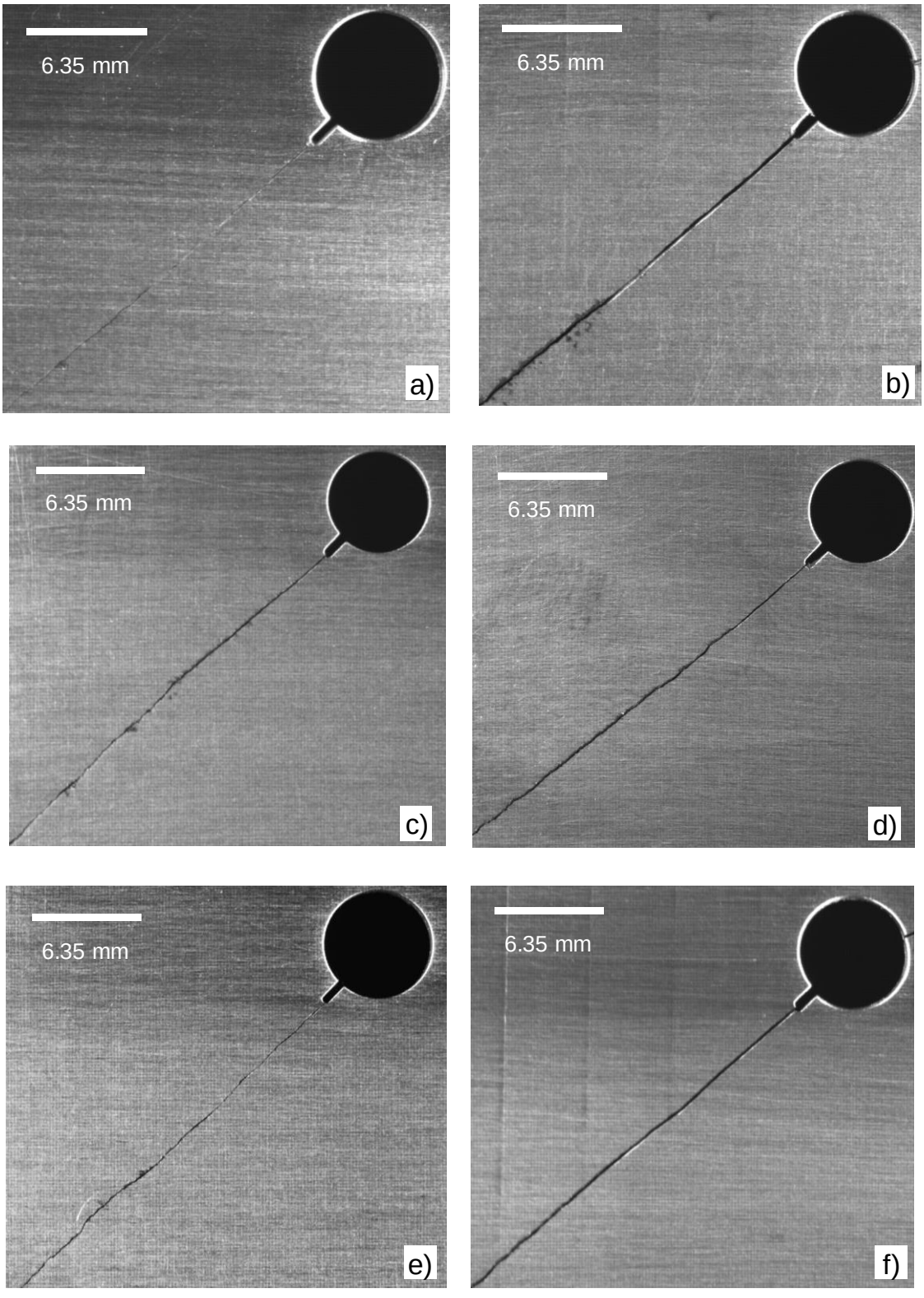
6.35 mm
a)
6.35 mm
b)
6.35 mm
c)
6.35 mm
d)
6.35 mm
e)
6.35 mm
f)

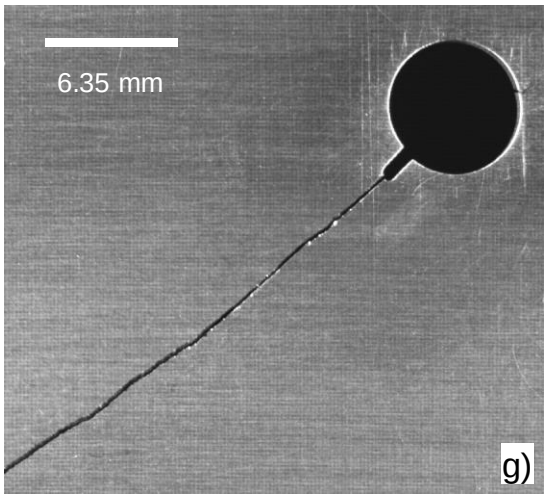

Figure 4.5: Orientation and trajectory of the fatigue crack subjected to overloads of different mode-mixity: a) ϕ_M = 0° (pure tensile); b) ϕ_M = 6.3°; c) ϕ_M = 14°; d) ϕ_M = 45°; e) ϕ_M = 56.3°; f) ϕ_M = 66.8°; g) ϕ_M = 90° (pure shear).

As shown in Figure 4.6(a), the fatigue life of the specimen decreases with an increase in the shear component during tensile-dominant overloads. The maximum increase in fatigue life occurs for the mode-mixity (ϕ_M) of 0°, i.e. pure tensile overload, and the minimum increase occurs when the value of ϕ_M is 45°. A significant decrease in fatigue life occurs by merely increasing the value of ϕ_M from 0° to 14° degree, and a comparatively small decrease in fatigue life is observed by further increasing the value of ϕ_M to 45°. Dramatic flattening of the curve immediately after overload occurs in the cases with small ϕ_M and is evidence of crack arrest [20]. The results from shear-dominant overloads are shown in Figure 4.6(b), in which fatigue life increases with increasing overload shear component. While increasing the shear component appears to slow down the crack propagation, no evidence of crack arrest is seen in the shear-dominant overloads, which is consistent with results from the literature [23]. The maximum increase in fatigue life for the shear-dominated overloads occurs when ϕ_M is 90°, i.e. pure shear overload, and the

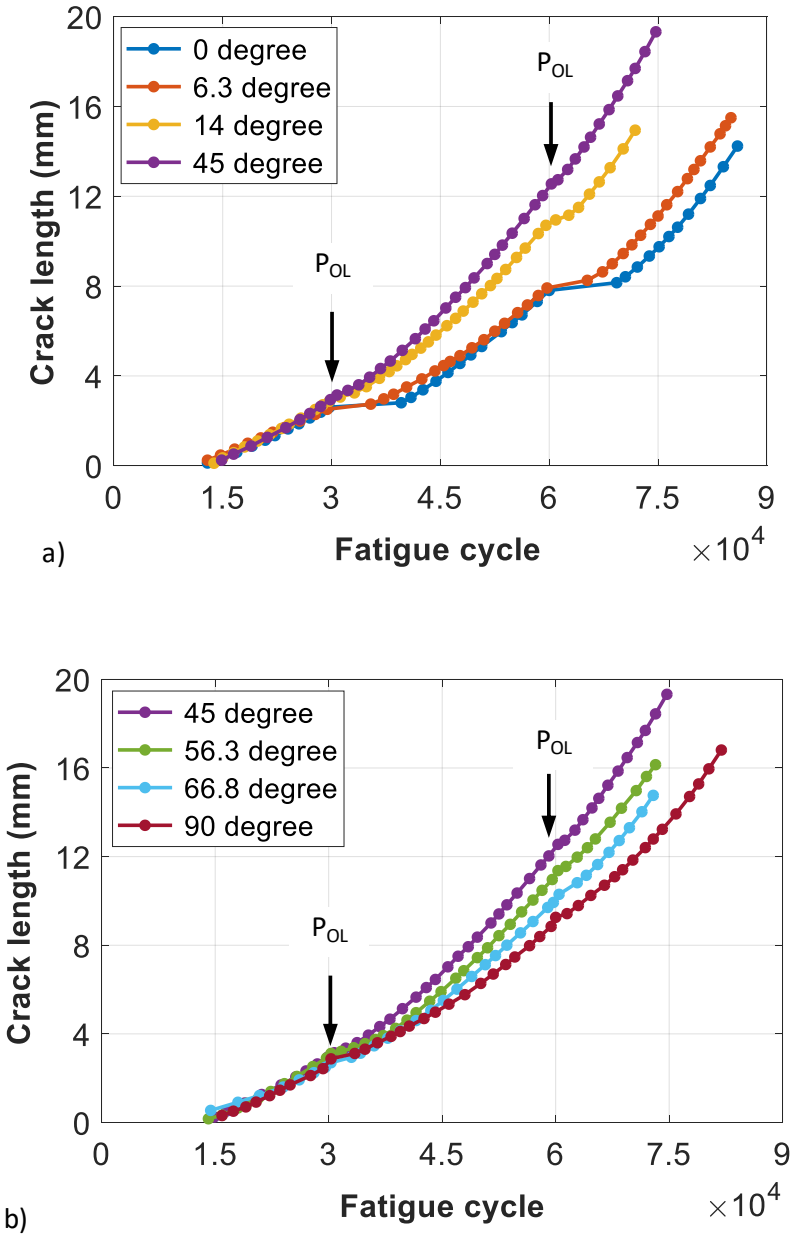

Figure 4.6: Plot of crack length vs. fatigue cycles for different values of overload mode-mixity in: a) tensile-dominant overload ($\phi_M \leq 45°$); b) shear-dominant overload ($\phi_M \geq 45°$).

Table 4.2:

Crack growth behavior under mix-mode overloads.

OL Type	φ_M	a_{OL} (mm)	ΔK_I (MPa.m$^{1/2}$)	R_d (mm)	da/dN (mm/cycle)			N_{OL} (cycles)
					Pre-OL	OL	Post-OL	
MM1	0°	2.39	10.97	0.280	$1.72\text{x}10^{-4}$	$1.81\text{x}10^{-4}$	$2.03\text{x}10^{-5}$	30,000
		7.32	13.66	1.284	$2.85\text{x}10^{-4}$	$2.98\text{x}10^{-4}$	$3.69\text{x}10^{-5}$	60,000
MM2	6.3°	2.29	10.9	0.443	$1.42\text{x}10^{-4}$	$1.38\text{x}10^{-4}$	$3.82\text{x}10^{-5}$	30,000
		7.58	13.8	1.229	$2.81\text{x}10^{-4}$	$2.79\text{x}10^{-4}$	$6.13\text{x}10^{-5}$	60,000
MM3	14°	2.71	11.19	0.707	$2\text{x}10^{-4}$	$1.78\text{x}10^{-4}$	$9.49\text{x}10^{-5}$	30,000
		10.34	15.06	1.228	$3.60\text{x}10^{-4}$	$3.49\text{x}10^{-4}$	$1.16\text{x}10^{-4}$	60,000
MM4	45°	2.94	11.34	0.963	$2.23\text{x}10^{-4}$	$2.28\text{x}10^{-4}$	$1.37\text{x}10^{-4}$	30,000
		12.03	15.83	1.291	$3.89\text{x}10^{-4}$	$4.34\text{x}10^{-4}$	$2.04\text{x}10^{-4}$	60,000
MM5	56.3°	2.91	11.31	1.242	$2.13\text{x}10^{-4}$	$3.50\text{x}10^{-4}$	$6.89\text{x}10^{-5}$	30,000
		10.97	15.34	1.534	$3.61\text{x}10^{-4}$	$5.36\text{x}10^{-4}$	$1.80\text{x}10^{-4}$	60,000
MM6	66.8°	2.49	11	1.316	$1.62\text{x}10^{-4}$	$3.43\text{x}10^{-4}$	$8.63\text{x}10^{-5}$	30,000
		9.71	14.8	1.739	$3.03\text{x}10^{-4}$	$6.08\text{x}10^{-4}$	$2.06\text{x}10^{-4}$	60,000
MM7	90°	2.43	11	1.427	$1.88\text{x}10^{-4}$	$4.21\text{x}10^{-4}$	$7.71\text{x}10^{-5}$	30,000
		8.85	14.4	2.417	$3.05\text{x}10^{-4}$	$6.83\text{x}10^{-4}$	$1.40\text{x}10^{-4}$	60,000

minimum increase occurs when ϕ_M is 45°. On combining the two results (tensile-dominant and shear-dominant), it is clear that the minimum increase in fatigue life occurs when ϕ_M is 45°. As this value changes either by increasing the tensile component (i.e. $\phi_M < 45°$) or by increasing the shear component (i.e. $\phi_M > 45°$), a further increase in fatigue life occurs. When the second overload is applied at a longer crack length corresponding to 60,000 fatigue cycles, the observed results for all the values of ϕ_M are similar to the results for the overload at a shorter crack length.

4.3.2. Crack Propagation

Figure 4.7 shows the plots of crack growth rate (da/dN) vs. the cyclic value of stress intensity factor (*SIF*) range obtained under constant amplitude pure mode I loading for seven different values of overload mode-mixity applied at 30,000 and 60,000 fatigue cycles. The magnitude of *SIF* (mode I) for the given cyclic loading at various crack lengths were calculated using methodologies outlined in previous research [23]. The plots in Figure 4.7, show that the crack growth rate in the transient region is highly dependent on the value of ϕ_M during the overload. Consequently, different trends are evident for initial acceleration and crack retardation during tensile-dominant ($\phi_M < 45°$) and shear dominant ($\phi_M > 45°$) overloads. When the value of ϕ_M is less than or equal to 45° (Figure 4.7(a) – (d)), only the crack retardation occurs in the transient region with no evidence of initial acceleration. Figure 4.7(a) shows the da/dN for the smallest value of ϕ_M, i.e. 0° (pure tensile), in which a delayed but significant post-overload retardation occurs, resulting in a crack arrest. This behavior is evident following both overloads and appears to be independent of the value of cyclic *SIF* (ΔK_I) at the time of overload. As the magnitude of ϕ_M increases from 0° to 45°

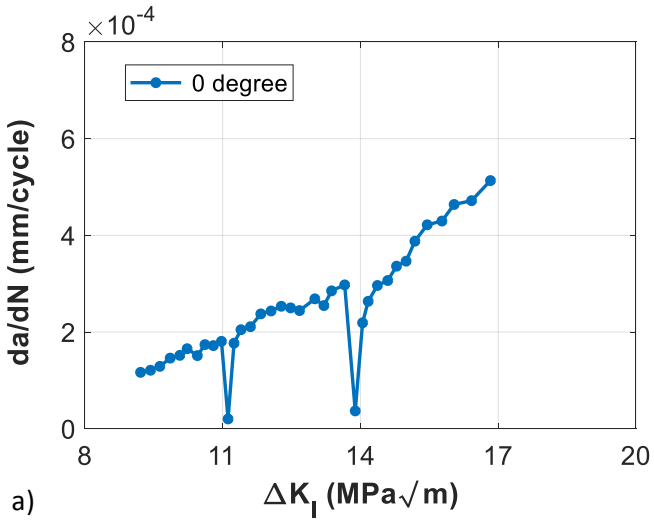
×10^-4
8
6
4
2
0
0 degree
da/dN (mm/cycle)
8
11
14
17
20
ΔK_I (MPa√m)

a)

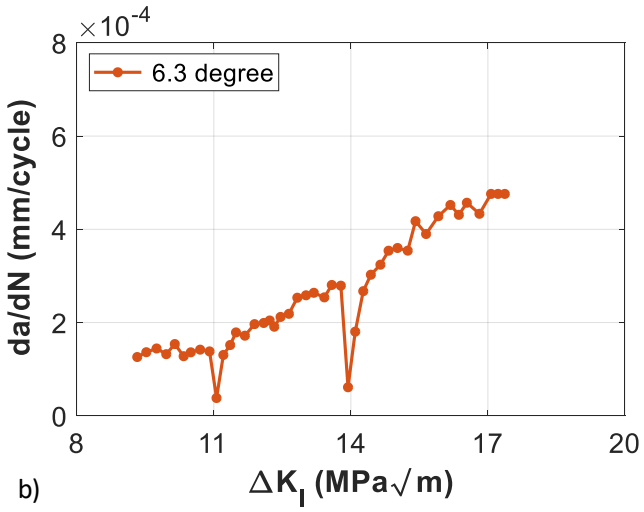
×10^-4
8
6
4
2
0
6.3 degree
da/dN (mm/cycle)
8
11
14
17
20
ΔK_I (MPa√m)

b)

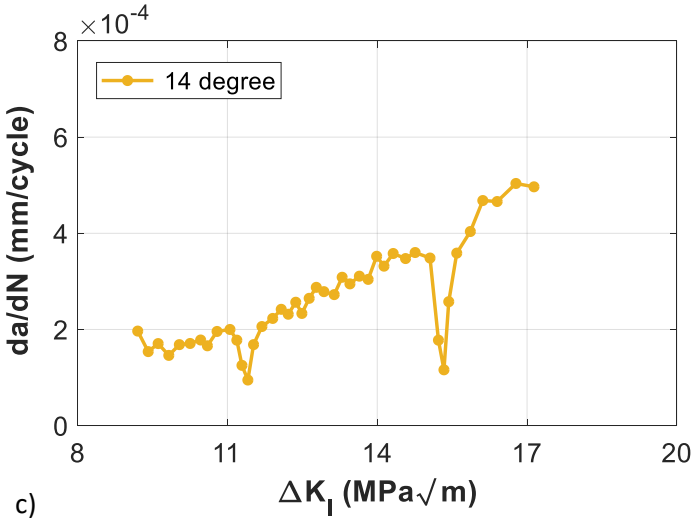
×10^-4
8
6
4
2
0
14 degree
da/dN (mm/cycle)
8
11
14
17
20
ΔK_I (MPa√m)

c)

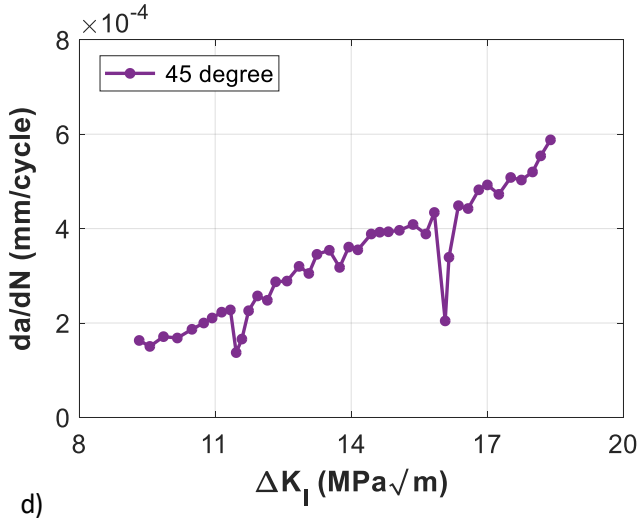
×10^-4
8
6
4
2
0
45 degree
da/dN (mm/cycle)
8
11
14
17
20
ΔK_I (MPa√m)

d)

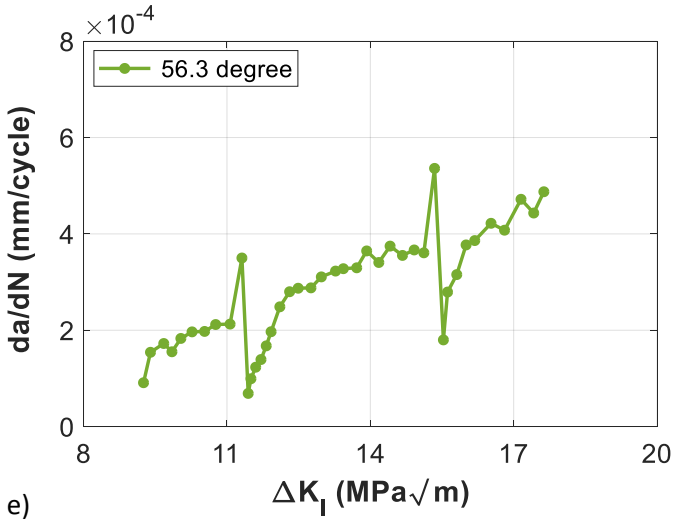
×10^-4
8
6
4
2
0
56.3 degree
da/dN (mm/cycle)
8
11
14
17
20
ΔK_I (MPa√m)

e)

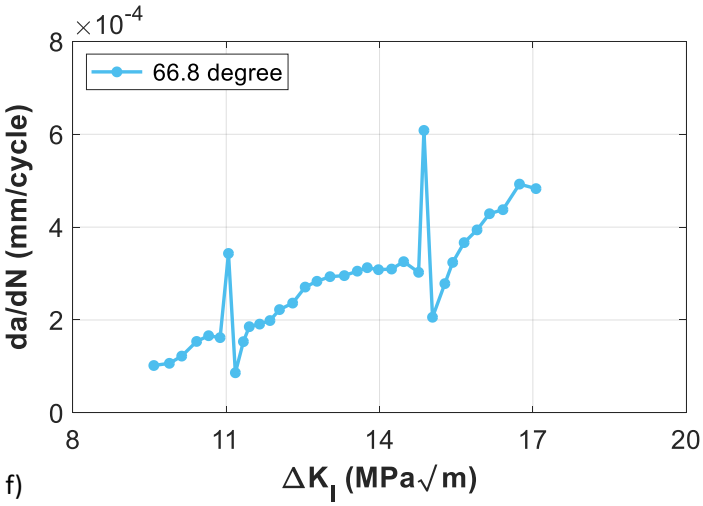
×10^-4
8
6
4
2
0
66.8 degree
da/dN (mm/cycle)
8
11
14
17
20
ΔK_I (MPa√m)

f)

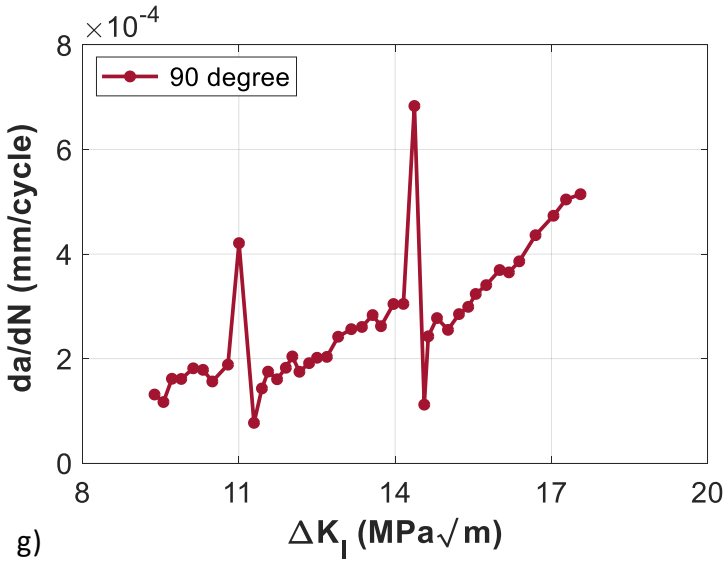

Figure 4.7: Crack growth rate is plotted against ΔK_I for different values of overload mode-mixity applied at the end of 30,000 cycle and 60,000: a) ϕ_M = 0° (pure tensile); b) ϕ_M = 6.3°; c) ϕ_M = 14°; d) ϕ_M = 45°; e) ϕ_M = 56.3°; f) ϕ_M = 66.8°; g) ϕ_M = 90° (pure shear).

(Figure 4.7(a) – (d)), a corresponding decrease in the magnitude of crack retardation occurs whether the overload is applied at a shorter crack length (30,000 cycles) or the longer crack length (60,000 cycles). However, at any given value of ϕ_M (tensile-dominant), when the same overload is applied at a longer crack length (i.e. higher ΔK_I), a higher degree of crack retardation is observed compared to the smaller crack length (i.e. lower ΔK_I).

During shear-dominant overload, when the value of ϕ_M is greater than 45° (Figure 4.7(e)–(g)), a different trend in the crack growth rate emerges. As shown in Figure 4.7(e), the transient region shows initial crack acceleration which is immediately followed by crack retardation. The initial acceleration is a short-lived phenomenon (~300 cycles) as compared to the retardation (~9,000 cycles). As the value of ϕ_M increases from 56.3° to 90° (Figure 4.7(e)–(g)), the magnitude of initial acceleration further increases. For any given

value of ϕ_M (shear-dominant), when the same overload was applied at a longer crack length, an increase in the magnitudes of initial acceleration as well as crack retardation was observed. Among the tensile overloads, a very few of the researchers noticed an initial acceleration in the crack growth rate only when the overload ratio was higher than 1.5 [84,85]. However, in the limited research available on the shear overloads, both the initial acceleration and the delayed retardation was observed under biaxial loading [23,24].

4.3.3. Recovery Distance

Recovery distance (R_d) is used to quantify the size of the transient zone created as a result of load excursions in an otherwise constant amplitude loading. It is defined as the distance traveled by the crack-tip after an overload until the crack retardation/acceleration effects wear off and the crack growth rates resume their normal values. Although Figure 4.8 shows the crack growth rate only for three different values of ϕ_M (0°, 45°, 90°), as the crack acquired different lengths during its propagation with or without the presence of overload, recovery distance was calculated for all the values of ϕ_M (0°, 6.3°, 14°, 45°, 56.3°, 66.8°, 90°) using their respective plots of crack growth rate vs. crack length. The methodology adopted in determining R_d has been explained in detail in the previous research [23] and the values of R_d thus obtained are shown in Table 4.2. Figure 4.9 shows the plots of R_d against the normalized values of $\phi_{M,}$ which are applied on a shorter crack length (30,000 cycles) and a longer crack length (60,000 cycles). As shown in Figure 4.9(a), when the overload is applied at the shorter crack length, the magnitude of R_d continuously increases with an increase in ϕ_M from 0° (pure tensile) to 90° (pure shear). However, a different trend is observed when the same overload is applied at the longer crack length as

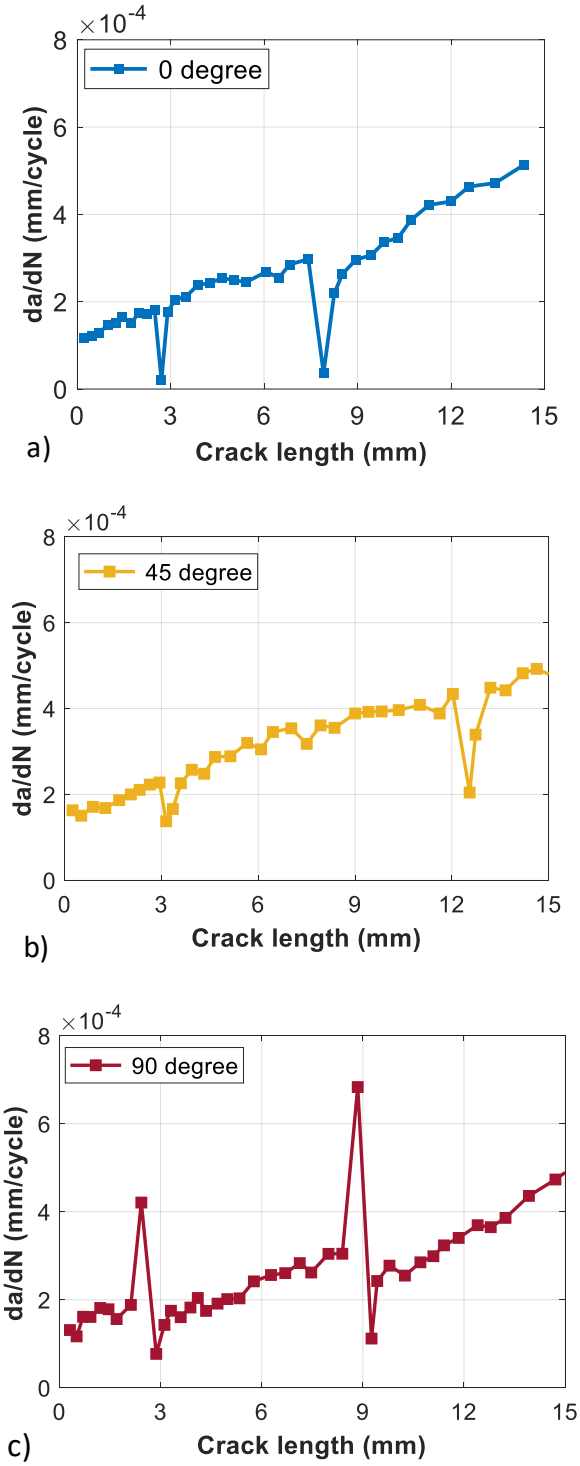

Figure 4.8: Crack growth rate is plotted against crack length for different values of overload mode-mixity applied at the end of 30,000 cycle and 60,000: a) ϕ_M = 0°; b) ϕ_M = 45°; c) ϕ_M = 90°.

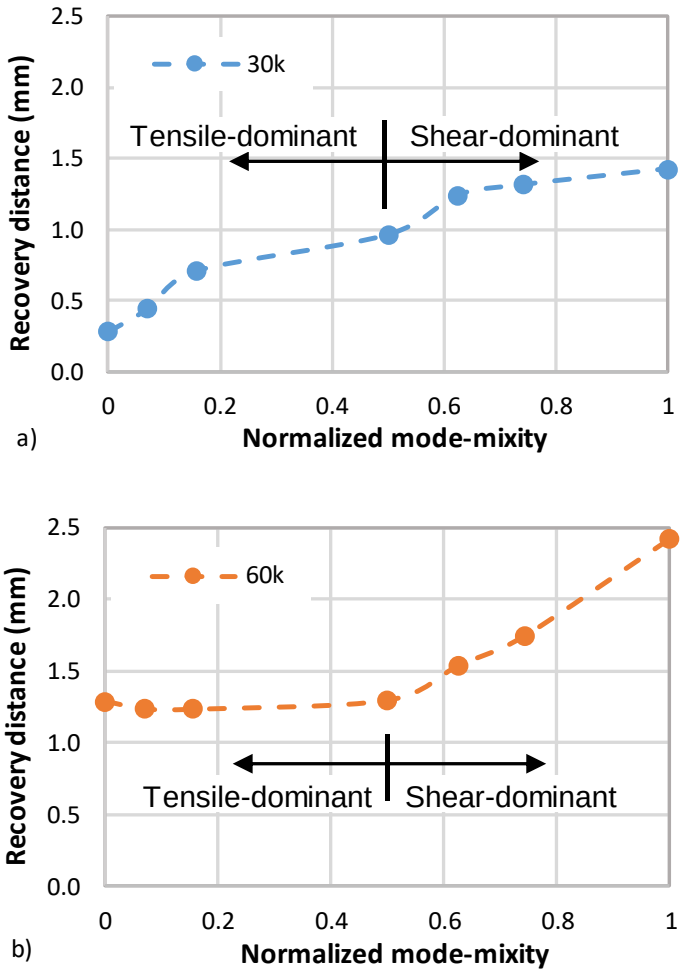

Figure 4.9: Recovery distance vs. normalized values of overload mode-mixity obtained at: a) small crack length (30,000 cycle); b) large crack length (60,000 cycle).

shown in Figure 4.9(b). With an increase in ϕ_M, there is no significant change in the value of R_d during tensile dominant overload ($\phi_M \leq 45°$), whereas, during the shear-dominant overload ($\phi_M \geq 45°$), a linear increase in R_d occurs with an increase in ϕ_M.

Crack propagation behavior is dominated by multiple distinct and competing mechanisms depending on microstructure, loading, environmental conditions, etc. Among them, strain hardening is a dominating mechanism that governs the size of the transient

zone (R_d) during an overload [23]. The additional dislocations generated during the plastic deformation results in the strain hardening that increases the strength of material by further resisting the dislocation motion. As a result, the crack driving force must overcome an increased resistance over an extended region giving rise to R_d. Since the size of the plastic zone (along the crack line) under mode II loading is up to five times bigger than that in mode I loading [1], an increase in the value of R_d occurs by increasing the mode-mixity (mode II component of loading) as shown in Figure 4.9(a). As shown in Figure 4.9(b), the R_d in the tensile dominant region of longer crack length does not change with an increase in overload mode-mixity but increases with an increase in overload mode-mixity in the shear dominant region. This behavior could be the result of competing mechanisms operating at the longer crack length in the tensile dominant region and needs further investigation. With respect to shorter crack length, a higher value of R_d occurs at longer crack length when the overload of the same mode-mixity is applied. This aligns with expectations since there is more plastic deformation at longer crack length.

4.4. Governing Micromechanisms

Fracture surface analysis was performed using SEM images of different magnifications to gain a comprehensive insight into various competing micromechanisms responsible for governing fatigue crack propagation under different loading conditions as shown in Figure 4.10 – Figure 4.13. Distinct fracture features of the pre-overload region, overload affected transient region, and post-overload region were identified and correlated with their characteristic micromechanisms to determine the dominant crack growth mechanism operating at each mode-mixity (tensile-dominant and shear-dominant) of the applied

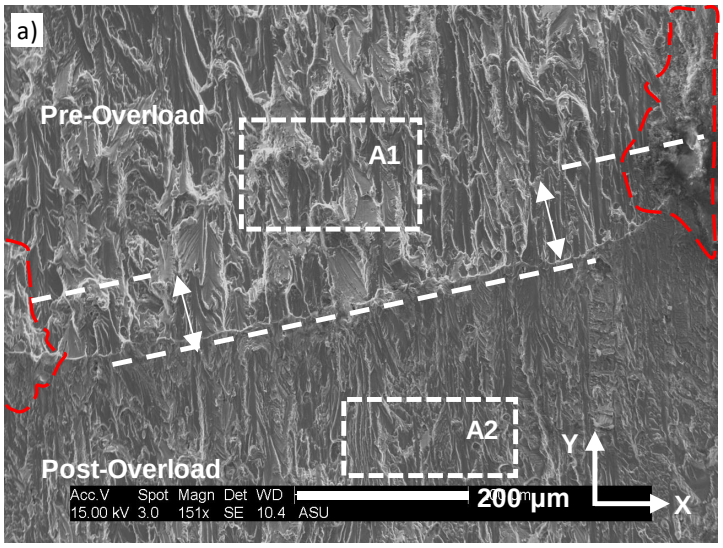
a)
Pre-Overload
A1
A2
Post-Overload
Y
X
Acc.V Spot Magn Det WD
15.00 kV 3.0 151x SE 10.4 ASU
200 µm

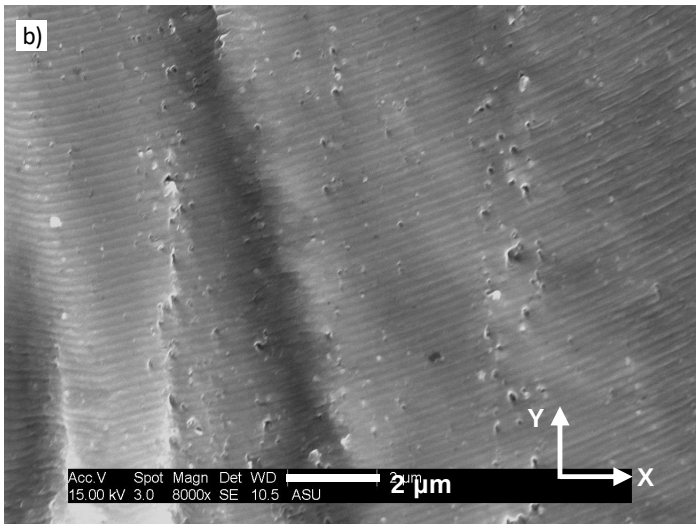
b)
Y
X
Acc.V Spot Magn Det WD
15.00 kV 3.0 8000x SE 10.5 ASU
2 µm

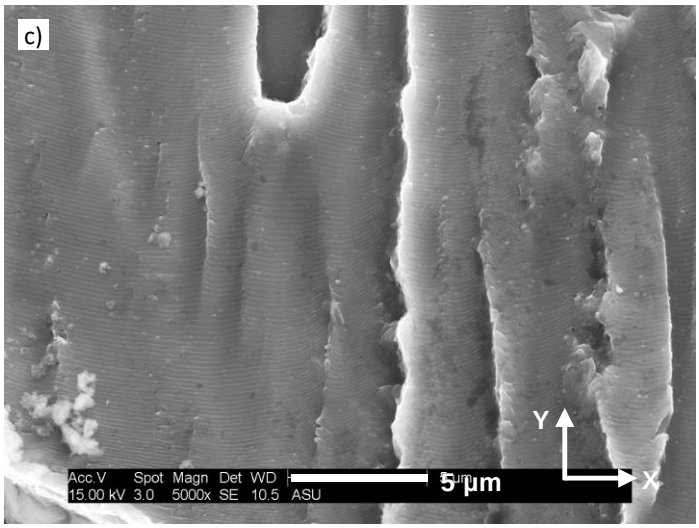
c)
Y
X
Acc.V Spot Magn Det WD
15.00 kV 3.0 5000x SE 10.5 ASU
5 µm

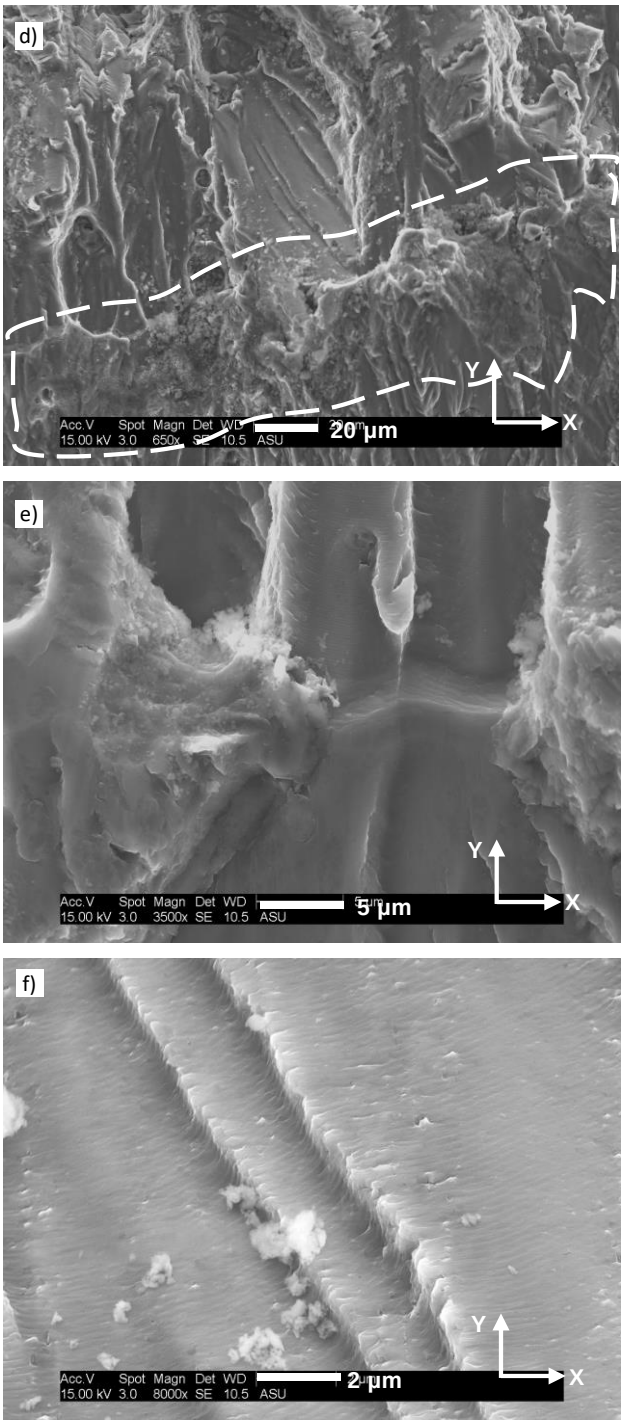

Figure 4.10: Microscale fracture features of the specimen subjected to tensile-dominant overload (ϕ_M = 14°) at 30k cycles: a) overload affected region (low magnification); b) pre-overload region; c) post-overload region. Magnified images of transient region showing: d) overload line along with tortuous surface; e) smooth and featureless facets; f) annihilated striations.

overloads. At each value of mode-mixity, overload was applied at 30,000 (~2.5mm crack length) and 60,000 (~10mm crack length) fatigue cycles to investigate the effect of different crack lengths on micromechanisms governing crack propagation in the overload affected zone.

4.4.1. Tensile-Dominant Overload (ϕ_M = 14°)

Microscale fracture features of the specimen subjected to the overload mode-mixity of 14° (tensile-dominant) are shown in Figure 4.10 and Figure 4.11 for the two different crack lengths corresponding to 30,000 and 60,000 fatigue cycles respectively. Figure 4.10(a) shows a low magnification micrograph in the proximity of the overload at a shorter crack length (30,000 cycles) in which all the three investigated regions, i.e. pre-overload region, transient region, and post-overload region, can be seen. A typical overload line formed on the fracture surface is clearly visible, and it represents the curvature of the crack front at the time of the overload. For most of the specimen thickness, a flat crack front (marked with a straight line) which became curved near the specimen surface was observed. This behavior occurs primarily because of the presence of a higher value of crack opening *SIF* in the near-surface region during crack propagation, which leads to a higher degree of crack closure resulting in a reduced crack driving force [110]. It is also evident from the results in Figure 4.10(a) that the near-surface region (highlighted in red) is exposed to enhanced plastic deformation (crack closure). Furthermore, the existing roughness of the fracture surface is modified due to the repeated contact between crack flanks as premature closure of the crack tip causes an additional decrease in the value of effective *SIF* in the near-surface region [103]. Because of these phenomena, slightly curved crack fronts are

observed under tensile or tensile-dominant overloads, which has been widely reported in the literature [20,84,93,103,111]. High magnification SEM images were taken in region 'A1' (pre-overload) and region 'A2' (post-overload) of Figure 4.10(a), which are shown in Figure 4.10(b) and Figure 4.10(c) respectively. In both the micrographs, the fracture surface exhibits well-developed and fully-grown striations propagating on different ridges, in which the walls of adjacent ridges are well connected with the continuously growing striations. At the local scale, small misalignments in the direction of forward propagating striations were also observed. Such conditions arise due to the variations in the local stress and/or the microstructure leading to the change in the orientation of the fracture plane that subsequently results in altering the direction of striations [76]. The presence of unbroken second-phase particles and the widely dispersed microvoids were observed on the fracture surfaces suggesting a particle-matrix separation with very little plastic flow around the particles. The fracture surface also exhibits secondary cracks originating from the large voids. These were generated due to the interaction between forward propagating striations and hard particles. These fracture features are in agreement with the results presented in the literature [76,111] and indicate that the crack propagated in a stable mode I growth in both the pre-overload and the post- overload regions. A magnified SEM image in the transient region (on overload line and near the center) of Figure 4.10(a) is shown in Figure 4.10(d) that reveals a tortuous region (enclosed within a dashed line) extended over multiple small facets across the thickness, suggesting a brittle fracture during the loading cycle of the tensile-dominant overload. On higher magnification, a sharp physical boundary can be seen that impedes the crack propagation through the adjacent ridges as shown in

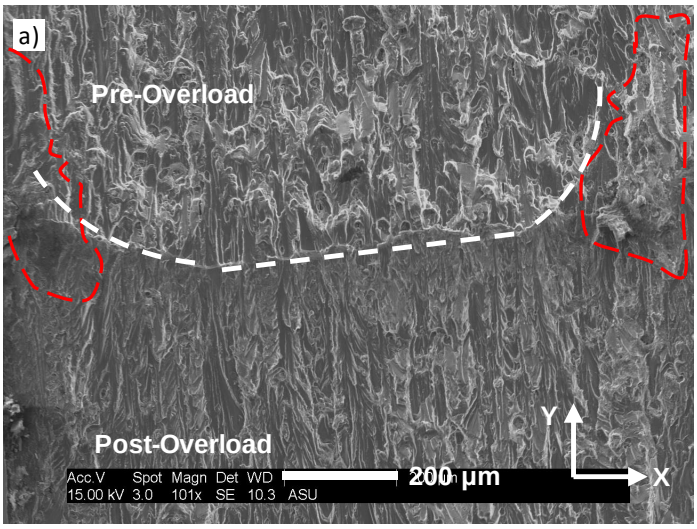
a)
Pre-Overload
Post-Overload
Y
X
Acc.V Spot Magn Det WD
15.00 kV 3.0 101x SE 10.3 ASU
200 µm

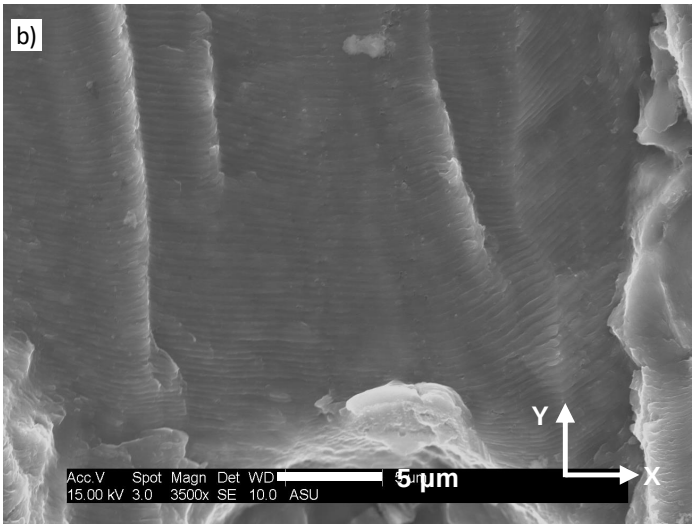
b)
Y
X
Acc.V Spot Magn Det WD
15.00 kV 3.0 3500x SE 10.0 ASU
5 µm

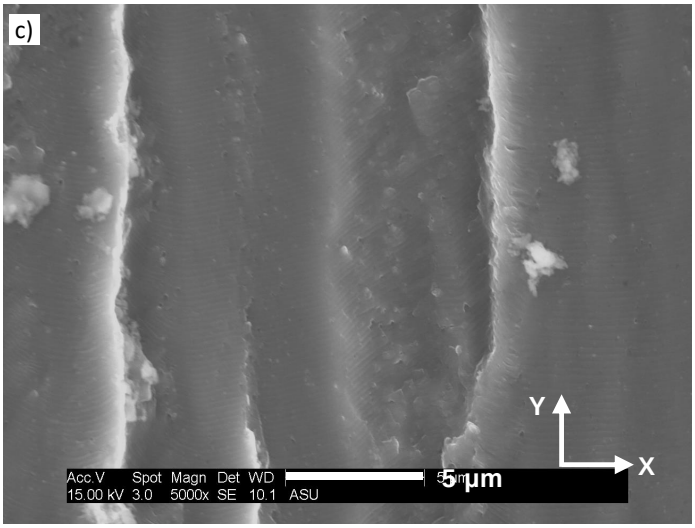
c)
Y
X
Acc.V Spot Magn Det WD
15.00 kV 3.0 5000x SE 10.1 ASU
5 µm

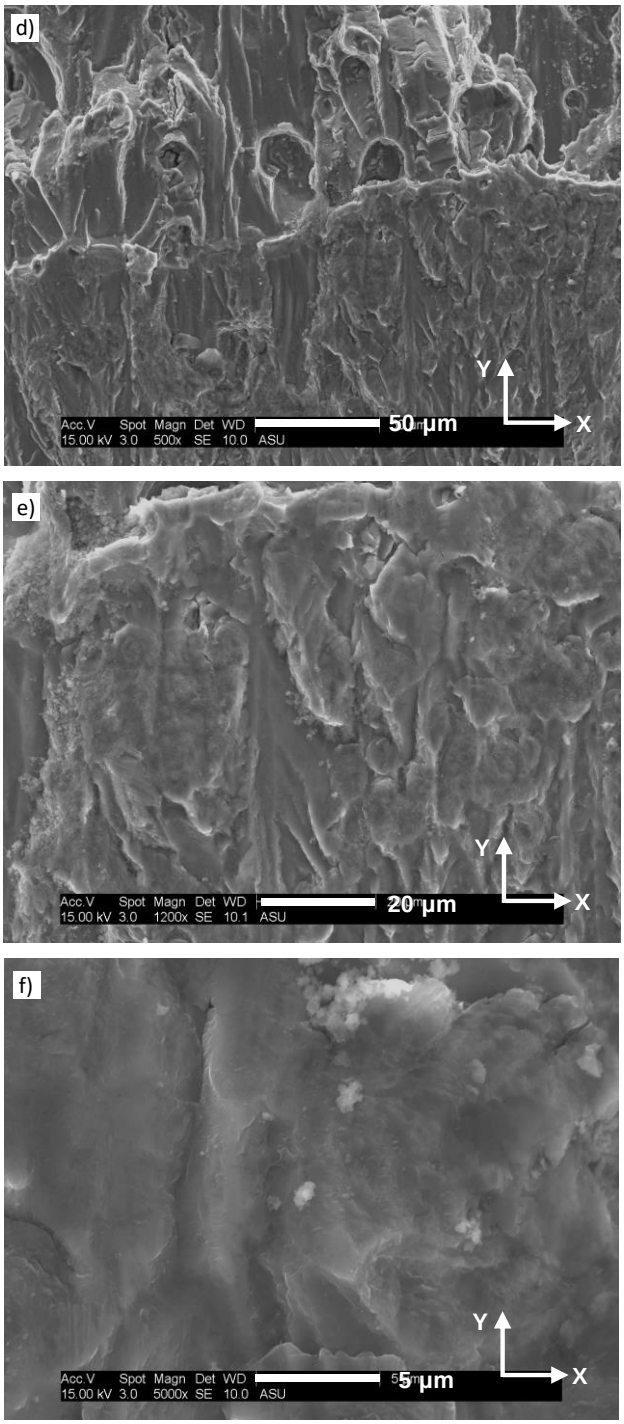

Figure 4.11: Microscale fracture features of the specimen subjected to tensile-dominant overload (ϕ_M = 14°) applied at 60k cycles: a) overload affected region (low magnification); b) pre-overload region; c) post-overload region. Magnified images of transient region showing: d) overload line with longer transient region; e) and f) featureless facets.

Figure 4.10(e). The ridges following the emerged boundary primarily consisted of two different features, which include: a) a smooth and featureless region shown in Figure 4.10(e); and b) annihilated striations shown in Figure 4.10(f). These features confirm the presence of a shear component in the loading and its influence on the crack governing micromechanism under a macroscopically tensile-dominant mix-mode overload. The sudden appearance of a boundary on a crack, propagating under the duplex slip mechanism, could possibly be the outcome of a very large dislocation generated on the slip plane corresponding to a very high load applied during the loading cycle of the overload.

Figure 4.11(a) shows the low magnification micrograph in the proximity of the overload at a longer crack length (60,000 cycles), which resembles all the fracture features observed at the shorter crack length shown in Figure 4.10(a). The same trait was displayed in the magnified SEM images taken in the pre-overload and the post-overload regions of Figure 4.11(a) as shown in Figure 4.11(b) and Figure 4.11(c) respectively. However, a slightly different trend was observed in the transient region (on overload line and near the center) of Figure 4.11(a) as compared with the transient region of Figure 4.10(a) and is shown in Figure 4.11(d). The transient region shown in Figure 4.11(d) is stretched over a longer distance and has more facets. This behavior is in accordance with the results presented for the recovery distance in the previous section, which indicated a larger transient zone for the same overload applied at the longer crack length. High magnification images of these facets are shown in Figure 4.11(e) and Figure 4.11(f) that suggest a higher degree of brittle failure at longer crack length during the applied overload. This behavior is anticipated

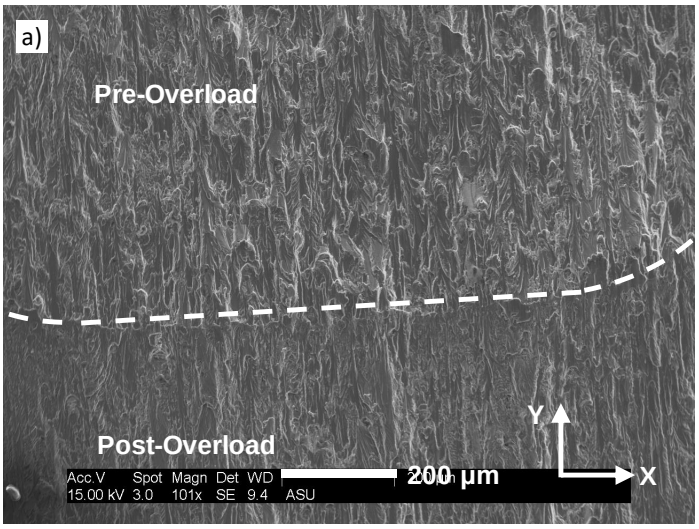
a)
Pre-Overload
Post-Overload
Acc.V Spot Magn Det WD
15.00 kV 3.0 101x SE 9.4 ASU
200 µm
Y
X

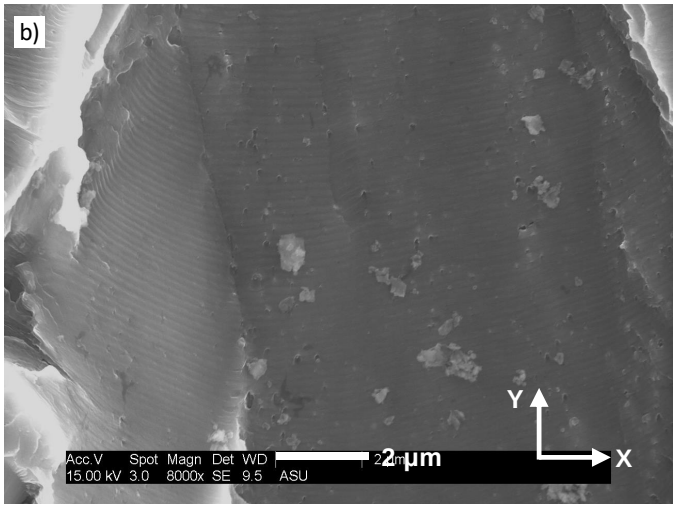
b)
Acc.V Spot Magn Det WD
15.00 kV 3.0 8000x SE 9.5 ASU
2 µm
Y
X

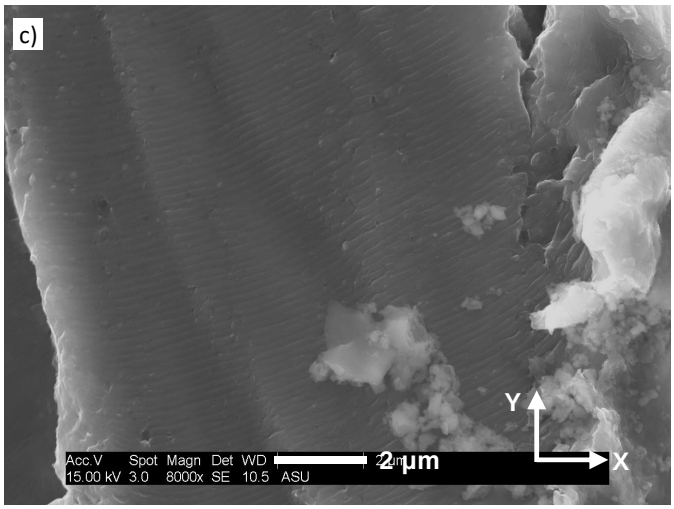
c)
Acc.V Spot Magn Det WD
15.00 kV 3.0 8000x SE 10.5 ASU
2 µm
Y
X

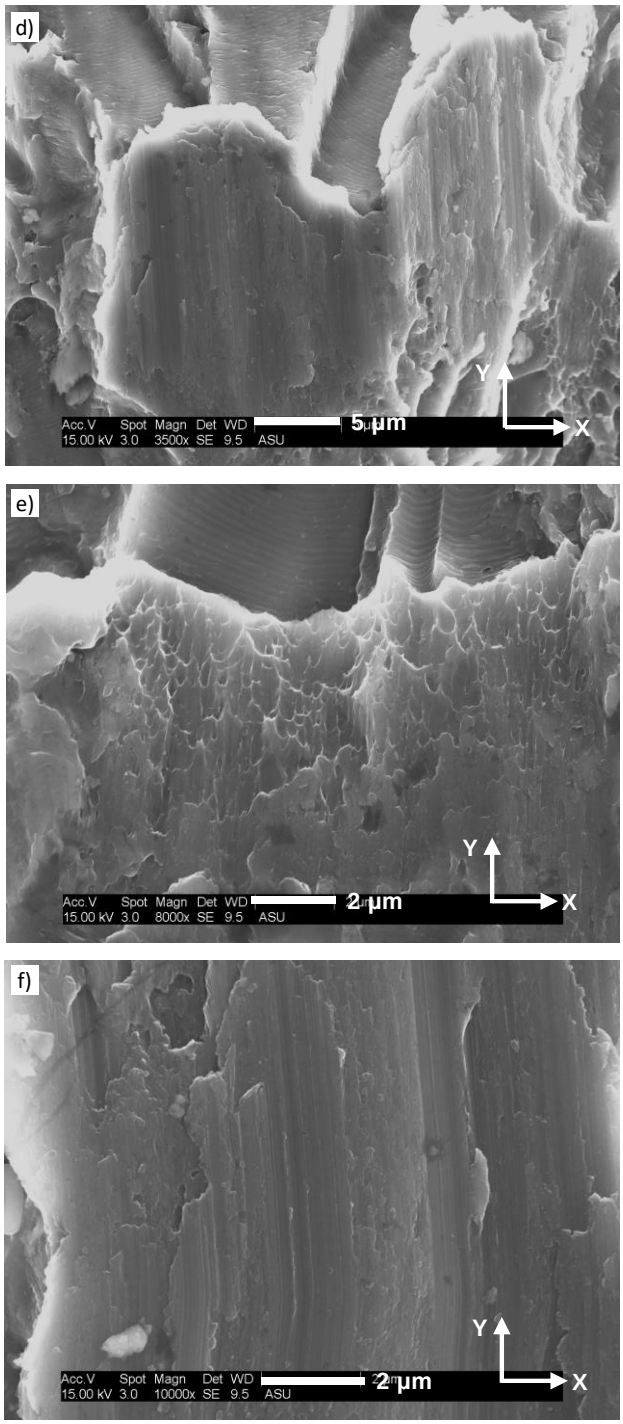

Figure 4.12: Microscale fracture features of the specimen subjected to shear-dominant overload (ϕ_M = 56.3°) applied at 30k cycles: a) overload affected region (low magnification); b) pre-overload region; c) post-overload region. Magnified images of transient region showing: d) abrupt change in fracture features, cleavage steps; e) elongated dimples; f) tongues and tire-tracks.

because the degree of brittleness increases with an increase in the magnitude of the crack driving force, which is higher at longer crack length for the same loading condition [76].

4.4.2. Shear-Dominant Overload (ϕ_M = 56.3°)

To understand the effect of mode-mixity on the governing micromechanism, SEM images at various magnification were also taken on the fracture surface of the specimen subjected to the overload mode-mixity of 56.3° (shear-dominant), which are shown in Figure 4.12 and Figure 4.13. The low magnification image, in the proximity of the overload, corresponding to the shorter crack length (30,000 cycles) is shown in Figure 4.12(a). Unlike the case of tensile-dominant overload, the overload line is barely visible, and the facets are stretched over a "narrow-region" of smooth surface. The appearance of a smooth surface indicates that the facets were formed by an extensive tearing along glide planes in a transgranular fracture [111]. The micrograph also reveals the presence of a flat crack front indicating a uniform crack driving force across the thickness of the specimen. This, in turn, negates any presence of additional crack closure in the near-surface region, which is also evident from the absence of enhanced plastic deformation on the fracture surface (earlier shown in tensile-dominant overload) in the near-surface region as shown in Figure 4.12(a). Figure 4.12(b) and Figure 4.12(c) show high magnification SEM images of the pre-overload and the post-overload regions, which display the same fracture features obtained during tensile-dominant overloads. This confirms the consistency in the loading pattern and the repeatability of the outcome as the loading conditions for the pre-overload and the post-overload regions remained the same and differed only in the transient region due to the overload of different mode-mixity. Examination of the transient region at higher

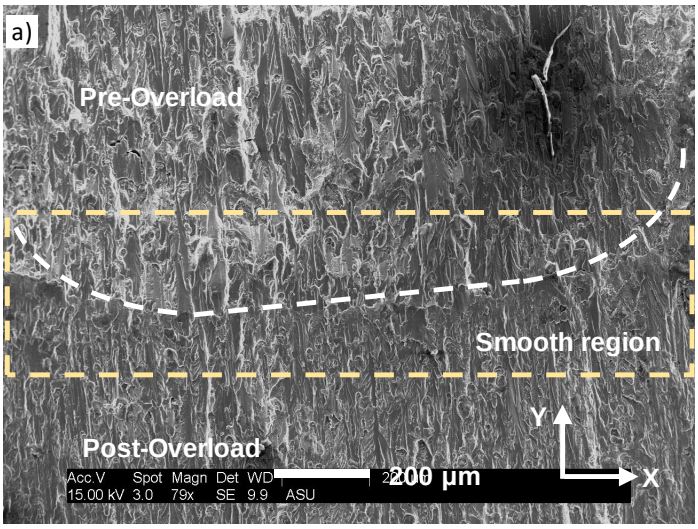
a)
Pre-Overload
Smooth region
Post-Overload
Y
X
Acc.V Spot Magn Det WD
15.00 kV 3.0 79x SE 9.9 ASU
200 µm

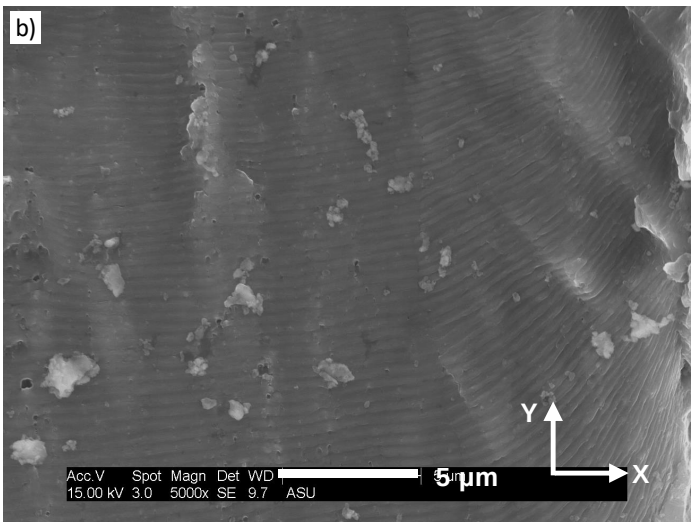
b)
Y
X
Acc.V Spot Magn Det WD
15.00 kV 3.0 5000x SE 9.7 ASU
5 µm

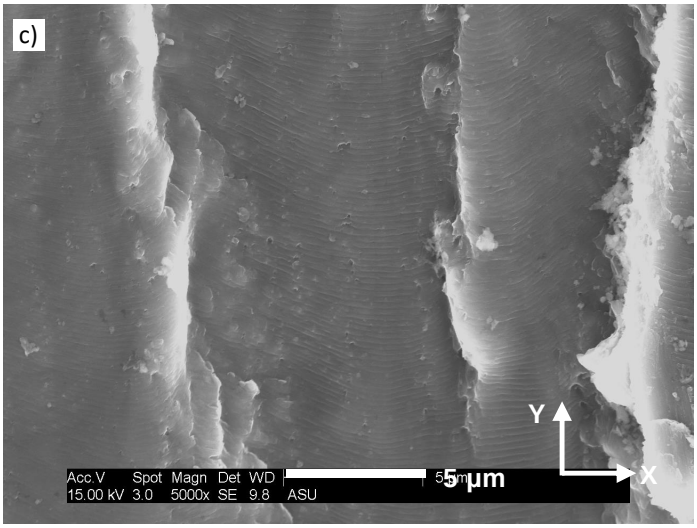
c)
Y
X
Acc.V Spot Magn Det WD
15.00 kV 3.0 5000x SE 9.8 ASU
5 µm

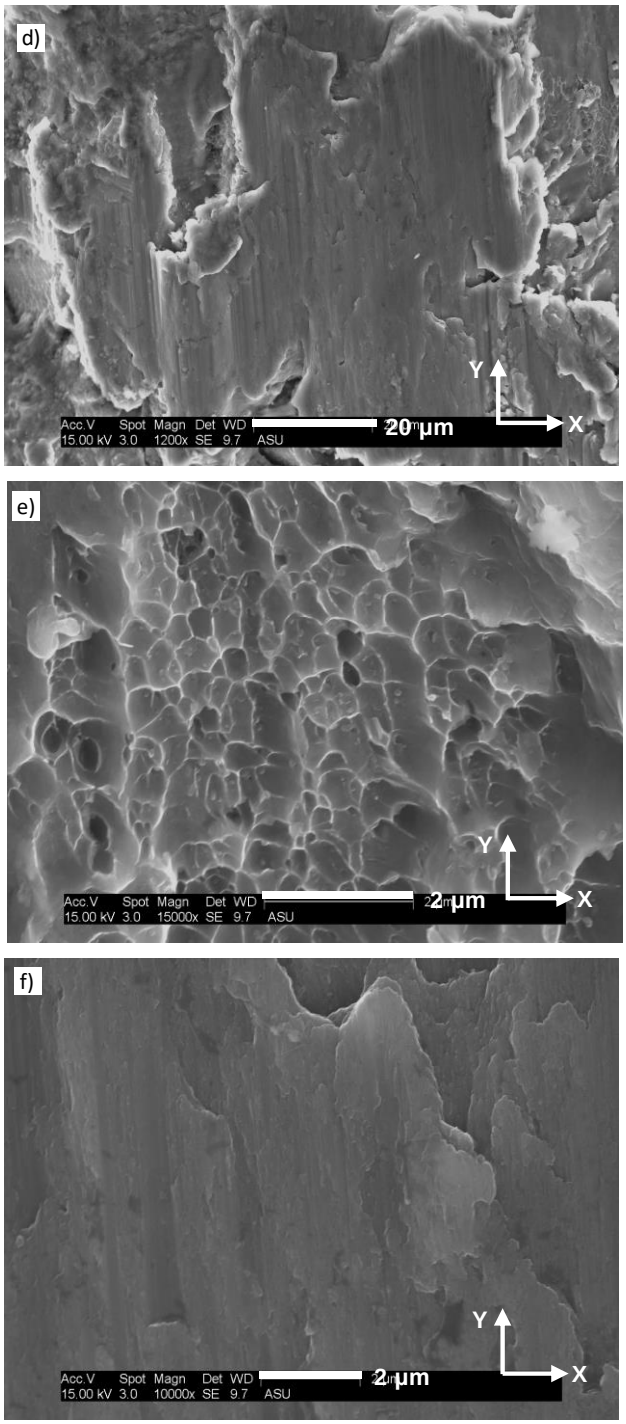

Figure 4.13: Microscale fracture features of the specimen subjected to shear-dominant overload (ϕ_M = 56.3°) applied at 60k cycles: a) overload affected region (low magnification); b) pre-overload region; c) post-overload region. Magnified images of transient region showing: d) cleavage steps; e) elongated dimples; f) tongues and tire-tracks.

magnification reveals an abrupt change in fracture features from well-developed striations to smooth cleavage steps and elongated dimples, across the thickness of the specimen, separating the pre-overload region from the overload affected region, as shown in Figure 4.12(d) and Figure 4.12(e). While the presence of dimples indicates a ductile failure in a fast fracture mode, its elongated shape suggests that the failure occurred predominantly under shear loading. This observation is in contrast with the result presented earlier for the tensile-dominant overload, where the fracture surface did not show any evidence of fast fracture (dimple rupture). In addition to elongated dimples, the fracture surface also exhibits tongues and tire-tracks as shown in Figure 4.12(f), which are the typical characteristics of shear or shear-dominant failure. These results are consistent with the findings of other investigations made under shear overloads, either in a uniaxial loading [111] or in a biaxial loading [23].

In order to evaluate the effect of crack length on the transient region, microscale analysis similar to that of the shorter crack length (30,000 cycles) was conducted at the longer crack length (60,000 cycles), for which the corresponding micrographs are shown in Figure 4.13. By comparing Figure 4.13 (a) with Figure 4.12(a), it is evident that: (1) the overload line was nearly annihilated; (2) a larger region of the smooth surface was generated; (3) a curved crack front was obtained suggesting the presence of additional crack closure in the near-surface region; (4) enhanced plastic deformation was found near the surface confirming the crack closure, which in turn supports the idea that the existence of crack closure is dependent on crack length (or *SIF*). As expected, pre-overload (Figure 4.13(b)) and post-overload (Figure 4.13(c)) region did not show any change in the fracture features

with respect to the crack length because of the identical pre- and post-overload loading conditions. Typical features of shear-dominant fracture were observed in the magnified images of the transient region, including smooth cleavage steps (Figure 4.13(d)), elongated dimples (Figure 4.13(e)), and tire-tracks and tongues (Figure 4.13(f)). The same features were also observed in the case of shorter crack length, except larger dimples and a longer region of the smooth surface were observed at the longer crack length.

4.5. Conclusion

Cruciform specimens were used to investigate the effects of overload mode-mixity on crack growth behavior and governing micromechanisms of AA 7075 T6 in an otherwise constant amplitude biaxial fatigue loading. The presented results support the following observations:

- For all the values of overload mode-mixity, fatigue life of the specimen was increased, and the minimum increase occurred for the overload mode-mixity of 45°. Also, the initial acceleration in crack growth was observed for the shear-dominant overloads, but the crack retardation behavior was observed for all the cases of mode-mixity.
- At shorter crack length (30,000 cycles), R_d was found to increase with increasing value of mode-mixity, but at longer crack length (60,000 cycles), only the shear dominant loading showed an increase in R_d with increasing value of mode-mixity.
- The fracture surface of the tensile-dominant overload showed an overload line, which on higher magnification showed smooth and featureless facets along with annihilated striations. On the other hand, the fracture surface of the shear-dominant overload showed a narrow-region of smooth surface, which on higher magnification showed

features of shear fracture including the annihilated striations, tire tracks, cleavage steps, tongues, and the elongated dimples in the transient region.

5. EMPIRICAL MODEL FOR PREDICTING FATIGUE CRACK GROWTH RATE IN TRANSIENT REGION

5.1. Introduction

Most of the engineering structures and materials experience variable amplitude loading during their service lives. The presence of load fluctuations or random amplitude loading induces load-interaction effects that can significantly affect fatigue crack growth rate and subsequently fatigue life of the engineering structures [112]. One of the most important load-interaction effects is produced by a single overload cycle introduced in a constant amplitude (CA) fatigue loading. Therefore, it is important to develop a quantitative model that can effectively incorporate such load-interaction effects.

It is a well-known fact that the overload results in crack growth retardation and the degree of retardation is proportional to the magnitude of applied overload. This phenomenon is often explained by the compressive residual stresses resulting from the plastic deformation that is introduced ahead of the crack tip due to the application of the overload. Based on this approach, many models have been developed to describe the crack growth retardation after the applied overload [113–119]. Among them, the earliest models were developed by Wheeler [113] and Willenborg [119], which are still widely used. The Wheeler model [113] predicts overload crack growth rate (CGR) by simply modifying the constant amplitude CGR with the help of a retardation parameter. The value of retardation parameter is experimentally determined and is expressed as a function of the ratio of the current plastic zone size to the overload plastic zone size. Several modifications of the Wheeler model have been proposed [120–122]. Yuen *et al* [120] introduced additional

parameters to the original Wheeler model to account for the initial CGR acceleration, delay retardation and overload interaction. Mehrzadi *et al*. [121] modified the Wheeler model by including parameters to account for material's sensitivity to overload in order to predict the CGR. Huang *et al*.[122] modeled plastic zone size ahead of the crack tip as a continuous function of the parameters defining the constraint state around the crack tip and was able to predict crack retardation and crack arrest due to the overload. On the other hand, the Willenborg model [119] used the material yield stress to give the plastic zone size instead of using it to find the empirical parameters. The model calculates degree of retardation as a function of stress intensity factor necessary to balance the effect of the overload plastic zone. Similar to the Wheeler model, Kim and Shim [123] developed an empirical model by introducing a retardation coefficient, which was defined as the ratio of the experimentally determined retarded CGR to the constant amplitude CGR. The model developed by Pavlou *et al*. [124] also used a retardation factor to modify the constant amplitude CGR. It defined the retardation factor as a function of the changing yield stress due to strain hardening within the overload plastic zone and used it to determine the overload affected fatigue CGR.

Because of the complexity associated with the mechanisms underlying the variable amplitude fatigue, the retardation models presented above can be justified only for the mode I overload. With the increase in mode II component of the overload, plastic zone is rotated, and its size becomes larger along the crack line while the plastic deformations in the vertical direction decreases resulting in a decrease of compressive residual stresses around the crack tip. In the case of pure mode II overload, the plastic deformations in the

vertical direction becomes insignificant resulting in an insignificant effect of compressive residual stresses in controlling the crack retardation behavior [125,126]. In addition to the lack of proper understanding of the retardation mechanisms, large ambiguities and disagreements can be seen among various models available in the literature. Therefore, no fundamental or universally accepted model is available till date that can be used to predict overload affected crack growth rate. In the present study, an empirical model is developed to predict the crack growth rate trend under pure mode II overloads in an otherwise CA biaxial fatigue loading. The proposed model is based on the shape and the size of the plastic zone ahead of the crack tip, and the degree of material hardening within the overload plastic zone region in order to predict the crack growth rate.

5.2. Experimental Observation

The experiments were conducted using the MTS planar biaxial/torsional load frame, using cruciform specimens. These specimens were subjected to single overload excursions in an otherwise CA biaxial fatigue loading with P_{max} (maximum cyclic load) = 15 kN, R (stress ratio) = 0.1 and a frequency of 10 Hz, as shown in Figure 3.7. The load excursions were applied at macroscopically smaller crack length (a_{OL} = 2-4 mm) and the tests were conducted at different values of shear overload ratio, i.e. R_{OL} = ($R_{OL\text{-}X}$, $R_{OL\text{-}Y}$) = (1, -1), (1.5, -1.5), (1.75, -1.75), (2, -2), and (2.5, -2.5); where $R_{OL\text{-}X}$ = Overload ratio in X-axis, and $R_{OL\text{-}Y}$ = Overload ratio in Y-axis. Additional tests were conducted at ($R_{OL\text{-}X}$, $R_{OL\text{-}Y}$) = (2.25, -2.25) that were further used to validate the developed empirical model.

The experimental observations for CGR in the transient region (overload affected region) were analyzed in terms of acceleration ratio, retardation ratio, and the asymptotic recovery

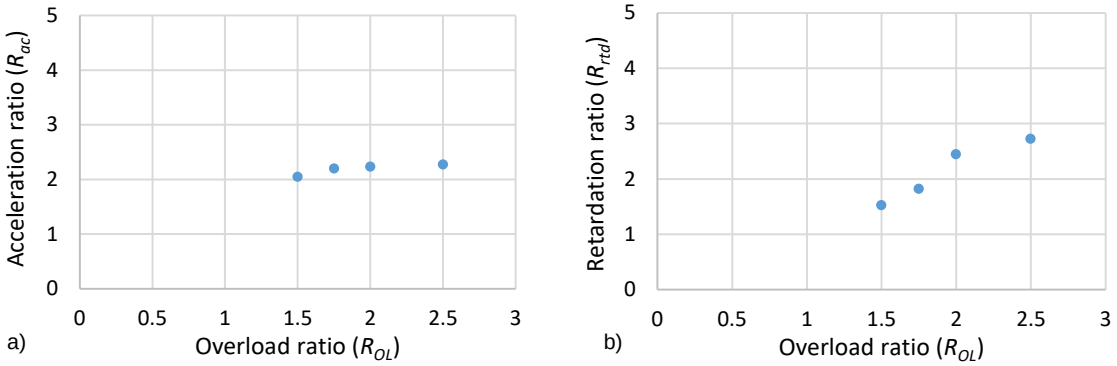

Figure 5.1: Experimentally determined values of a) accelration ratio, and b) retardation ratio at different values R_{OL}.

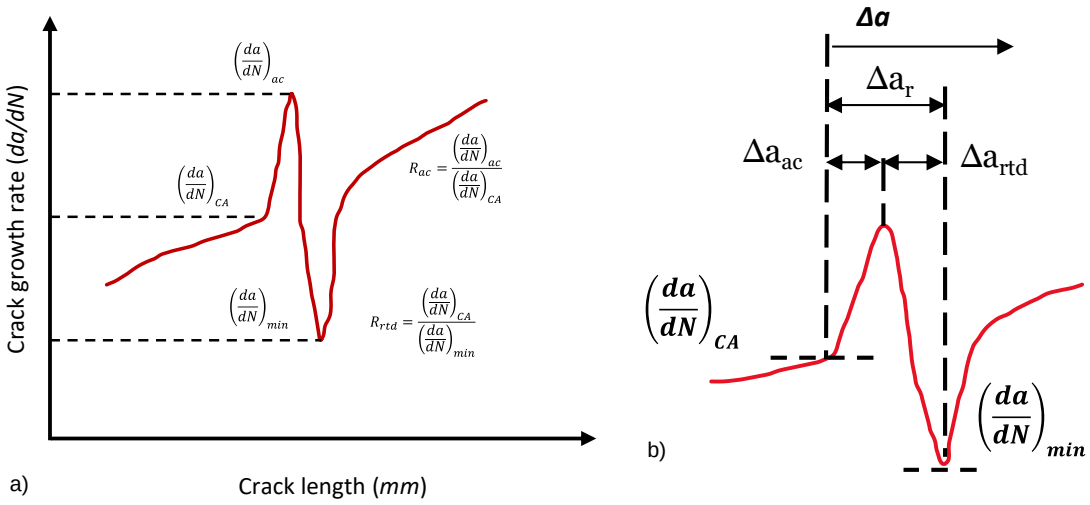

Figure 5.2: a) and b) are the schematics of CGR against crack length.

as summarized in Table 5.1 and shown in Figure 5.1. Figure 5.1(a) shows the plot of acceleration ratio (R_{ac}), which is defined as the ratio of CGR at the time of initial acceleration to the constant amplitude CGR before the overload, against the applied overload ratio. It was found that the magnitude of R_{ac} did not show any significant change with the increase in the values of overload ratios ($R_{OL} = R_{OL\text{-}X}, R_{OL\text{-}Y}$). However, a different trend was observed with retardation ratio (R_{rtd}), which is defined as the ratio of constant amplitude CGR before the overload to the minimum CGR due to retardation, when plotted

Table 5.1:

Experimental data used in model development.

R_{OL}	a_{OL} (*mm*)	Initial CGR (*mm/cycle*)	R_{ac}	R_{rtd}	Δa_{ac} (*mm*)	Δa_{rtd} (*mm*)	Δa_r (*mm*)
1.5	2.51	1.44×10^{-4}	2.06	1.52	0.195	0.222	0.417
1.75	2.58	1.97×10^{-4}	2.20	1.82	0.236	0.26	0.496
2	2.43	1.88×10^{-4}	2.23	2.44	0.311	0.442	0.753
2.5	2.43	1.84×10^{-4}	2.28	2.72	0.363	0.441	0.804

against the values of R_{OL} and is shown in Figure 5.1(b). Unlike acceleration ratio, an increase in the magnitude of retardation ratio was observed with an increase in the value of overload ratio. Once the CGR reached the minimum value, a sharp increase in its magnitude was observed, which was followed by an asymptotic increase till the time crack propagated in the overload affected region. As shown in Figure 5.2(a), the increase in CGR during recovery phase was found to follow inverse hyperbolic function. Figure 5.2(b) explains the different variables used to define the crack lengths in the transient region, where Δa_{ac} = length of accelerated CGR from overload position, Δa_{rtd} = length of retarded CGR from accelerated CGR position, Δa_r = sum of the lengths of Δa_{ac} and Δa_{rtd}, $\left(\frac{da}{dN}\right)_{CA}$ = CGR before overload, $\left(\frac{da}{dN}\right)_{ac}$ = CGR during overload, $\left(\frac{da}{dN}\right)_{min}$ = maximum retardation in CGR. The proposed empirical model in subsequent sections takes into consideration of these observed phenomenon and correlates them with strain hardening, and the plastic zone size ahead of the crack tip.

5.3. Model Formulation

5.3.1. Plastic Zone

The theory of elasticity predicts an infinitely large stress at the tip of the crack when a body with a sharp crack is loaded [120]. In other words, for ductile materials, this means that the crack tip stresses exceed the yield stress of the material and a zone of plastically deformed region is formed ahead of the crack tip. The amount of the plastic deformation is restricted by the surrounding material, which remains elastic during the loading period while its size is determined by the stress conditions of the body. In a thin specimen, there is insignificant variation in stress across the thickness and is considered to be under plane stress conditions, whereas, in a thicker specimen, material is constrained across the thickness resulting in stress variations and is considered to be under plane strain conditions. The proposed model is under plain stress condition for which plastic zone size under mode I loading is calculated using Irwin's method as shown in Eq. (1). During subsequent unloading, reversed yielding occurs and a zone of compressive residual stress is created ahead of the crack tip and the size of reversed yield zone is one-fourth of the maximum plastic zone size at the time of loading.

$$PZS\ I = \frac{1}{\pi}\left(\frac{K_I}{\sigma_y}\right)^2 \tag{1}$$

where $PZS\ I$ = plastic zone size under mode I loading, K_I = stress intensity factor under mode I loading, σ_y = yield stress of the material. The plastic zone size under mode II loading in its generic form is shown in Eq. (2). The stretch of plastic zone along the crack line can be found using Eq. (3), obtained from Eq. (2) when the value of 'θ' is 0. At the same

Table 5.2:

Analytical data used in model development.

R_{OL}	a_{OL} (mm)	ΔK_I (Mpa.√m)	K_{II_OL} (Mpa.√m)	PZS I (mm)	R_{OL} x PZS I (mm)	PZS II (mm)	σ_y' (MPa)	$\frac{\sigma_y'}{\sigma_y}$
1.5	2.51	11.12	21.95	0.192	0.288	0.91	528	1.05
1.75	2.58	11.16	25.79	0.193	0.339	1.26	538	1.07
2	2.43	11.0	29.02	0.188	0.376	1.59	547	1.09
2.5	2.43	11.10	36.28	0.191	0.478	2.48	572	1.14

amplitude of far-field loading, the plastic zone size in mode II can be up to five times bigger than that in mode I [1].

$$r^{II}(\theta) = \frac{1}{8\pi}\left(\frac{K_{II}}{\sigma_y}\right)^2 \times (14 - 2\cos\theta - 9\sin^2\theta) \quad (2)$$

$$PZS\ II = r^{II}(0) = \frac{3}{2\pi}\left(\frac{K_{II}}{\sigma_y}\right)^2 \quad (3)$$

where, r^{II} is plastic zone size in θ direction, *PZS II* = plastic zone size in crack direction under mode II loading, K_{II} = mode II stress intensity factor. The plastic zone size obtained under various loading conditions are summarized in Table 5.2, where ΔK_I = cyclic stress intensity factor under mode I loading, K_{II_OL} = mode II stress intensity factor at overload.

5.3.2. Proposed Model

The proposed empirical model predicts the CGR, *da/dN*, in the transient region created by the shear (mode II) overloads in an otherwise constant amplitude biaxial loading. The model introduces experimentally determined parameters to calculate overload affected

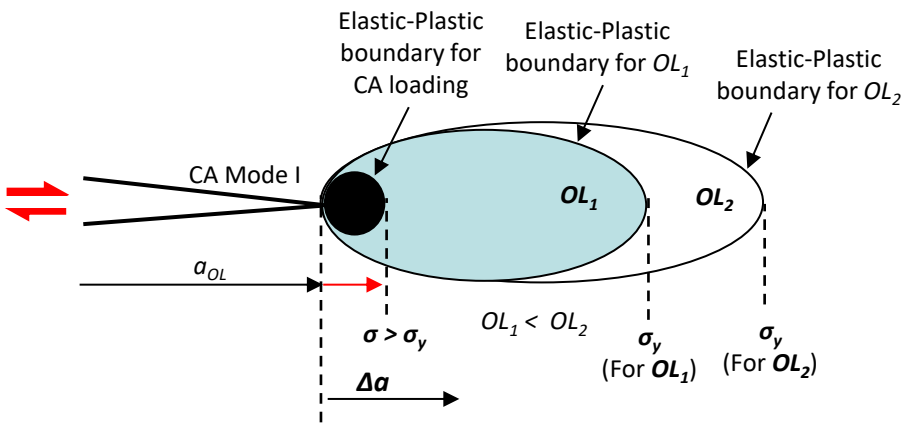

Figure 5.3: Schematic of the plastic zone showing its shape and size under different loading scenarios.

da/dN in terms of constant amplitude *da/dN*. The parameters can further be related with the shape and the size of the plastic zone ahead of the crack tip, and the degree of material hardening within the overload plastic zone as shown in Figure 5.3. The model in its generic form is presented in Eq. (4), where C_p is the set of parameters determined experimentally and is multiplied with the constant amplitude CGR. The parameter C_p is sub-divided into three different parameters (C_{p1}, C_{p2}, C_{p3}) to uniquely identify accelerated CGR at overload, delayed retardation in CGR following the overload, and gradual recovery after reaching minimum CGR.

$$\frac{da}{dN} = C_p \times \left(\frac{da}{dN}\right)_{CA} \qquad C_p = \begin{cases} C_{P1} & \Delta a = \Delta a_{ac} \\ C_{P2} & \Delta a = \Delta a_r \\ C_{P3} & \Delta a > \Delta a_r \end{cases} \tag{4}$$

Accelerated CGR

In many cases, it has been observed that an initial acceleration of the fatigue CGR occurs immediately after an overload is applied, which is then followed by crack retardation. Despite that the majority of fatigue models have neglected the crack acceleration effect and

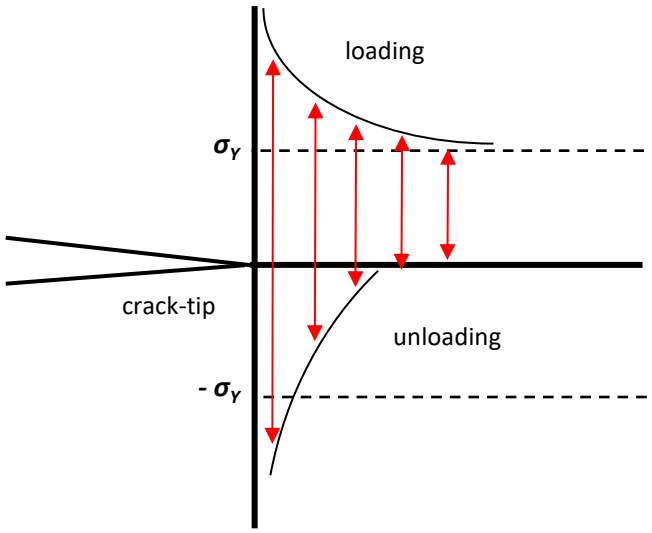

Figure 5.4: Stress varitions near the crack-tip (within the CA plastic zone region) during loading and unloading cycles.

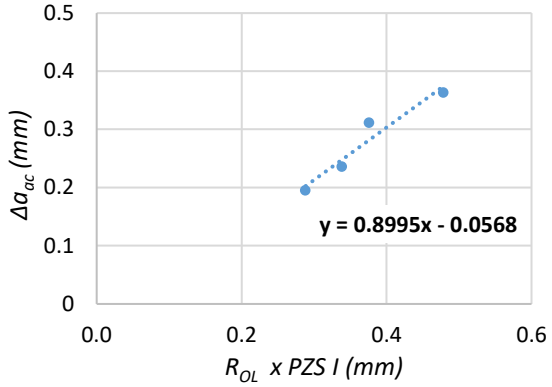

Figure 5.5: Plot of accelerated CGR against the product of overload ratio and plastic zone size of CA loading.

captured only the dominating crack retardation effects. In the proposed model, the effect of accelerated CGR has been taken into account by introducing an additional parameter, C_{P1}, that can be corelated with the plastic deformation ahead of the crack tip during CA fatigue loading. Within the plastic zone (CA loading), a very high stress gradient occurs in the region between the crack tip and the elastic-plastic boundary along the crack line at the

time of loading as well as unloading cycles as shown in Figure 5.4. Even for a positive stress ratio (R>0), the elements near crack-tip undergoes a very high tensile stress ($\sigma > \sigma_y$) during the loading cycle, which is followed by a very high compressive stress ($\sigma < -\sigma_y$) during unloading cycle. The amplitudes of the cyclic stress keep on decreasing as we move away from the crack-tip and beyond a certain distance in the plastic zone region the compressive stress vanishes for the unloading cycle. This results in the consistent accumulation of damage in the plastic zone region of the CA loading, which leads to material deterioration and weakening. Under such conditions when a shear overload is applied at a macroscopically small crack length, it easily cuts through the plastic zone region of the CA loading giving similar values of the acceleration ratio for all the values of overload ratios (R_{OL}). The experimental values of acceleration ratio at different overload ratios are shown in Table 5.1, from which the average value of R_{ac} is found to be 2.2. This gives the following relation:

$$R_{ac} = \frac{\left(\frac{da}{dN}\right)_{ac}}{\left(\frac{da}{dN}\right)_{CA}} = 2.2 \tag{5}$$

$$\left(\frac{da}{dN}\right)_{ac} = 2.2 \times \left(\frac{da}{dN}\right)_{CA} \qquad \text{where, } C_{P1} = 2.2 \tag{6}$$

As shown in Table 5.1, the experimentally observed values for the location of maximum accelerated CGR, Δa_{ac}, is found to be proportional to the applied R_{OL}. Therefore, the values of Δa_{ac} was plotted against the product of R_{OL} and $PZS\ I$ in order to get the regression curve. From the plot shown in Figure 5.5, following relation was obtained:

$$\Delta a_{ac} = 0.8995 \times (R_{OL} \times PZS\ I) - 0.0568 \tag{7}$$

Crack Retardation

In this model, the crack retardation effect has been taken into account by introducing a retardation parameter, C_{P2}, that can be corelated with the plastic deformation and the strain hardening resulting from the applied mode II (shear) overload. Since all the overloads cut through the weak and deteriorated plastic zone of CA loading, different degrees of hardening occur at the elastic-plastic boundary of CA loading resulting in different values of yield stress at different overload ratios. However, the yield stress at the elastic–plastic boundary of the overload plastic zone remains equal to the initial yield stress of the material. The proposed model captures the degree of strain hardening between the elastic-plastic boundary of CA loading and the elastic-plastic boundaries of the overload plastic zone, which is then used to present retardation parameter as a function of the changing yield stress. While developing the model two assumptions have been made as shown in Figure 5.6: i) maximum hardening occurs at R_{OL} of 2.5, for which yield stress near the elastic-plastic boundary of CA loading becomes equal to ultimate stress (σ_u); ii) slope (m) of the

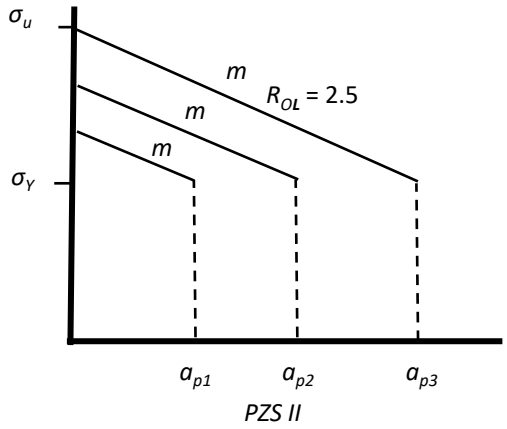

Figure 5.6: Scematic for modified yield stress at elastic-plastic boundary of CA loading against the size of plastic zone created due to mode II overload.

curve between the new yield stress (σ_y') and the overload plastic zone size (a_p) remains constant for all the values of overload ratio.

$$m = \frac{\sigma_u - \sigma_y}{PZS\ II_{(R_{OL}=2.5)}} = \frac{(572-503)\times 10^6}{2.48 \times 10^{-3}} = 2.78 \times 10^{10} \quad (8)$$

$$Also, m = \frac{\sigma_y' - \sigma_y}{PZS\ II} \quad (9)$$

$$\sigma_y' = \sigma_y + m \times PZS\ II \quad (10)$$

The values of σ_y' obtained from Eq. (10) and the normalized value of σ_y' with respect to σ_y, i.e. yield ratio, are shown in Table 5.2, whereas, the experimental values of crack

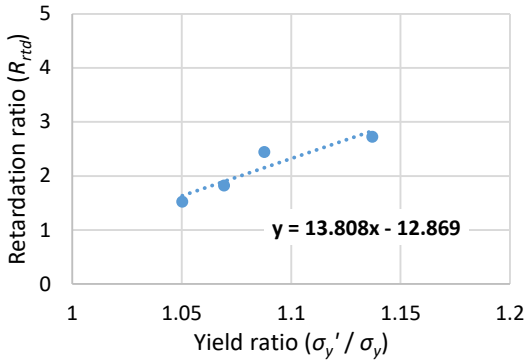

Figure 5.7: Plot of retardation ratio against yield ratio.

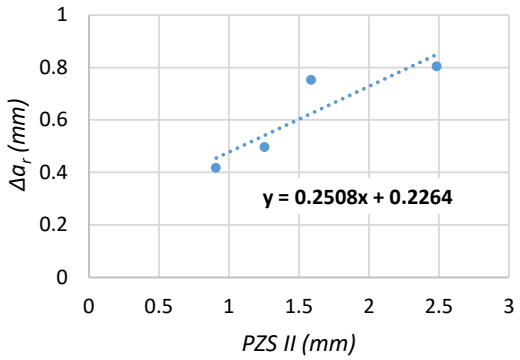

Figure 5.8: Plot showing distance of maximum CGR retardation from the overload location against the size of plastic zone created under mode II overload.

retardation ratio (R_{rtd}) is shown in Table 5.1. In order to find the values of maximum retardation, regression curve was obtained from the plot of normalized σ_y' with R_{rtd} as shown in Figure 5.7. From the plot shown in Figure 5.7, following relation was obtained:

$$y = 13.808x - 12.869 \tag{11}$$

$$R_{rtd} = 13.808 \times \frac{\sigma_y'}{\sigma_y} - 12.869 \tag{12}$$

$$\frac{\left(\frac{da}{dN}\right)_{CA}}{\left(\frac{da}{dN}\right)_{min}} = 13.808 \times \frac{\sigma_y'}{\sigma_y} - 12.869 \tag{13}$$

By substituting the expression of σ_y' from Eq. (10)

$$\left(\frac{da}{dN}\right)_{min} = \frac{1}{13.808 \times \left(1 + \frac{m \times PZS\ II}{\sigma_y}\right) - 12.869} \times \left(\frac{da}{dN}\right)_{CA} \tag{14}$$

where, the retardation parameter, $C_{P2} = \frac{1}{13.808 \times \left(1 + \frac{m \times PZS\ II}{\sigma_y}\right) - 12.869}$

The experimentally observed values for the location of maximum retardation in CGR, Δa_r, is shown in Table 5.1, and the values of overload *PZS II* for different values of R_{OL} is shown in Table 5.2. Using these two sets of data, regression curve was obtained from their plot as shown in Figure 5.8, which gives the following relation:

$$\Delta a_r = 0.2508 \times PZS\ II - 0.2264 \tag{15}$$

CGR Recovery

The model uses inverse hyperbolic function as a recovery parameter, C_{P3}, to predict the asymptotic recovery in CGR from its minimum value reached during crack retardation.

The recovery parameter is expressed in terms of a) crack length advancement from the overload location (Δa); and b) the retardation distance (Δa_r). To determine the value of recovery parameter at a given crack length ($\Delta a > \Delta a_r$), the model takes the ratio of Δa to Δa_r as the input value and calculates the crack growth rate as shown in Eq. (16).

$$\frac{da}{dN} = \left(\frac{da}{dN}\right)_{min} + C_r \times ln\left(\left(\frac{\Delta a}{\Delta a_r}\right) + \sqrt{\left(\frac{\Delta a}{\Delta a_r}\right)^2 - 1}\right) \times \left(\frac{da}{dN}\right)_{CA} \quad (16)$$

By substituting the values of $\left(\frac{da}{dN}\right)_{min}$ from Eq. (14)

$$\frac{da}{dN} = \left(\frac{1}{13.808 \times \left(1 + \frac{m \times PZS\ II}{\sigma_y}\right) - 12.869} + C_r \times ln\left(\left(\frac{\Delta a}{\Delta a_r}\right) + \sqrt{\left(\frac{\Delta a}{\Delta a_r}\right)^2 - 1}\right)\right) \times \left(\frac{da}{dN}\right)_{CA} \quad (17)$$

where, $C_{P3} = \left(\frac{1}{13.808 \times \left(1 + \frac{m \times PZS\ II}{\sigma_y}\right) - 12.869} + C_r \times ln\left(\left(\frac{\Delta a}{\Delta a_r}\right) + \sqrt{\left(\frac{\Delta a}{\Delta a_r}\right)^2 - 1}\right)\right)$

and C_r is a shaping constant whose value

5.4. Model Validation

The parameters of the proposed empirical model have been calibrated using the experimental results obtained from the overload ratios of (1.5, -1.5), (1.75, -1.75), (2, -2), and (2.5, -2.5). However, validation of the model is done with the help of the experimental data for the overload ratio of (2.25, -2.25). The predicted values of accelerated CGR and their locations have been plotted against the overload ratios in Figure 5.9, in which experimental values are also provided for the comparison. Similarly, predicted values of maximum retardation in CGR and their locations are plotted against the overload ratios and

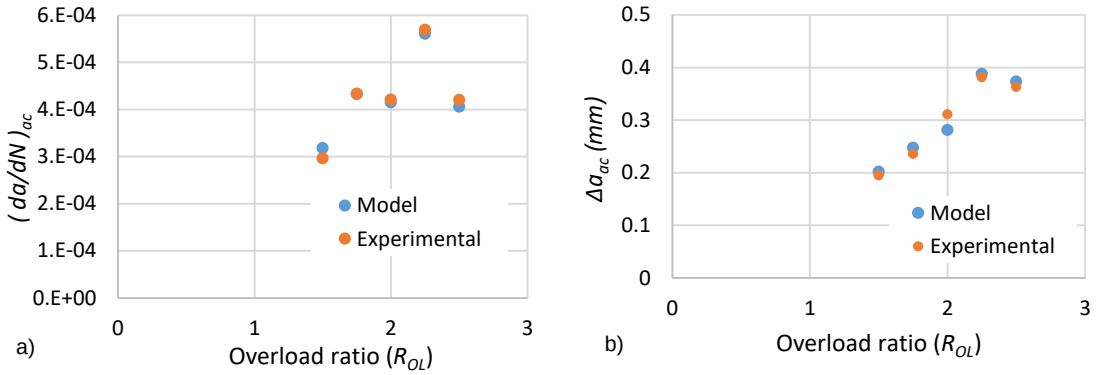

Figure 5.9: Comparison of experimental and model predicted values of a) maximum initial acceleration, and b) its location for different overload ratio.

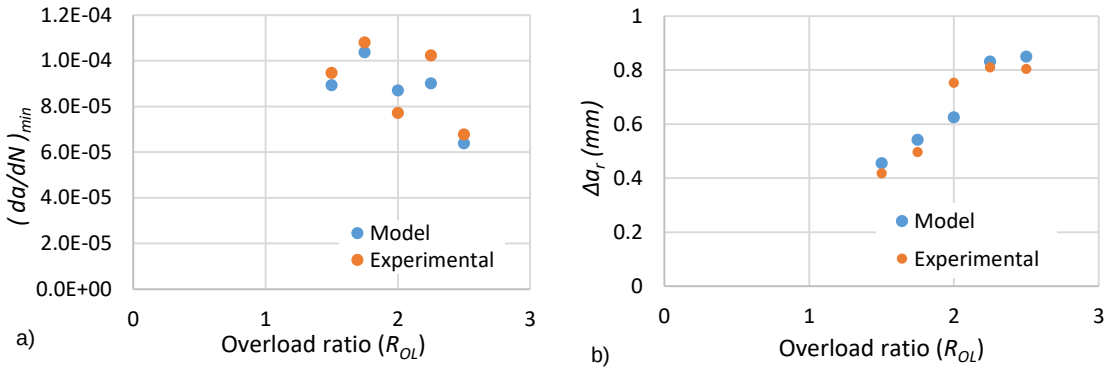

Figure 5.10: Comparison of experimental and model predicted values of a) maximum CGR retardation, and b) its location for different overload ratio.

are shown in Figure 5.10. Using the developed model, values of CGR at different crack length in the transient region is obtained for the overload ratio of 2.25 and is plotted against the actual crack length as shown in Figure 5.11. As shown in the plots of Figure 5.9 – Figure 5.11, the CGR trend predicted by the model shows a good correlation with the experimental values.

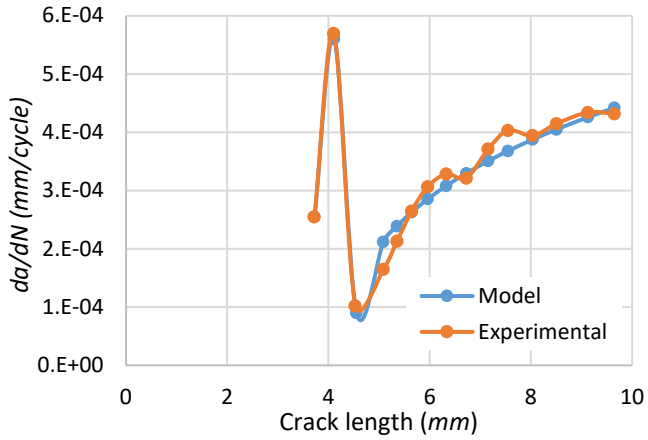

Figure 5.11: Validation plot showing experimental and model predicted CGR against the values of crack length (in the transient region) for the overload ratio of 2.25.

5.5. Conclusion

An empirical model was developed to predict the crack growth rate trend under mode II overloads in an otherwise CA biaxial loading. The proposed model is based on the shape and the size of the plastic zone ahead of the crack tip, and the degree of material hardening within the overload plastic zone. The model parameters were calibrated using the experimental data for the overload ratios of (1.5, -1.5), (1.75, -1.75), (2, -2), and (2.5, -2.5); however, validation of the model was done at the overload ratio of (2.25, -2.25). The data obtained from the model showed a good correlation with the experimental values for CGR in the transient region.

6. SUMMARY AND FUTURE WORK

6.1. Summary

The primary focus of this research is to understand the fatigue damage behavior in AA-7075 under multiaxial loading for which different kinds of loading conditions were considered. These loadings include: i) in-phase bending-torsional fatigue loading; ii) non-proportional bending-torsional fatigue loading; iii) biaxial fatigue with shear overloads; iv) biaxial fatigue with mix-mode overloads. For all these load conditions, investigations were also conducted to understand the morphology of the fracture surfaces as it was crucial in identifying the governing micromechanisms and correlating the macroscale fatigue damage behavior with microscale features.

Under constant amplitude bending-torsion coupled loading, a detailed investigation was conducted on fatigue crack initiation and propagation behavior in AA 7075 for proportional as well as non-proportional loading conditions. A thin-walled tubular specimen was designed to achieve a combination of mode I and II loadings to study mix-mode bending-torsion fatigue behavior. Analyses of crack trajectory and crack growth modes were conducted for various amplitudes of bending and shear stresses at a constant stress amplitude ratio (λ). Tests were conducted under pure bending and pure torsional loading to gain better insight into the mechanisms governing fatigue-fracture behavior under combined bending-torsion loading and segregate the effect of multiaxiality from uniaxial bending or torsional loading. Additional investigations were conducted to understand microscale fracture features that helped in identifying the micromechanisms governing

crack initiation and propagation behavior at different stress levels and at various crack propagation stages.

The complex behavior of variable amplitude multiaxial fatigue loading was studied by capturing the effects of overloads of different magnitudes and mode-mixities on micro- and macroscale crack growth behavior. Some of the key findings from the biaxial fatigue tests with pure shear (mode II) overloads include: (i) the trends for initial acceleration in crack growth rate, crack growth retardation and recovery; (ii) dependence of crack growth rate trends on overload magnitude and instantaneous fatigue crack length at the time of overload; (iii) the role of governing fatigue-fracture micromechanisms, such as, duplex slip, residual compressive stress, plasticity induced crack closure and strain hardening; and (iv) an empirical model to predict crack growth rate trends in the transient region under the influence of overloads of different magnitudes. In addition to mode II overloads, tests were conducted for mix-mode overloads under biaxial fatigue loading and key fatigue damage behavior, including fatigue life, crack growth rate, and recovery distance, were investigated and correlated with the overload parameters. The obtained result showed some interesting crack growth phenomenon in the transient region, where initial acceleration in crack growth rate was observed only for the shear-dominant overloads. The microscale analyses of the fracture surfaces showed distinct fracture features in the pre-overload, transient, and post-overload regions for both tensile and shear dominant overloads.

6.2. Future Work

While the research presented in this dissertation significantly improves the understanding of multiaxial fatigue damage behavior in aerospace-grade AA 7075 under

constant amplitude mix-mode bending-torsion loadings and under load excursions in biaxial loading, further developments and advancements are necessary to maximize its applicability and effectiveness. Future work topics are essential to understand, predict and delay fatigue damage progression in aerospace materials:

- The multi-axial bending-torsion research conducted in Chapter 2 to understand the micro- and macro-scale fatigue damage behavior of AA 7075 at different loading magnitudes can be extended to: understand the effects of changing stress amplitude ratio (λ) on crack trajectory and crack growth modes for various amplitudes of bending and shear stresses. It will also be interesting to investigate the underlying micromechanisms and identify the dominating mechanisms that govern the crack initiation and propagation behavior under various loading conditions and at various crack propagation stages.

- The investigations in Chapter 3 were conducted to gain a comprehensive insight into the nature of crack propagation under the influence of pure mode II (shear) overloads in an otherwise constant amplitude biaxial fatigue loading. The primary goal was to characterize the in-plane biaxial fatigue crack propagation behavior of AA-7075 in the transient region and to investigate the underlying microscale mechanisms at different magnitudes of shear overload ratio and at different fatigue crack lengths. However, this study can be extended to understand the effects of pure shear (mode II) overload on micro- and macroscale fatigue damage behavior when the baseline fatigue load is applied in the form of spectrum loading, such as the Transport Wing Standard (TWIST) and Fighter Aircraft Loading Standard for Fatigue Evaluation (FALSTAFF).

- In chapter 4, research was conducted to understand biaxial fatigue damage behavior of AA 7075 under the influence of mix-mode overloads at the reference overload ratio of 2. This research work can be extended by investigating the effects of mode-mixity at different values of reference overload ratio in order to understand the key fatigue damage behavior, including fatigue life, crack growth rate, and recovery distance and establishing a correlation between macroscopic fatigue damage behavior with underlying micro-mechanisms.

- An empirical model is presented in Chapter 5 that takes into account the shape and the size of the plastic zone ahead of the crack tip, and the degree of material hardening within the overload plastic zone in order to determine the model parameters for predicting crack growth rate in the transient region. The developed model is limited to the use of shear overload at macroscopically smaller crack lengths. However, this model can be extended to incorporate the effects of overload mode-mixity and overload crack length. This will increase the scope and useability of the presented model for a wider range of application.

REFERENCES

[1] Suresh S. Fatigue of materials. Cambridge University Press; 1998. doi:10.1017/CBO9780511806575.

[2] Wöhler A. Experiments to determine the forces acting on the railway carriage axles and the resistance of the carriage axles. J Constr 1860;10:583–614.

[3] Bauschinger J. On the change of the position of the elastic limit of iron and steel under cyclic variations of stress. Mech-Tech Lab 1886;13.

[4] Coffin Jr LF. A study of the effects of cyclic thermal stresses on a ductile metal. Trans Am Soc Mech Eng 1954;76:931–50.

[5] Manson SS. Behavior of materials under conditions of thermal stress. Natl Advis Comm Aeronaut 1953;2933.

[6] Inglis CE. Stresses in a plate due to the presence of cracks and sharp corners. Trans Inst Nav Arch 1913;55:219–41.

[7] Griffits AA. VI. The phenomena of rupture and flow in solids. Philos Trans R Soc London Ser A, Contain Pap a Math or Phys Character 1921;221:163–98. doi:10.1098/rsta.1921.0006.

[8] Irwin GR. Analysis of stresses and strains near the end of a crack transversing a plate. Trans ASME, Ser E, J Appl Mech 1957;24:361–4.

[9] Paris PC, Gomez MP, Anderson WE. A rational analytic theory of fatigue. Trend Eng 1961;13.

[10] Elber W. The significance of fatigue crack closure 1971. doi:10.1520/stp26680s.

[11] Thompson N, Wadsworth N, Louat N. XI. The origin of fatigue fracture in copper. Philos Mag 1956;1:113–26. doi:10.1080/14786435608238086.

[12] Zapffe CA, Worden CO. Fractographic study of deformation and cleavage in ingot iron. Preprint 1950;31:577–602.

[13] Forsyth PJE, Ryder DA. Fatigue fracture: some results derived from the microscopic examination of crack surfaces. Aircr Eng Aerosp Technol 1960;32:96–9. doi:10.1108/eb033233.

[14] Palmgren A. The life of bullet barrels. Zeitshrift Des Verein Duetsher Ingenieure 1924;68:339.

[15] Miner MA. Cumulative fatigue damage. J Appl Mech 1945;12:A159–64.

[16] Tanaka K. Fatigue crack propagation from a crack inclined to the cyclic tensile axis.

Eng Fract Mech 1974;6:493. doi:10.1016/0013-7944(74)90007-1.

[17] Irwin GR. Fracture mode transition for a crack traversing a plate. J Fluids Eng Trans ASME 1960;82:417–23. doi:10.1115/1.3662608.

[18] Dugdale DS. Yielding of steel sheets containing slits. J Mech Phys Solids 1960;8:100–4. doi:10.1016/0022-5096(60)90013-2.

[19] Qian J, Fatemi A. Mixed mode fatigue crack growth: A literature survey. Eng Fract Mech 1996;55:969–90. doi:10.1016/S0013-7944(96)00071-9.

[20] Datta S, Chattopadhyay A, Iyyer N, Phan N. Fatigue crack propagation under biaxial fatigue loading with single overloads. Int J Fatigue 2018;109:103–13. doi:10.1016/j.ijfatigue.2017.12.018.

[21] Fatemi A, Gates N, Socie DF, Phan N. Fatigue crack growth behaviour of tubular aluminium specimens with a circular hole under axial and torsion loadings. Eng Fract Mech 2014;123:137–47. doi:10.1016/j.engfracmech.2014.04.010.

[22] Tanaka K. Crack initiation and propagation in torsional fatigue of circumferentially notched steel bars. Int J Fatigue 2014;58:114–25. doi:10.1016/j.ijfatigue.2013.01.002.

[23] Singh AK, Datta S, Chattopadhyay A, Phan N. Characterization of crack propagation behavior in Al-7075 under in-plane biaxial fatigue loading with shear overloads. Int J Fatigue 2020;134:105529. doi:10.1016/J.IJFATIGUE.2020.105529.

[24] Singh AK, Datta S, Chattopadhyay A, Phan N. Effect of shear overloads on crack propagation in Al-7075 under in-plane biaxial fatigue loading. ASME 2019 Int. Mech. Eng. Congr. Expo. Am. Soc. Mech. Eng. Digit. Collect., 2019.

[25] Neerukatti RK, Datta S, Chattopadhyay A, Iyyer N, Phan N. Characterization of fatigue crack propagation under complex biaxial loading. Vol. 9 Mech. Solids, Struct. Fluids; NDE, Diagnosis, Progn., ASME; 2016, p. V009T12A041. doi:10.1115/IMECE2016-66337.

[26] Neerukatti RK, Datta S, Chattopadhyay A, Iyyer N, Phan N. Fatigue crack propagation under in-phase and out-of-phase biaxial loading. Fatigue Fract Eng Mater Struct 2018;41:387–99. doi:10.1111/ffe.12690.

[27] Wolf CH, Henkel S, Burgold A, Qiu Y, Kuna M, Biermann H. Investigation of fatigue crack growth under in-phase loading as well as phase-shifted loading using cruciform specimens. Int J Fatigue 2019;124:595–617. doi:10.1016/J.IJFATIGUE.2019.03.011.

[28] Duan M, Li Y, Liu H, Shu Y. Fatigue crack behaviors under asynchronous biaxial loading. Int J Fatigue 2019;126:248–57. doi:10.1016/J.IJFATIGUE.2019.05.006.

[29] Fleck NA. Fatigue crack growth due to periodic underloads and overloads. Acta Metall 1985;33:1339–54.

[30] Li Y, Retraint D, Xue H, Gao T, Sun Z. Fatigue properties and cracking mechanisms of a 7075 aluminum alloy under axial and torsional loadings. Procedia Struct Integr 2019;19:637–44. doi:10.1016/J.PROSTR.2019.12.069.

[31] Otsuka A, Tohgo K. Fatigue crack initiation and growth under mixed mode loading in aluminum alloys 2017-T3 and 7075-T6. Eng Fract Mech 1987;28:721–32. doi:10.1016/0013-7944(87)90065-8.

[32] Otsuka A, Mori K, Ohshima T. Mode II fatigue crack growth in aluminum alloys and mild steel. Adv Fract Res 1982:1851–8.

[33] Borrego LP, Antunes FV, Costa JM, Ferreira JM. Mixed-mode fatigue crack growth behaviour in aluminium alloy. Int J Fatigue 2006;28:618–26. doi:10.1016/J.IJFATIGUE.2005.07.047.

[34] Liu HWW. Shear fatigue crack growth: a literature survey. vol. 8. 1985. doi:10.1111/j.1460-2695.1985.tb00429.x.

[35] Vormwald M, Zerres P, Group MM, Vormwald M, Zerres P, Group MM, et al. Review of fatigue crack growth under non-proportional loading. Int J Fatigue 2014;58:1–14. doi:http://dx.doi.org/10.1016/j.ijfatigue.2013.04.001.

[36] Qian J, Fatemi A. Fatigue crack growth under mixed-mode I and II loading. Fatigue Fract Eng Mater Struct 1996;19:1277–84. doi:10.1111/j.1460-2695.1996.tb00950.x.

[37] Paul SK, Tarafder S. Cyclic plastic deformation response at fatigue crack tips. Int J Press Vessel Pip 2013;101:81–90. doi:10.1016/J.IJPVP.2012.10.007.

[38] Hua CT, Socie DF. Fatigue damage in 1045 steel under constant amplitude biaxial loading. Fatigue Fract Eng Mater Struct 1984;7:165–79. doi:10.1111/j.1460-2695.1984.tb00187.x.

[39] Socie DF. Fatigue damage maps. Proc. 3rd Int. Conf. Fatigue Fatigue Threshold., Engineering Materials Advisory Services; 1987, p. 599–616.

[40] Brown MW, Miller KJ. Initiation and growth of cracks in biaxial fatigue. Fatigue Fract Eng Mater Struct 1979;1:231–46. doi:10.1111/j.1460-2695.1979.tb00380.x.

[41] Plank R, Kuhn G. Fatigue crack propagation under non-proportional mixed mode loading. Eng Fract Mech 1999;62:203–29. doi:10.1016/S0013-7944(98)00097-6.

[42] Zhang J, Shi X, Bao R, Fei B. Tension–torsion high-cycle fatigue failure analysis of 2A12-T4 aluminum alloy with different stress ratios. Int J Fatigue 2011;33:1066–74. doi:10.1016/j.ijfatigue.2010.12.007.

[43] Tanaka K, Matsuoka S, Kimura M. Fatigue strength of 7075-T6 aluminium alloy under combined axial loading and torsion. Fatigue Fract Eng Mater Struct 1984;7:195–211. doi:10.1111/j.1460-2695.1984.tb00189.x.

[44] Gough HJ, Pollard H V. The strength of metals under combined alternating stresses. Proc Inst Mech Eng 1935;131:3–103. doi:10.1243/PIME_PROC_1935_131_008_02.

[45] Susmel L, Petrone N. Multiaxial fatigue life estimations for 6082-T6 cylindrical specimens under in-phase and out-of-phase biaxial loadings. Eur. Struct. Integr. Soc., vol. 31, Elsevier; 2003, p. 83–104. doi:10.1016/S1566-1369(03)80006-7.

[46] Park J, Nelson D, Rostami A. Small crack growth in combined bending-torsion fatigue of A533B steel. Fatigue Fract Eng Mater Struct 2001;24:179–91. doi:10.1046/j.1460-2695.2001.00386.x.

[47] Park J, Nelson D V. In-phase and out-of-phase combined bending-torsion fatigue of a notched specimen. Multiaxial Fatigue Deform Test Predict ASTM Int 2000;1946:246–65.

[48] Branco R, Costa JD, Antunes F V. Fatigue behaviour and life prediction of lateral notched round bars under bending-torsion loading. Eng Fract Mech 2014;119:66–84. doi:10.1016/j.engfracmech.2014.02.009.

[49] Nishihara T, Kawamoto M. The strength of metals under combined alternating bending and torsion with phase difference. Mem Coll Eng Kyoto Imp Univ 1945;11:85–112.

[50] Findley WN. Combined-stress fatigue strength of 76S-T61 aluminum alloy with superimposed mean stresses and corrections for yielding. 1953.

[51] Marciniak Z, Rozumek D, Macha E. Fatigue lives of 18G2A and 10HNAP steels under variable amplitude and random non-proportional bending with torsion loading. Int J Fatigue 2008;30:800–13. doi:10.1016/j.ijfatigue.2007.07.001.

[52] Niesłony A, Łagoda T, Walat K, Kurek M. Multiaxial fatigue behaviour of AA6068 and AA2017A aluminium alloys under in-phase bending with torsion loading condition. Materwiss Werksttech 2014;45:947–52. doi:10.1002/mawe.201400214.

[53] Davis JR. Aluminum and aluminum alloys. Light Met Alloy 2001:66. doi:10.1361/autb2001p351.

[54] Richard HA. Specimens for investigating biaxial fracture and fatigue processes. Mechcanical Eng. Publ., 1989, p. 217–29.

[55] Zhizhong H, Lihua M, Shuzhen C. A study of shear fatigue crack mechanisms. Fatigue Fract Eng Mater Struct 1992;15:563–72. doi:10.1111/j.1460-2695.1992.tb01295.x.

[56] Yokoborij T, Kamei A, Yokobori AT. Fatigue crack propagation under mode II loading. Int J Fatigue 1976;12:2–4.

[57] Pook LE. Comments on fatigue crack growth under mixed modes I and III and pure mode III loading. Multiaxial Fatigue, ASTM STP 853 1985:249–63.

[58] Shamsaei N, Fatemi A. Small fatigue crack growth under multiaxial stresses. Int J Fatigue 2014;58:126–35. doi:10.1016/J.IJFATIGUE.2013.02.002.

[59] Gates N, Fatemi A. Friction and roughness induced closure effects on shear-mode crack growth and branching mechanisms. Int J Fatigue 2016;92:442–58. doi:10.1016/j.ijfatigue.2016.01.023.

[60] Yang Y, Vormwald M. Fatigue crack growth simulation under cyclic non-proportional mixed mode loading. Int J Fatigue 2017;102:37–47. doi:10.1016/j.ijfatigue.2017.04.014.

[61] Handbook ASM. Fractography, Vol.12. ASM international Materials; 1987.

[62] Kim WH, Laird C. Crack nucleation and stage I propagation in high strain fatigue—II. mechanism. Acta Metall 1978;26:789–99. doi:10.1016/0001-6160(78)90029-9.

[63] Cina B, Kaatz T. A systematic study of the fractography of fatigue in high strength aluminium alloys. Fatigue Eng Mater Struct 1979;2:85–95.

[64] Meyers MA, Chawla KK. Mechanical behavior of materials. 1999.

[65] Schijve J. Fatigue of structures and materials. Springer Science & Business Media; 2009. doi:10.1007/978-1-4020-6808-9.

[66] Wang Y-YY, Yao W-XX. A multiaxial fatigue criterion for various metallic materials under proportional and nonproportional loading. Int J Fatigue 2006;28:401–8. doi:10.1016/j.ijfatigue.2005.07.007.

[67] Sonsino CM. Influence of material's ductility and local deformation mode on multiaxial fatigue response. Int J Fatigue 2011;33:930–47. doi:10.1016/j.ijfatigue.2011.01.010.

[68] Sonsino CM. Influence of load and deformation-controlled multiaxial tests on fatigue life to crack initiation. Int J Fatigue 2001;23:159–67. doi:10.1016/S0142-1123(00)00079-7.

[69] Li J, Li CW, Qiao YJ, Zhang ZP. Fatigue life prediction for some metallic materials under constant amplitude multiaxial loading. Int J Fatigue 2014;68:10–23. doi:10.1016/j.ijfatigue.2014.06.009.

[70] Itoh T, Nakata T, Sakane M, Ohnami M. Nonproportional low cycle fatigue of 6061aluminum alloy under 14 strain paths. vol. 25. Elsevier Masson SAS; 1999.

doi:10.1016/S1566-1369(99)80006-5.

[71] Skibicki D, Sempruch J. Use of a load non-proportionality measure in fatigue under out-of-phase combined bending and torsion. Fatigue Fract Eng Mater Struct 2004;27:369–77. doi:10.1111/j.1460-2695.2004.00757.x.

[72] Shamsaei N, Fatemi A, Socie DF. Multiaxial cyclic deformation and non-proportional hardening employing discriminating load paths. Int J Plast 2010;26:1680–701. doi:10.1016/j.ijplas.2010.02.006.

[73] Socie D. Multiaxial fatigue damage models. J Eng Mater Technol Trans ASME 1987;109:293–8. doi:10.1115/1.3225980.

[74] Fatemi A, Socie DF. A critical plane approach to multiaxial fatigue damage including out-of-phase loading. Fatigue Fract Eng Mater Struct 1988;11:149–65. doi:10.1111/j.1460-2695.1988.tb01169.x.

[75] McDiarmid DL. Fatigue under out-of-phase bending and torsion. Fatigue Fract Eng Mater Struct 1987;9:457–75.

[76] Singh AK, Datta S, Chattopadhyay A, Riddick JC, Hall AJ. Fatigue crack initiation and propagation behavior in Al – 7075 alloy under in-phase bending-torsion loading. Int J Fatigue 2019;126:346–56. doi:10.1016/j.ijfatigue.2019.05.024.

[77] Barter S, Molent L, Goldsmith N, Jones R. An experimental evaluation of fatigue crack growth. Eng Fail Anal 2005;12:99–128. doi:10.1016/j.engfailanal.2004.04.002.

[78] Fathi Sola J, Kelton R, Meletis EI, Huang H. A surface roughness based damage index for predicting future propagation path of microstructure-sensitive crack in pure nickel. Int J Fatigue 2019;122:164–72. doi:10.1016/J.IJFATIGUE.2019.01.012.

[79] Balusu K, Kelton R, Meletis EI, Huang H. Investigating the relationship between grain orientation and surface height changes in nickel polycrystals under tensile plastic deformation. Mech Mater 2019. doi:10.1016/J.MECHMAT.2019.04.011.

[80] Singh AK, Datta S, Chattopadhyay A, Hall A, Riddick JC. Fatigue damage initiation and propagation in Al – 7075 under combined bending and torsion loading. AIAA Scitech 2019 Forum, San Diego: American Institute of Aeronautics and Astronautics; 2019. doi:10.2514/6.2019-0412.

[81] Zhao T, Zhang J, Jiang Y. A study of fatigue crack growth of 7075-T651 aluminum alloy. Int J Fatigue 2008;30:1169–80. doi:10.1016/j.ijfatigue.2007.09.006.

[82] Dahlin P, Olsson M. Reduction of mode I fatigue crack growth rate due to occasional mode II loading. Int J Fatigue 2004;26:1083–93. doi:10.1016/J.IJFATIGUE.2004.03.003.

[83] Tür YK, Vardar Ö. Periodic tensile overloads in 2024-T3 Al-alloy. Eng Fract Mech 1996;53:69–77. doi:10.1016/0013-7944(95)00116-D.

[84] Borrego LP, Ferreira JM, Pinho da Cruz JM, Costa JM. Evaluation of overload effects on fatigue crack growth and closure. Eng Fract Mech 2003;70:1379–97. doi:10.1016/S0013-7944(02)00119-4.

[85] Sadananda K, Vasudevan A., Holtz R., Lee E. Analysis of overload effects and related phenomena. Int J Fatigue 1999;21:S233–46. doi:10.1016/S0142-1123(99)00094-8.

[86] Chung KH, Yang WH. Mixed mode fatigue crack growth in aluminum plates with composite patches. Int J Fatigue 2003;25:325–33. doi:10.1016/S0142-1123(02)00142-1.

[87] Richard HA, Schramm B, Schirmeisen NH. Cracks on mixed mode loading - theories, experiments, simulations. Int J Fatigue 2014;62:93–103. doi:10.1016/j.ijfatigue.2013.06.019.

[88] Sander M, Richard HA. Experimental and numerical investigations on the influence of the loading direction on the fatigue crack growth. Int J Fatigue 2006;28:583–91. doi:10.1016/j.ijfatigue.2005.05.012.

[89] Lee EU, Taylor RE. Fatigue behavior of aluminum alloys under biaxial loading. Eng Fract Mech 2011;78:1555–64. doi:10.1016/j.engfracmech.2010.11.005.

[90] Mall S, Perel VY. Crack growth behavior under biaxial fatigue with phase difference. Int J Fatigue 2015;74:166–72. doi:10.1016/J.IJFATIGUE.2015.01.005.

[91] Misak HEE, Perel VYY, Sabelkin V, Mall S. Crack growth behavior of 7075-T6 under biaxial tension-tension fatigue. Int J Fatigue 2013;55:158–65. doi:10.1016/J.IJFATIGUE.2013.06.003.

[92] Corbly DM, Packman PF. On the influence of single and multiple peak overloads on fatigue crack propagation in 7075-T6511 aluminum. Eng Fract Mech 1973;5:479–97. doi:10.1016/0013-7944(73)90034-9.

[93] Simpson CA, Kozuki SC, Lopez-Crespo P, Mostafavi M, Connolley T, Withers P. Quantifying fatigue overload retardation mechanisms by energy dispersive X-ray diffraction. J Mech Phys Solids 2019;124:392–410. doi:10.1016/J.JMPS.2018.10.020.

[94] Shlyannikov VN, Tumanov A V. An inclined surface crack subject to biaxial loading. Int J Solids Struct 2011;48:1778–90. doi:10.1016/j.ijsolstr.2011.02.024.

[95] Hua G, Fernando US. Effect of non-proportional overloading on fatigue life. Fatigue Fract Eng Mater Struct 1996;19:1197–206. doi:10.1111/j.1460-2695.1996.tb00943.x.

[96] Fathi Sola J, Kelton R, Meletis EI, Huang H. Predicting crack initiation site in polycrystalline nickel through surface topography changes. Int J Fatigue 2019;124:70–81. doi:10.1016/J.IJFATIGUE.2019.02.027.

[97] İriç S, Ayhan AO. Dependence of fracture toughness on rolling direction in aluminium 7075 alloys 2017;132. doi:10.12693/APhysPolA.132.892.

[98] He W, Wang C, Deng J, Xie D, Zhang Z. Effect of single tensile overload on fatigue crack growth behavior based on plastically dissipated energy and critical distance theory. Eng Fract Mech 2020;223:106744. doi:10.1016/j.engfracmech.2019.106744.

[99] Wang H, Zhang J, Li Y, Wang Z, Wu J. Experimental investigation of overload effects on fatigue crack growth behaviour of 7050-T7451 aluminium alloy. Fatigue Fract Eng Mater Struct 2020;43:2928–42. doi:10.1111/ffe.13329.

[100] Chen C, Ye D, Zhang L, Liu J. DIC-based studies of the overloading effects on the fatigue crack propagation behavior of Ti-6Al-4V ELI alloy. Int J Fatigue 2018;112:153–64. doi:10.1016/j.ijfatigue.2018.03.017.

[101] Thielen M, Schaefer F, Gruenewald P, Laub M, Marx M, Meixner M, et al. In situ synchrotron stress mappings to characterize overload effects in fatigue crack growth. Int J Fatigue 2019;121:155–62. doi:10.1016/j.ijfatigue.2018.12.013.

[102] Pippan R, Hohenwarter A. Fatigue crack closure: a review of the physical phenomena. Fatigue Fract Eng Mater Struct 2017;40:471–95. doi:10.1111/ffe.12578.

[103] Salvati E, Zhang H, Fong KS, Song X, Korsunsky AM. Separating plasticity-induced closure and residual stress contributions to fatigue crack retardation following an overload. J Mech Phys Solids 2017;98:222–35. doi:10.1016/J.JMPS.2016.10.001.

[104] Lopez-Crespo P, Withers PJ, Yusof F, Dai H, Steuwer A, Kelleher J., et al. Overload effects on fatigue crack-tip fields under plane stress conditions: surface and bulk analysis. Fatigue Fract Eng Mater Struct 2013;36:75–84.

[105] Meng Y, Gao H, Yan Y, Gao L. Effects of phase difference and stress ratio on biaxial tension–tension fatigue crack propagation behavior of rolled ZK60 magnesium alloy. Mater Today Commun 2020;24:101159. doi:10.1016/j.mtcomm.2020.101159.

[106] Skinner T, Datta S, Chattopadhyay A, Hall A. Fatigue damage behavior in carbon fiber polymer composites under biaxial loading. Compos Part B Eng 2019;174:106942. doi:10.1016/j.compositesb.2019.106942.

[107] Singh AK, Datta S, Chattopadhyay A, Phan N. Fatigue crack growth behavior in Al-

7075 under in-plane biaxial loading with mixed-mode overloads. TMS 2020 149th Annu. Meet. Exhib. Suppl. Proc., Springer, Cham; 2020, p. 1465–78.

[108] Li G, Datta S, Chattopadhyay A, Iyyer N, Phan N. An online-offline prognosis model for fatigue life prediction under biaxial cyclic loading with overloads. Fatigue Fract Eng Mater Struct 2019;42:1175–90. doi:10.1111/ffe.12983.

[109] Misak HE, Perel VY, Sabelkin V, Mall S. Corrosion fatigue crack growth behavior of 7075-T6 under biaxial tension-tension cyclic loading condition. Eng Fract Mech 2013;106:38–48. doi:10.1016/j.engfracmech.2013.04.004.

[110] Lê Minh B, Maitournam MH, Doquet V. A cyclic steady-state method for fatigue crack propagation: Evaluation of plasticity-induced crack closure in 3D. Int J Solids Struct 2012;49:2301–13. doi:10.1016/J.IJSOLSTR.2012.04.040.

[111] Bhandarkar M, Lisagor W. Metallurgical characterization of the fracture of aluminum alloys. 100 Barr Harbor Drive, PO Box C700, West Conshohocken, PA 19428-2959: ASTM International; 1978. doi:10.1520/STP38092S.

[112] Singh AK, Datta S, Chattopadhyay A, Phan N. Effects of overload mode-mixity on fatigue damage behavior and governing micromechanisms in AA7075 under biaxial fatigue loading. Int J Fatigue 2021;145:106141. doi:10.1016/j.ijfatigue.2021.106141.

[113] Wheeler OE. Spectrum loading and crack growth. J Fluids Eng Trans ASME 1972;94:181–6. doi:10.1115/1.3425362.

[114] Wolf E. Fatigue crack closure under cyclic tension. Eng Fract Mech 1970;2:37–45. doi:10.1016/0013-7944(70)90028-7.

[115] Matsuoka S, Tanaka K, Kawahara M. The retardation phenomenon of fatigue crack growth in HT80 steel. Eng Fract Mech 1976;8:507–23. doi:10.1016/0013-7944(76)90005-9.

[116] Sheu BC, Song PS, Hwang S. Shaping exponent in wheeler model under a single overload. Eng Fract Mech 1995;51:135–43. doi:10.1016/0013-7944(94)00250-L.

[117] Yichi L, Kangxian L. A new model for fatigue crack growth after a single overload. Eng Fract Mech 1993;46:849–56. doi:10.1016/0013-7944(93)90136-G.

[118] Bolotin V V., Lebedev VL. Analytical model of fatigue crack growth retardation due to overloading. Int J Solids Struct 1996;33:1229–42. doi:10.1016/0020-7683(95)00096-8.

[119] Willenborg J, Engle RM, Wood HA. A crack growth retardation model using an effective stress concept. Afb Oh: 1971.

[120] Yuen BKCC, Taheri F. Proposed modifications to the Wheeler retardation model

for multiple overloading fatigue life prediction. Int J Fatigue 2006;28:1803–19. doi:10.1016/j.ijfatigue.2005.12.007.

[121] Mehrzadi M, Taheri F. A material sensitive modified wheeler model for predicting the retardation in fatigue response of AM60B due to an overload 2013. doi:10.1016/j.ijfatigue.2013.06.022.

[122] Huang X, TORGEIR M, Cui W. An engineering model of fatigue crack growth under variable amplitude loading. Int J Fatigue 2008;30:2–10. doi:10.1016/j.ijfatigue.2007.03.004.

[123] Kim JK, Shim DS. A statistical approach for predicting the crack retardation due to a single tensile overload. Int J Fatigue 2003;25:335–42. doi:10.1016/S0142-1123(02)00145-7.

[124] Pavlou DG. Prediction of fatigue crack growth under real stress histories. Eng Struct 2000;22:1707–13. doi:10.1016/S0141-0296(99)00069-3.

[125] Shahani AR, Shakeri I, Rans CD. Two engineering models for predicting the retardation of fatigue crack growth caused by mixed mode overload. Int J Fatigue 2020;132:105378. doi:10.1016/j.ijfatigue.2019.105378.

[126] Sander M, Richard HA. Finite element analysis of fatigue crack growth with interspersed mode I and mixed mode overloads. Int. J. Fatigue, vol. 27, Elsevier; 2005, p. 905–13. doi:10.1016/j.ijfatigue.2004.10.008.